A Thesis for the Degree of Ph.D. in Engineering

Safety Surgery and Quantitative Pathological Evaluation Based on Haptic Technology

February 2018

Graduate School of Science and Technology
Keio University

Kenji OGAWA

Acknowledgements

I have completed this dissertation as a summary of my research from April 2012 through March 2018 as a member of Ohnishi laboratory, Graduate School of Science and Technology, Keio University. I would like to express my acknowledgments to those who have helped me to complete my research.

First, I would like to express my heartfelt gratitude to Professor Dr. Kouhei Ohnishi. His immense support and insightful comments were invaluable for my research. In addition, he provided me opportunities to take part in the state-of-the-art projects and develop various haptic robots. The activities in the Ohnishi laboratory were precious experiences for me.

I greatly appreciate the members of the SUM committee in Keio University, Professor Dr. Toshiyuki Murakami, Professor Dr. Hiroaki Nishi, Associate Professor Dr. Takahiro Yakoh, Associate Professor Dr. Seiichiro Katsura, and Assistant Professor Dr. Takahiro Nozaki for providing me with a number of valuable advices and comments. I also greatly appreciate the member of the Keio Program for Leading Graduate School. This unique program, which is coordinated by Professor Dr. Kouhei Ohnishi and Professor Dr. Fumihiko Kannari, was very interesting and I had many precious experiences. During this program, I received several opportunities to expand my research. Professor Dr. Toru Takebayashi, Keio University School of Medicine, provided me significant support during my sub-major course research. Furthermore, Mr. Jun Fukuyoshi, the CEO of Caner Scan Co. Ltd., co-operated with my research. In addition, this program gave to me a chance to study overseas for half a year and I am grateful to Professor Dr. Yousef Ibrahim, Federation University Australia, for his collaboration in my research, his advices, and several opportunities to improve the research during my study in Australia.

My deepest appreciation is for Professor Dr. Yuko Kitagawa and Assistant Professor Dr. Norihito Wada. They gave me appropriate feedback about medical haptic applications.

Furthermore, I would like to thank the members of the male infertility medical project team, namely Professor Dr. Teruaki Iwamoto, International University of Health and Welfare, Professor Dr. Yasuhide Morikawa, International University of Health and Welfare, Professor Dr. Yoko Sato, University of East Asia, Dr. Miki Yoshiike, St. Marianna University School of Medicine, Dr. Shiari Nozawa, St. Marianna University School of Medicine, and Mr. Daisuke Tomizuka, Mitsubishi Electric Corporation. The collaboration with them has been a very valuable experience.

I would like to offer my special thanks to Dr. Takahiro Mizoguchi, Haptics Research Center, Mr. Kazuki Tanida, Sumitomo Heavy Industries, Ltd., Mr. Yuki Saito, Yokogawa Electric Corporation, Mr. Kasun Prasanga, Dr. Koyo Yu, Keyence Corporation, and Dr. Takuya Matsunaga for their valuable and practical advice as the seniors of the laboratory. Without their guidance and persistent help, my Ph. D dissertation would not have been possible.

Moreover, I am grateful to Mr. Tetsuzou Kishimoto, the CEO of Kishimotokogyo Inc. I am impressed with his passion and humanity. The products of this company contributed to my research. I would also like to take this opportunity to thank Mr. Takemi Iwai, the CEO of Iwai Seisakusyo Inc. The products of this company also helped my research for EHTS-based medical instruments.

Furthermore, I received encouragement from Mr. Seiji Uozumi, Mr. Yoshiki Ohno, Ms. Seinan Kyo, Mr. Ryouhei Kozuki, and Mr. Nobuto Yoshimura, who are my contemporaries in Ohnishi laboratory. Mr. Bechet Francis has made enormous contributions to projects and experiments for EHTS-based medical instruments. I received tremendous support for activities in Ohnishi laboratory from Mr. Toshiaki Okano.

I am deeply grateful to my parents and brother for giving me tremendous support. Without their support, I could not dedicate myself to this research.

There are a number of people who helped me; however, their names cannot be mentioned here. I would like to again express my sincere gratitude to all the people who have supported me.

February, 2018

Kenji Ogawa

Contents

List of Figures

List of Tables

Chapter 1

Introduction

1.1 Background

1.1.1 Historical Transition of Medical Technology

Medical science has fascinated scientists from time immemorial. Medical science has a long history and its roots go back to the four great civilizations of the world. With the development of civilization, medical science improved, and anatomical descriptions were followed by investigation methods to determine the cause of diseases. Artists in the Renaissance created anatomical drawings. For instance, the anatomical studies and drawings of Leonardo da Vinci are well known. The progress of medical technologies over the centuries has made the treatment of several diseases possible, contributing immensely to healthy living of people.

1.1.2 Highly Advanced Medical Treatment with Robotic Technology

In modern society, the demand for advanced medical technology is growing due to the decreasing birthrate and aging population. Especially, people are interested in medical technology that can improve their daily lives. In other words, today's medical technology is required to take account into how to improve the quality of life (QOL) of people. Now, the use of several medical technologies has become common. However, surgical operations have limitations in many cases and there a constant need to improve the medical technologies used. For instance, in invasive surgeries, surgeons open parts of the patients' bodies. In such traditional open surgeries, the human cannot recognize their motion quantitatively. Therefore, even if the doctor demonstrates the same medical operations, the motion would be

different for each operation. Individual differences and the diagnosis results would be different for each medical doctor. To overcome these problems, surgical operations are expected to be performed increasingly using robotic technologies in the future. The two major advantages using robots for performing surgeries are as follows.

First, robots can perform complex tasks compared to human. This advantage is useful in performing minimally invasive/non-invasive surgical operations. These surgical techniques minimize patients' recovery time and pain due to the very small incisions made during the surgical procedures[1]. Currently, the master-slave tele-operation system is becoming a hot research topic world-wide. The system consists of a master robot and a slave robot. When the operator operates the master robot, the slave robot synchronizes to the master robot's motion at the same time. Consequently, the doctor can demonstrate the medical operation as if he/she puts their hands inside the patient's body and operates the bio-tissue directly. ZEUS, developed by Computer Motion, Inc.[2], and da Vinci developed by Intuitive Surgical, Inc., are famous tele-operational systems used for medical applications. These robots were exclusively developed for performing laparoscopic surgeries. In the case of these tele-operational systems, the doctor only makes a small hole in the patient's body to facilitate the insertion of medical instruments used in the laparoscopic surgical procedure. Hence, these systems perform better in terms of non-invasiveness compared with laparotomy. In addition, tele-operational systems are used for performing natural orifice transluminal endoscopic surgery (NOTES)[3]. The NOTES technique is commonly employed to remove tiny tumors such as cancerous tissues or other malignant tumors. In addition, the technique is applied to surgical suturing. The biggest advantage of NOTES is that the doctor does not make an incision in the abdomen. Generally, three medical tasks are required for both MIS procedure: (i) palpation; a doctor uses a palpation probe under an endoscope to detect a tumor, (ii) tumor removal; the doctor uses long flexible tools such as a forceps with a flexible cable for removing the tumor, (iii) suturing; the doctor uses long flexible tools such as a forceps with a flexible suture for keeping the tissues together.

Second, robots can obtain their motion quantitatively. This advantage is often applied to diagnosis systems such as cancer tissue measurement methodologies. Kawahara *et al.* measured the displacement of abnormal tissues by using air pressure[4]. Cao *et al.* analyzed the liver fibrosis by using an Ultrasound Images[5]. Oshiro *et al.* analyzed the property of the bio-tissue by using an MR Elastography[6]. Likewise, Austere *et al.* measured the live fibrosis by using a "Fibroscan" which is a medical development to evaluate the condition of liver[7]. These researches are helpful to realize a precise diagnosis judgement and operator can measure the physical property more easily.

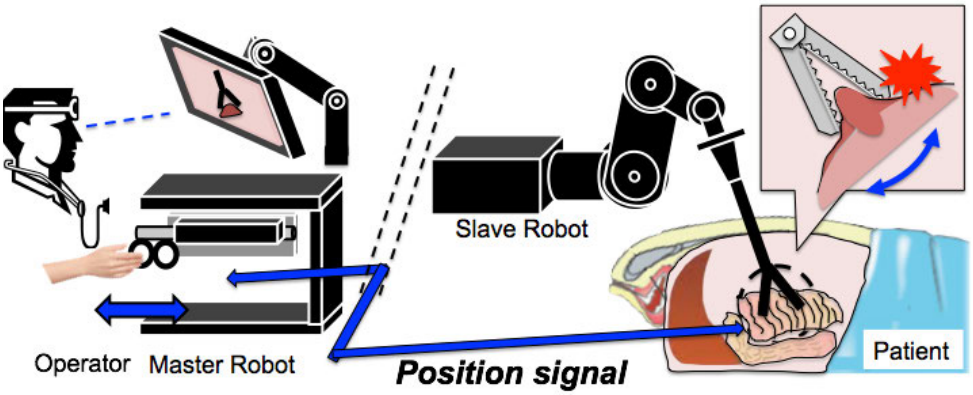

(a) No Force Feedback Surgical System

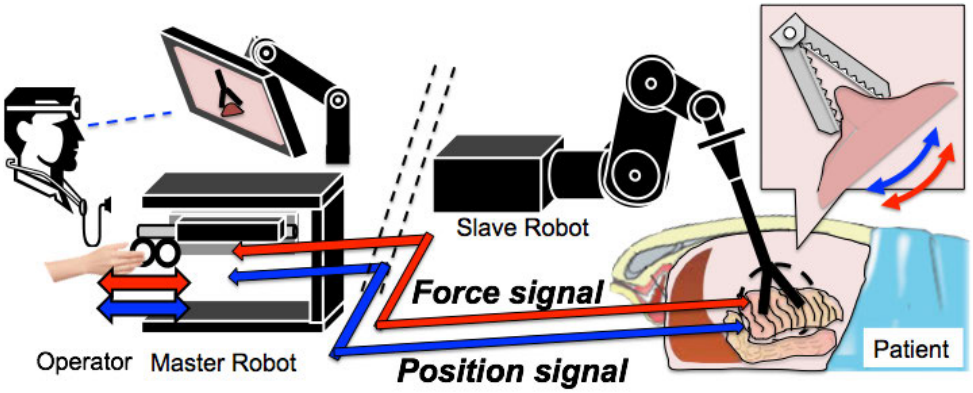

(b) With Force Feedback Surgical System

Fig. 1-1: Remote Surgical Operation System

1.1.3 Importance of Force Information for Medical Science

The studies introduced above only use position information. From the point of view the human's perception, position information is recognized as visual information. Hence, the doctor only knows their motion as a visual information. This constraint would be an obstacle for performing surgical operations. For instance, the surgeon does not understand how much grasping force is added to the bio-tissue like Fig. 1-1(a). Indeed, some medical errors caused by the lack of the haptic information have been reported. Besides, the visual judgement of diseases such as cancer is difficult. In particular, the abnormal tissues hidden inside organs are almost never detected like Fig. 1-2(a). CT or ultrasound scans can detect abnormal tissues even if they are hidden inside the organs but these diagnostic methods are easily influenced by the patient's body conditions such as the amount of water in the tissues.

The application of haptic sensation for laparoscopic surgery and NOTES could be an effective so-

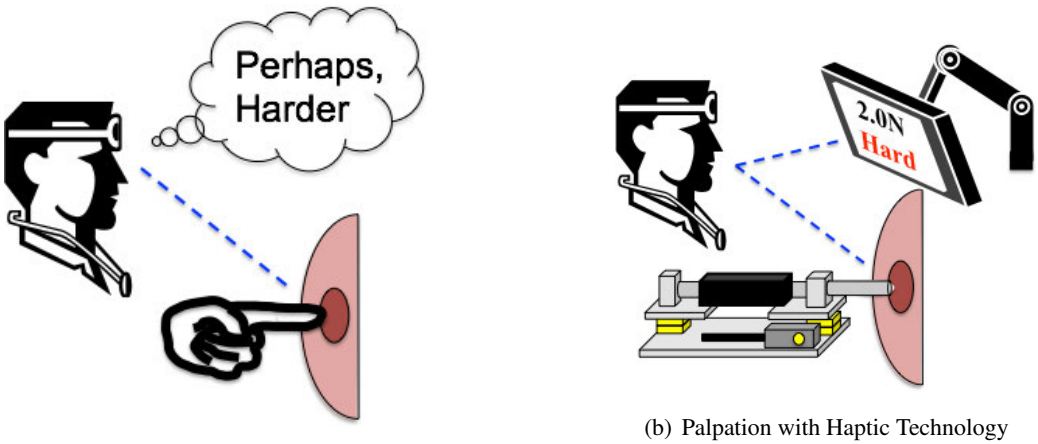

(a) Palpation with Operator's Perception

(b) Palpation with Haptic Technology

Fig. 1-2: Scheme of The Palpation

lution to improve the performance of palpation, grasping, and suturing. Therefore, haptic technology has emerged as a key factor in aiding human - robot interaction. This technology recreates the sense of touch by applying forces, vibrations, or motions to the user. This mechanical stimulation can be used to assist in the creation of virtual objects in a computer simulation, to control such virtual objects, and to enhance the remote control of machines and devices (tele-robotics). Consequently, by using haptics for medical instruments, a doctor can feel the reaction force from the bio-tissue and surgical operations can be performed more safely like Fig. 1-1(b). Bilateral control, which is one of the haptic technologies, can achieve a force and a tactile feedback with very high performance during tele-operations.

Likewise, force information is very important to understand the physical structure of the bio-tissue quantitatively like Fig. 1-2(b). Majira *et al.* measured the stiffness of breast cancer tissue by using an atomic force microscope (AFM)[8]. The AFM is a microscope system that measures the displacement of the sensing probe by using the atomic force generated between the measurement sample and the probe. Thus, the detailed structure of the surface shape can be scanned. In addition, the reaction force of the measurement sample is also available. The measurement results indicated that the structure of breast cancer tissues is different from that of normal tissues in terms of the physical characteristics. In addition, Moreira *et al.* measured the stiffness and the viscosity of a pig's heart[9].

1.2 Orientation of this research

This research discusses the integration of haptic technology into medical applications to improve the QOL of patients.

First, a one-DoF haptic medical instrument is developed based on the electro-hydraulic transmission system (EHTS). This research focuses on applying the haptic tele-operation system for NOTES surgery. The biggest characteristics of developed instruments are the fluid energy is used to transmit the position and force to the end-effector. In addition, the size of the instrument is less than 2.6 mm and hence the instrument can be easily inserted into an endoscope. Haptic sensation with bilateral control under a very narrow area, which a human cannot easily access, can be achieved by the developed instrument. In conventional research on medical applications with force feedback, a flexible actuator, which consists of a metal wire, a metal tube, and a linear actuator, is often used[10, 11]. Position and force information are transmitted to the endpoint of the metal tube. As a conventional method for medical applications, Phee *et al.* proposed master and slave surgical system by using a flexible actuator[12]. However, the transmission performance depends on the wire's shape due to the nonlinear friction. Thus, the precise reaction force from the bio - tissue is difficult to obtain by the flexible actuator. Correspondingly, Do *et al.* proposed a master - slave surgical system by using the flexible actuator with nonlinear compensation[13]. However, the position encoder needed to be mounted on the endpoint. Therefore, the size of the endpoint became large. For these reasons, the release-type medical instruments cannot transmit a clear haptic sensation. In the case of the EHTS-based mechanical applications, the transmission loss does not depend on the wire's shape. Therefore, good transmission performance is guaranteed irrespective of the wire's shape. The validity of the transmission performance was confirmed through the experiment.

Second, the quantitative index with force information for non-obstructive azoospermia (NOA) judgement is proposed[14]. This research focuses on NOA that is a male infertility condition in which the spermatogenic function deteriorates. As a sperm-extraction method for NOA patients, the micro dissection testicular sperm extraction (MD-TESE) is a commonly used method[15, 16]. However, the low sperm-collection rate and the large individual differences are considered as problems associated with MD-TESE. These problems are caused by the visual information which the surgeon is obtained by a microscope camera. To overcome this problem, the stiffness of the testicles is applied as a quantitative index. The testicles of Syrian hamsters are measured and compared with the normal testicles. In addition, the stiffness of the seminiferous tubule is also measured. Further, a morphological analysis was also

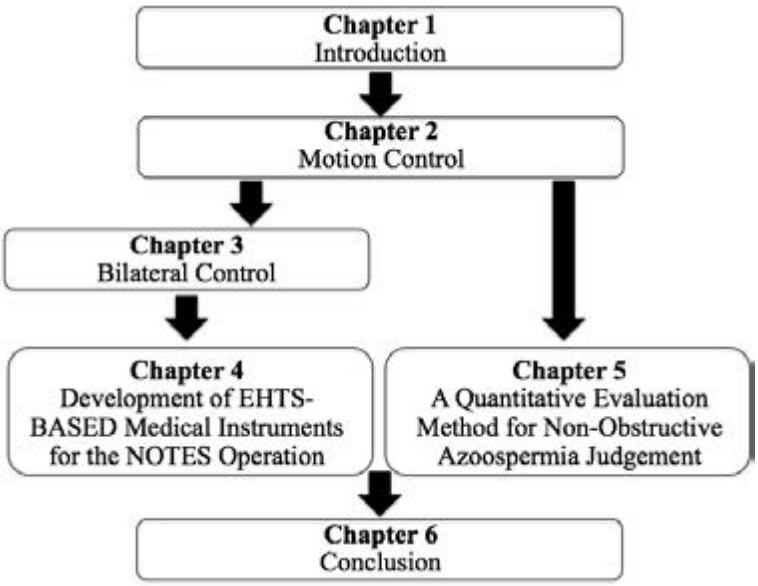

Fig. 1-3: Chapter Organization

performed.

1.3 Chapter organization

The flowchart shown in Fig. 1.3 explains how the content of this thesis is organized.

Chapter 1 provides the introduction of this research. In addition, the problems to be addressed in conventional researches are explained.

Chapter 2 describes motion control based on robust acceleration control[17]. As a method to realize robust acceleration control, a disturbance observer (DOB) is explained[18]. Besides, reaction force observer (RFOB) is described to estimate force information [19]. Then, position control and force control based on acceleration control are described.

Chapter 3 describes bilateral control. Acceleration-based four-channel bilateral control is explained as a method to transmit clear force and position information. First, a basic strategy of the four-channel bilateral control is explained. Next, a modal space bilateral control method to describe the role of the actuator function is explained. In addition, the oblique coordinate bilateral control method, which is proposed by Sakaino *et al.*, is described[20]. This control method is based on modal space bilateral control and eliminates the interference generated by different mass actuators or scaling control. Chapter 4 de-

scribes one-DoF flexible haptic medical instruments based on the EHTS. The chapter presents the details of the two medical instruments developed: (i) a palpation probe and (ii) a pair of forceps. The main characteristic of these instruments is the fluid energy used to transmit the position and force information to the end-effector. The position/force transmission performance is dramatically improved compared with that of release-type medical instruments, without depending on the wire's position. In addition, oblique coordinate bilateral control implemented in both the instruments as well as the experiments performed to confirm the efficacy of the haptic sensation are described.

Chapter 5 describes the quantitative evaluation for NOA judgement. NOA is one of the male infertility diseases in which the spermatogenic function is deteriorated. As a sperm-extraction method for NOA patients, the MD-TESE method is widely used. However, the low sperm-collection rate and the large individual differences are considered as problems of the MD-TESE method. These problems are caused by the visual information that the surgeon obtains by using a microscope camera. To overcome this problem, a quantitative index for spermatogenesis evaluation is constructed. As a quantitative index, the stiffness of the testicle and the seminiferous tubule is measured. This stiffness is compared with that of a normal testicle. The validity of the index is analyzed by a static approach as well as a morphological approach.

Finally, Chapter 6 drawn conclusions.

Chapter 2

Motion Control

Motion control is the fundamental control theory at work behind a mechatronic system [17] that produces desired motions. In this research, an acceleration control method is applied to motion control, and the details of the process are described. First, the actuator's model is described in Section 2.1. Next, the detailed structure of the acceleration control scheme is described in Section 2.2, along with the acceleration-based position and force control techniques. A method to create robust acceleration control through the use of a disturbance observer (DOB) is subsequently explained in Section 2.3. The structures of two types of DOBs and the stability conditions are also described. This section additionally discusses the confirmation of the performance of both DOBs by using Bode plot simulations and explains the robust position control method and the confirmation of its performance through experiments. Furthermore, a reaction force observer (RFOB) used to obtain a reaction force estimation is described, along with the acceleration-based force control technique with the DOB and the RFOB and the confirmation of its performance through experiments.

2.1 Actuator's Modeling

This section describes the actuator's modeling. In this research, two different types of actuators are used. Each actuator's model is described in 2.1.1 and 2.1.2.

2.1.1 Liner Actuator

A linear actuator is a type of actuator that produces a forward and backward motion. The linear actuator's force, f_{a}, can be derived as

$$f_{\mathrm{a}} = K_{\mathrm{t}} I_{\mathrm{a}}. \tag{2.1}$$

where K_{t} is a torque coefficient and I_{a} is the inflow armature current. I_{a} is controlled by a current minor loop to control the actuator's force precisely. Here, the relationship between the inflow armature current (I_{a}) and the current reference ($I_{\mathrm{a}}^{\mathrm{ref}}$) is derived as

$$\frac{I_{\mathrm{a}}^{\mathrm{ref}}}{I_{\mathrm{a}}} = \frac{1}{1 + T_{\mathrm{e}}' s}, \tag{2.2}$$

where T_{e}' is the total time constant expressed as

$$T_{\mathrm{e}}' = \frac{K_{\mathrm{e}} T_{\mathrm{m}} T_{\mathrm{e}}}{K_0}, \tag{2.3}$$

where K_{e} is the coefficient of the back-emf constant, T_{m} is the mechanical time constant, the T_{e} is the electric time constant, and the K_0 is the gain for armature current control. Generally, K_0 can set at a large enough value to ignore the influence of $K_{\mathrm{e}}, T_{\mathrm{m}}$ and T_{e}. Therefore, I_{a} is almost the same as the current reference value, $I_{\mathrm{a}}^{\mathrm{ref}}$. From this reason, Eq. (2.1) can be rewritten as

$$f_{\mathrm{a}} = K_{\mathrm{t}} I_{\mathrm{a}}^{\mathrm{ref}}. \tag{2.4}$$

On the other hand, f_{a} can be derived by using the following mechanical model:

$$f_{\mathrm{a}} = M \ddot{q}^{\mathrm{res}}, \tag{2.5}$$

where q is the actuator's position and the $\bigcirc^{\mathrm{res}}$ is the response value. By using Eq. (2.4) and Eq. (2.5), the electrical and mechanical system integration model is expressed as

$$M \ddot{q}^{\mathrm{res}} = K_{\mathrm{t}} I_{\mathrm{a}}^{\mathrm{ref}}. \tag{2.6}$$

Therefore, the linear actuator is one of the mechatronic systems. In actual situations, a load force, f_{load}, is added to the linear actuator, and Eq. (2.6) is rewritten as

$$M \ddot{q}^{\mathrm{res}} = K_{\mathrm{t}} I_{\mathrm{a}}^{\mathrm{ref}} - f_{\mathrm{load}}. \tag{2.7}$$

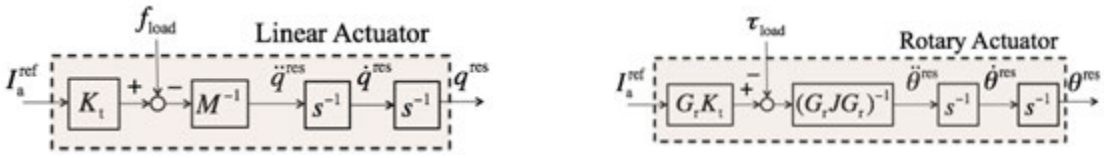

(a) A Linear Actuator Model

(b) A Geared Rotary Actuator Model

Fig. 2-1: Block Diagram of the Actuator's Model

Eq. (2.7) is the motion equation of the linear actuator, wherein f_{load} is the load force. In the case of the 1-DoF linear actuator, f_{load} is defined as

$$f_{\mathrm{load}} = f_{\mathrm{ext}} + f_{\mathrm{g}} + (f_{\mathrm{c}}\mathrm{sgn}(\dot{q}) + D\dot{q}), \tag{2.8}$$

wehre $\mathrm{sgn}(\cdot)$ is a signum function. In Eq. (2.8), each parameter is described as follows:

- f_{ext} : External force from the environment,
- f_{g} : Gravity force, and
- $(f_{\mathrm{c}}\mathrm{sgn}(\dot{q}) + D\dot{q})$: Coulomb friction and viscous friction including the actuator.

Here, block diagram of Eq. (2.7) is shown in Fig. 2-1(a).

2.1.2 Rotary Actuator

A rotary actuator is used to produce a rotary motion. The motion equation of a rotary actuator is expressed, similarly to that of a linear actuator, as

$$J\ddot{\theta}^{\mathrm{res}} = K_{\mathrm{t}} I_{\mathrm{a}}^{\mathrm{ref}} - \tau_{\mathrm{load}}, \tag{2.9}$$

where J is a moment of inertia, θ is the angle, and τ is the torque. In the case of a geared rotary actuator, the motion equation is

$$G_{\mathrm{r}} J G_{\mathrm{r}} \ddot{\theta}^{\mathrm{res}} = G_{\mathrm{r}} K_{\mathrm{t}} I_{\mathrm{a}}^{\mathrm{ref}} - \tau_{\mathrm{load}}, \tag{2.10}$$

where G_{r} is the gear ratio and τ_{load} is the load torque expressed as

- τ_{int} : Internal torque such as Coriolis force and centrifugal force,

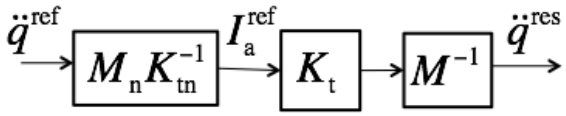

Fig. 2-2: Block Diagram of An Acceleration Control ($f_{\mathrm{dis}} = 0$)

- τ_{ext} : External torque from environment,
- τ_{g} : Torque from gravity force, and
- $(\tau_{\mathrm{c}}\mathrm{sgn}(\dot{\theta}) + D\dot{\theta})$: Coulomb friction and viscous friction including actuator.

2.2 Acceleration Control

This section describes an acceleration control method. In acceleration control, a reference signal inputted to the actuator is produced by the acceleration information. In the case of a linear actuator, the acceleration control of which is shown in the block diagram in Fig. 2-2, the transfer function from the acceleration reference to the acceleration response is expressed as

$$\frac{\ddot{q}^{\mathrm{res}}}{\ddot{q}^{\mathrm{ref}}} = \frac{M_{\mathrm{n}}K_{\mathrm{t}}}{MK_{\mathrm{tn}}}, \tag{2.11}$$

where $\bigcirc_{\mathrm{n}}$ is the nominal value. If M_{n} and K_{tn} equal M and K_{t}, the ideal transfer function between $\ddot{q}^{\mathrm{ref}}$ and $\ddot{q}^{\mathrm{res}}$ is

$$\frac{\ddot{q}^{\mathrm{res}}}{\ddot{q}^{\mathrm{ref}}} = 1. \tag{2.12}$$

Therefore, precise control is achieved by the acceleration control method.

2.2.1 Position Control

Position control is the most fundamental control method for matching the position command and the position response. The transfer function from a acceleration command, $\ddot{q}^{\mathrm{cmd}}$, and an acceleration response, $\ddot{q}^{\mathrm{res}}$, is

$$\frac{\ddot{q}^{\mathrm{ref}}}{\ddot{q}^{\mathrm{cmd}}}\frac{\ddot{q}^{\mathrm{res}}}{\ddot{q}^{\mathrm{ref}}} = 1. \tag{2.13}$$

Here, an acceleration reference $\ddot{q}^{\mathrm{ref}}$ is expressed as

$$\ddot{q}^{\mathrm{ref}} = \ddot{q}^{\mathrm{cmd}} + q^{\mathrm{e}} C_{\mathrm{p}}(s), \tag{2.14}$$

where $C_{\mathrm{p}}(s)$ is the position controller and q^{e} is the position error. If PD control is applied to position control, both parameters are expressed as

$$C_{\mathrm{p}}(s) = K_{\mathrm{p}} + K_{\mathrm{v}} s, \tag{2-14a}$$

$$q^{\mathrm{e}} = q^{\mathrm{cmd}} - q^{\mathrm{res}}, \tag{2-14b}$$

where K_{p} is the proportional controller and K_{v} is the differentiation controller. Eq. (2.14) describes the position error convergence performance depends on two controllers. Here, when the position error convergence performance depends on two controllers. Here, when K_{p} and K_{v} satisfy the relation shown in Eq. (2.15), the attenuation becomes 1. Thus, the response value becomes the critical damping value and converges with the command value without vibration.

$$K_{\mathrm{v}} = 2\sqrt{K_{\mathrm{p}}}. \tag{2.15}$$

2.2.2 Force Control

Force control is a control method for controlling the force and reaction force generated between a robot and its environments. The transfer function of force control is expressed as

$$\frac{f^{\mathrm{ref}}}{f^{\mathrm{cmd}}} \frac{f^{\mathrm{res}}}{f^{\mathrm{ref}}} = 1. \tag{2.16}$$

The force reference is

$$f^{\mathrm{ref}} = f^{\mathrm{cmd}} + f^{\mathrm{e}} C_{\mathrm{f}}(s), \tag{2.17}$$

where $C_{\mathrm{f}}(s)$ is the force controller and f^{e} is the force error described as

$$C_{\mathrm{f}}(s) = K_{\mathrm{f}}, \tag{2-17a}$$

$$f^{\mathrm{e}} = f^{\mathrm{cmd}} - f^{\mathrm{res}}, \tag{2-17b}$$

where K_{f} is the proportional controller. Unlike in the case of position control, the force controller does not apply a damping gain due to the avoidance of a noise effect from the differential value of f^{res}.

2.3 Robustness Improvement Techniques Using the Disturbance Observer

In actual situations, the disturbance force, such as an uncertain force or variation in the parameters, would occur during the actuator's movement. These factors contribute to the deterioration of the position and force tracking performance. A Disturbance Observer (DOB) is an observer that suppresses the influence of the disturbance force through feedback compensation [18, 21]. This section describes the basic ideas behind the DOB and the parameters tuning method and presents an analysis of the stability and robustness of the DOB. In 2.3.1, the disturbance force is defined. In 2.3.2, the basic idea behind the disturbance force estimation is explained. Further, two types of DOBs are described and the stability and robustness are analyzed in 2.3.3. Finally, the performances of both DOBs are compared by using Bode plot simulations in 2.3.4

2.3.1 Definition of Disturbance Force

Before describing the structure of the DOB, this section provides a definition for disturbance force. When an actuator is actuated, mass M and torque coefficient K_{t} can be altered by changing the robot posture. The variation of each parameter can be expressed as

$$M = M_{\mathrm{n}} + \Delta M, \tag{2.18}$$

$$K_{\mathrm{t}} = K_{\mathrm{tn}} + \Delta K_{\mathrm{t}}. \tag{2.19}$$

In Eq. (2.18) and Eq. (2.19), the $\Delta\bigcirc$ is a parameter's variation. If the influence of the parameter variation is included in the motion equation expressed as Eq. (2.7), the motion equation can be rewritten as

$$M_{\mathrm{n}}\ddot{q}^{\mathrm{res}} = K_{\mathrm{tn}} I_{\mathrm{a}}^{\mathrm{ref}} - f_{\mathrm{f}} - f_{\mathrm{load}}, \tag{2.20}$$

where f_{f} is a fluctuating force described as

$$f_{\mathrm{f}} = \Delta M_{\mathrm{n}}\ddot{q}^{\mathrm{res}} - \Delta K_{\mathrm{tn}} I_{\mathrm{a}}^{\mathrm{ref}}. \tag{2.21}$$

In Eq. (2.21), $\Delta M_{\mathrm{n}}\ddot{q}^{\mathrm{res}}$ indicates the inertial force by the variation of inertia, while the $\Delta K_{\mathrm{tn}} I_{\mathrm{a}}^{\mathrm{ref}}$ indicates a torque ripple. The summation of the load force, f_{load}, expressed as Eq. (2.8), and the fluctuating

force, f_{f}, is defined as a disturbance force and expressed as

$$\begin{aligned} f_{\mathrm{dis}} &= f_{\mathrm{load}} + f_{\mathrm{f}} \\ &= f_{\mathrm{ext}} + f_{\mathrm{g}} + (f_{\mathrm{c}} + D\dot{q}) + \Delta M\ddot{q}^{\mathrm{res}} - \Delta K_{\mathrm{t}} I_{\mathrm{a}}^{\mathrm{ref}}. \end{aligned} \tag{2.22}$$

2.3.2 Basic Idea of the Disturbance Force Calculation

From the motion equation described as Eq. (2.22), f_{dis} is derived by using $K_{\mathrm{tn}} I_{\mathrm{a}}^{\mathrm{ref}}$ and $M_{\mathrm{n}}\ddot{q}^{\mathrm{res}}$ as follows:

$$f_{\mathrm{dis}} = K_{\mathrm{tn}} I_{\mathrm{a}}^{\mathrm{ref}} - M\ddot{q}^{\mathrm{res}}. \tag{2.23}$$

Consequently, the disturbance force is calculated from the difference between the actuator's input force and the actuator's output force.

2.3.3 The Full-Order DOB

The Plant Model and the Observer Design

As shown in Eq. (2.23), the acceleration response information is needed to calculate the disturbance force. If the position sensing device such a position encoder has only one system mounted, the acceleration signal needs to be estimated from the position information. A state observer is a system that provides a state estimation; it can estimate the acceleration signal. The state observer is designed from the state equation. A state space equation of a linear actuator's model with a disturbance force is derived as

$$\begin{cases} \frac{d\boldsymbol{x}(t)}{dt} = \boldsymbol{A}_{\mathrm{p}}\boldsymbol{x}(t) + \boldsymbol{B}_{\mathrm{p}}u(t) + \boldsymbol{B}_{\mathrm{p}}d(t) \\ y(t) = \boldsymbol{C}_{\mathrm{p}}\boldsymbol{x}(t) \end{cases}, \tag{2.24}$$

where $\boldsymbol{x}$ is the state vector, $\boldsymbol{A}$ is the square matrix, $\boldsymbol{B}$ is the row vector, $\boldsymbol{C}$ is the column vector, $\bigcirc_{\mathrm{p}}$ is the plant, $d(t)$ is the disturbance force, $u(t)$ is the input signal and $y(t)$ is the output signal. Then, the state observer is constructed as

$$\frac{d\hat{\boldsymbol{x}}(t)}{dt} = \boldsymbol{A}_{\mathrm{ob}}\hat{\boldsymbol{x}}(t) + \boldsymbol{B}_{\mathrm{ob}}u_{\mathrm{a}}(t) + \boldsymbol{L}\boldsymbol{C}_{\mathrm{ob}}(\boldsymbol{x}(t) - \hat{\boldsymbol{x}}(t)), \tag{2.25}$$

where $\bigcirc_{\mathrm{ob}}$ is the observer's variable, $u_{\mathrm{a}}(t)$ is the actuator input, $\boldsymbol{L}$ is the observer gain and $\hat{\bigcirc}$ is the estimated signal. The state vector, $\boldsymbol{x}$, can be expressed as

$$\boldsymbol{x}(t) = \hat{\boldsymbol{x}}(t) - \boldsymbol{x}_{\mathrm{e}}(t), \tag{2.26}$$

where $\boldsymbol{x}_{\mathrm{e}}(t)$ is the error of the state vector. By using Eq. (2.25) and Eq. (2.26), the state observer can be written as

$$\frac{d\hat{\boldsymbol{x}}(t)}{dt} = \boldsymbol{A}_{\mathrm{p}}\hat{\boldsymbol{x}}(t) + \boldsymbol{B}_{\mathrm{p}}u(t) + \boldsymbol{B}_{\mathrm{p}}d(t) + \frac{d\boldsymbol{x}_{\mathrm{e}}(t)}{dt} - \boldsymbol{A}_{\mathrm{p}}\boldsymbol{x}_{\mathrm{e}}(t). \tag{2.27}$$

$\frac{d\boldsymbol{x}_{\mathbf{e}}(t)}{dt}$ can be rewritten, by using the state space equation, as

$$\frac{d\boldsymbol{x}_{\mathrm{e}}(t)}{dt} = \boldsymbol{A}_{\mathrm{p}}x_{\mathrm{e}}(t) + \boldsymbol{B}_{\mathrm{p}}d_{\mathrm{e}}(t), \tag{2.28}$$

where $d_{\mathrm{e}}(t)$ is the error signal of a disturbance force. The relationship of $d(t)$, $d_{\mathrm{e}}(t)$ and $\hat{d}(t)$ is expressed as

$$d(t) = \hat{d}(t) - d_{\mathrm{e}}(t). \tag{2.29}$$

Using Eq. (2.28) and Eq. (2.29), Eq. (2.27) can be rewritten as

$$\frac{d\hat{\boldsymbol{x}}(t)}{dt} = \boldsymbol{A}_{\mathrm{p}}\boldsymbol{x}(t) + \boldsymbol{B}_{\mathrm{p}}u(t) + \boldsymbol{B}_{\mathrm{p}}\hat{d}(t). \tag{2.30}$$

Also, if $\boldsymbol{A_{\mathrm{p}}} = \boldsymbol{A_{\mathrm{ob}}}$, $\boldsymbol{B_{\mathrm{p}}} = \boldsymbol{B_{\mathrm{ob}}}$, and $\boldsymbol{C_{\mathrm{p}}} = \boldsymbol{C}_{\mathrm{ob}}$, the estimated disturbance force can be derived by using Eq. (2.25) and Eq. (2.30) as follows:

$$\hat{d}(t) = u_{\mathrm{a}}(t) - u(t) - \boldsymbol{B^{\#}}_{\mathrm{ob}}\boldsymbol{L}\boldsymbol{C}_{\mathrm{ob}}\boldsymbol{x}_{\mathrm{e}}(t). \tag{2.31}$$

In particular, the estimated disturbance force for the SISO system is expressed as

$$\hat{f}_{\mathrm{dis}} = K_{\tau\mathrm{n}}I_{\mathrm{a}} - K_{\tau\mathrm{n}}I^{\mathrm{ref}} - \boldsymbol{B^{\#}}_{\mathrm{ob}}\boldsymbol{L}\boldsymbol{C}_{\mathrm{ob}}\boldsymbol{x}_{\mathbf{e}}(t), \tag{2.32}$$

$$\hat{f}_{\mathrm{dis}}^{\mathrm{LPF}} = \frac{g_{\mathrm{dob}}}{s + g_{\mathrm{dob}}}\hat{f}_{\mathrm{dis}}, \tag{2.33}$$

where

$$\boldsymbol{B}_{\mathrm{ob}}^{\#} = (\boldsymbol{B}_{\mathrm{ob}}^{\mathrm{T}}\boldsymbol{B}_{\mathrm{ob}})^{-1}\boldsymbol{B}_{\mathrm{ob}}^{\mathrm{T}} = \begin{bmatrix} 0 \\ M_{\mathrm{n}} \end{bmatrix}^{\mathrm{T}}, \tag{2.32a}$$

$$\boldsymbol{x} = \begin{bmatrix} q^{\mathrm{res}} \\ \dot{q}^{\mathrm{res}} \end{bmatrix}, \hat{\boldsymbol{x}} = \begin{bmatrix} \hat{q}^{\mathrm{res}} \\ \hat{\dot{q}}^{\mathrm{res}} \end{bmatrix}, \boldsymbol{x}_{\mathrm{e}} = \begin{bmatrix} q^{\mathrm{res}} - \hat{q}^{\mathrm{res}} \\ \dot{q}^{\mathrm{res}} - \hat{\dot{q}}^{\mathrm{res}} \end{bmatrix}, \tag{2.32b}$$

$$\boldsymbol{A}_{\mathrm{p}} = \begin{bmatrix} 0 & 1 \\ 0 & 0 \end{bmatrix}, \boldsymbol{A}_{\mathrm{ob}} = \begin{bmatrix} 0 & 1 \\ 0 & 0 \end{bmatrix}, \tag{2.32c}$$

$$\boldsymbol{B}_{\mathrm{p}} = \begin{bmatrix} 0 \\ \frac{1}{M} \end{bmatrix}, \boldsymbol{B}_{\mathrm{ob}} = \begin{bmatrix} 0 \\ \frac{1}{M_{\mathrm{n}}} \end{bmatrix}, \tag{2.32d}$$

$$\boldsymbol{C}_{\mathrm{p}} = \begin{bmatrix} 1 \\ 0 \end{bmatrix}^{\mathrm{T}}, \boldsymbol{C}_{\mathrm{ob}} = \begin{bmatrix} 1 \\ 0 \end{bmatrix}^{\mathrm{T}}, \tag{2.32e}$$

$$\boldsymbol{L} = \begin{bmatrix} l_1 \\ l_2 \end{bmatrix}. \tag{2.32f}$$

A transfer function from $\ddot{q}^{\mathrm{ref}}$ to $\ddot{q}^{\mathrm{res}}$ is described as

$$\ddot{q}^{\mathrm{res}} = \frac{\xi(s(s^2 + sl_1 + l_2) + l_2 g_{\mathrm{dob}})}{Ms(s^2 + sl_1 + l_2) + \xi l_2 g_{\mathrm{dob}}} \ddot{q}^{\mathrm{ref}} - \frac{1}{M} T_{\mathrm{SEN}}^{\mathrm{DOB}} f_{\mathrm{dis}} - T_{\mathrm{Cosen}}^{\mathrm{DOB}} s\dot{q}^{\mathrm{noise}}. \tag{2.34}$$

Where, ξ, the $T_{\mathrm{SEN}}^{\mathrm{DOB}}$, $T_{\mathrm{Cosen}}^{\mathrm{DOB}}$ and $L^{\mathrm{DOB}}(s)$ are described as

$$\xi = \frac{K_\tau M_{\mathrm{n}}}{K_{\tau \mathrm{n}}}, \tag{2.34a}$$

$$T_{\mathrm{SEN}}^{\mathrm{DOB}} = \frac{1}{1 + L^{\mathrm{DOB}}(s)}, \tag{2.34b}$$

$$T_{\mathrm{Cosen}}^{\mathrm{DOB}} = \frac{L^{\mathrm{DOB}}(s)}{1 + L^{\mathrm{DOB}}(s)}, \tag{2.34c}$$

$$L^{\mathrm{DOB}}(s) = \frac{\xi l_2 g_{\mathrm{dob}}}{Ms(s^2 + sl_1 + l_2)}. \tag{2.34d}$$

If $\xi = 1$, Eq. (2.2) can be simplified as

$$\ddot{q}^{\mathrm{res}} = \ddot{q}^{\mathrm{ref}} - \frac{1}{M} T_{\mathrm{SEN}}^{\mathrm{DOB}} f_{\mathrm{dis}} - T_{\mathrm{Cosen}}^{\mathrm{DOB}} s\dot{q}^{\mathrm{noise}}. \tag{2.35}$$

A block diagram of the full-order DOB is shown in Fig. 2-3. $T_{\mathrm{Sen}}^{\mathrm{DOB}}$, which is called a "Sensitivity function", is an index for disturbance suppression property. Further, $T_{\mathrm{Cosen}}^{\mathrm{DOB}}$, which is called a "Complementary sensitivity function", is an index for noise response property. Both functions are satisfied in the following equation:

$$T_{\mathrm{Sen}}^{\mathrm{DOB}}(s) + T_{\mathrm{Cosen}}^{\mathrm{DOB}}(s) = 1. \tag{2.36}$$

Eq. (2.36) indicates that there is a trade-off between the disturbance suppression property and the noise response property. In other words, the disturbance and noise cannot be eliminated completely in all frequency domains. Commonly, an external force such as the friction force exists in the low frequency domain while noise exists in the high frequency domain. Thus, the operator has to decide the optimal

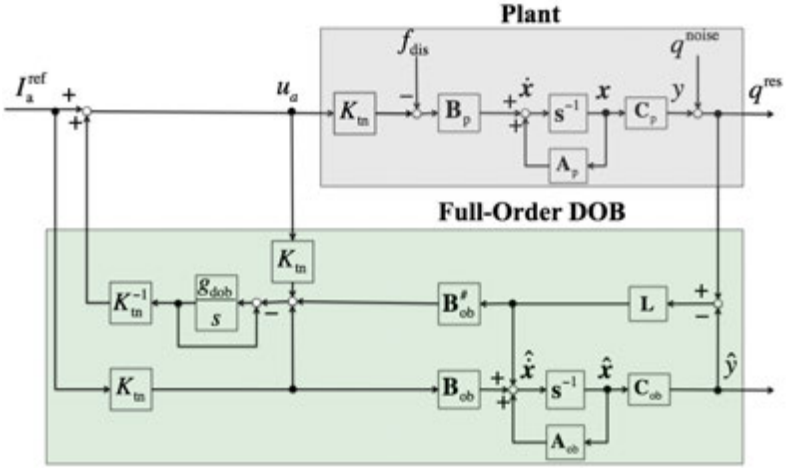

Fig. 2-3: A Block Diagram of Full-Order DOB

observer gains, $\boldsymbol{L}$, for each system in order to produce a robust control system.

Stability and Robustness Conditions

The stability of the full-order DOB can be analyzed by the stable margin theory. The stable margin is analyzed by the transfer function of L^{DOB}. The gain and the phase of L^{DOB} are derived as follows:

$$|L^{\mathrm{DOB}}(s)| = \frac{\xi g_{\mathrm{dob}} l_2}{M\sqrt{(-l_1\omega^2)^2 + (\omega l_2 - \omega^3)^2}}, \tag{2.37}$$

$$\angle L^{\mathrm{DOB}}(s) = \arctan 0 - \arctan \frac{M(\omega l_2 - \omega^3)}{M(-l_1\omega^2)}. \tag{2.38}$$

According to gain margin theory, when a gain equals 1, and a phase is larger than -180°, the system will be stable. Then, the relationships among the gain crossover frequency, ω_{gc} and the observer gain l_1 and the l_2 are described as

$$\omega_{\mathrm{gc}} = \frac{\xi}{M} g_{\mathrm{dob}} = \sqrt{2l_2 - l_1^2}, \tag{2.39}$$

$$0 < \omega_{gc} < \sqrt{l_2}. \tag{2.40}$$

Further, according to phase margin theory, when a phase equals -180°, and a gain is lower than 1, the system will be stable. Then, the relationships among l_2, $\omega_{\rm pc}$, $\omega_{\rm gc}$ are expressed as

$$\omega_{\rm pc} = \sqrt{l_2}, \tag{2.41}$$

$$\omega_{\rm gc} < \omega_{\rm pc}. \tag{2.42}$$

Robustness against an uncertain disturbance force is evaluated by using a closed loop transfer function $T_{\rm Cosen}^{\rm DOB}$. Generally, robustness is evaluated by the H norm expressed as

$$||T_{\rm Cosen}^{\rm DOB}||_\infty = \sup_\omega |T_{\rm Cosen}^{\rm DOB}|. \tag{2.43}$$

Therefore, the H norm equals a peak gain. A peak gain can be derived by calculating the condition of the extremal value as follows:

$$\frac{d(|T_{\rm Cosen}^{\rm DOB}(j\omega)|)}{d\omega} = 0. \tag{2.44}$$

By calculating Eq. (2.45), a peak frequency can be obtained as follows:

$$\omega_{\rm p} = \frac{\sqrt{\omega_{\rm gc}^2 + \sqrt{\omega_{\rm gc}^4 - 3\omega_{\rm pc}^4 + 6\omega_{\rm gc}\omega_{\rm pc}^2(\sqrt{2\omega_{\rm pc^2-\omega_{gc}^2}})}}}{\sqrt{3}}. \tag{2.45}$$

Finally, a peak gain can be obtained as follows:

$$|T_{\rm Cosen}^{\rm DOB}(j\omega_{\rm p})| = \frac{\omega_{\rm gc}\omega_{\rm pc}^2}{\sqrt{(-\omega_{\rm p}^3 + \omega_{\rm p}\omega_{\rm pc}^2)^2 + (\omega_{\rm gc}\omega_{\rm pc}^2 - \omega_{\rm p}^2\sqrt{2\omega_{\rm pc}^2 - \omega_{\rm gc}^2})^2}}. \tag{2.46}$$

When a peak gain is lower than 1, robust stability is especially guaranteed because of a small gain theorem.

$$|T_{\rm Cosen}^{\rm DOB}(j\omega_{\rm p})| < 1. \tag{2.47}$$

2.3.4 The Minimum-Order DOB

If the position signal, q can be measured by a sensing device, and the velocity, $\dot{q}$, is calculated by the differentiation of the position signal, q and $\dot{q}$ would not need to be estimated using the observer. Therefore, the disturbance force estimation can be obtained in a simpler way. However, differentiating the value of the position signal amplifies the noise in the high frequency domain because of quantization

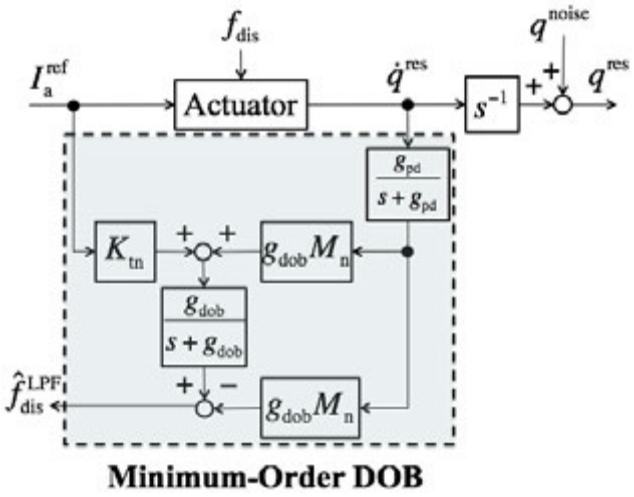

Fig. 2-4: Block Diagram of Minimum-Order DOB

error. Therefore, in order to decrease amplified high frequency noise, pseudo-differentiation is applied. Pseudo-differentiation can suppress high frequency noise by the low-pass filter. Then, the disturbance force estimation by the minimum-order DOB is expressed as

$$\hat{f}_{\mathrm{dis}} = K_{\tau \mathrm{n}} I_{\mathrm{a}}^{\mathrm{ref}} - M_{\mathrm{n}} g_{\mathrm{dob}} \ddot{q}, \tag{2.48}$$

$$\hat{f}_{\mathrm{dis}}^{\mathrm{LPF}} = \frac{g_{\mathrm{dob}}}{s+g_{\mathrm{dob}}} \hat{f}_{\mathrm{dis}}. \tag{2.49}$$

A block diagram of the Eq. (2.48) and Eq. (2.49) is shown in Fig. 2-4 The transfer function of acceleration control with the DOB is expressed as

$$\ddot{q}^{\mathrm{res}} = \frac{\xi(s+g_{\mathrm{dob}})(s+g_{\mathrm{pd}})}{s(s+g_{\mathrm{pd}})+\xi g_{\mathrm{dob}} g_{\mathrm{pd}}} \ddot{q}^{\mathrm{ref}} - T_{\mathrm{Sen}}^{\mathrm{DOB}} - T_{\mathrm{Cosen}}^{\mathrm{DOB}} \ddot{q}^{\mathrm{noise}}, \tag{2.50}$$

where L_{DOB} is

$$L_{\mathrm{DOB}}(s) = \frac{\xi g_{\mathrm{dob}} g_{\mathrm{pd}}}{s(s+g_{\mathrm{pd}})}. \tag{2.51}$$

As shown in Eq. (2.51), the disturbance force compensation performance depends on g_{dob} and g_{pd}. In addition, $T_{\mathrm{Sen}}^{\mathrm{DOB}}$ equals a one-order high pass filter. Analysis of the stability and robustness of the minimum-order DOB [22] by using a characteristic polynomial of by using a characteristic polynomial

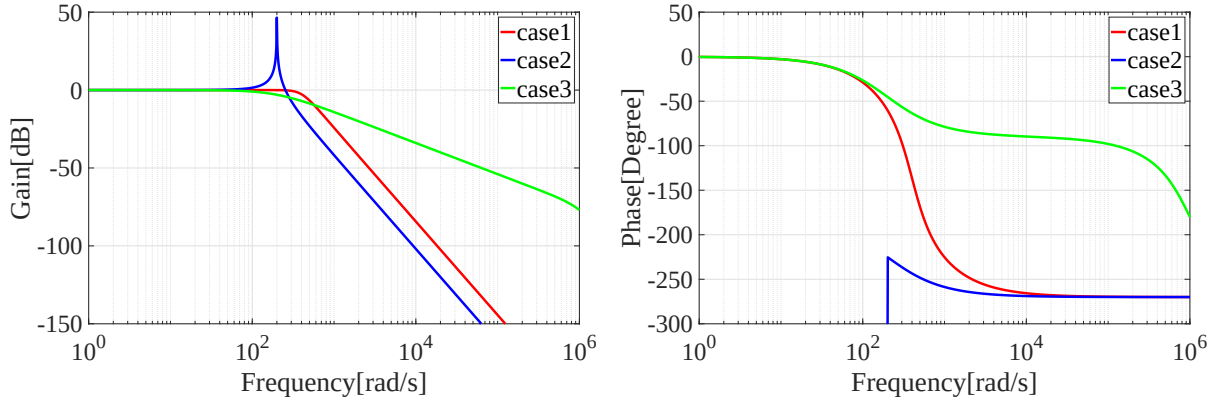

(a) Gain Plot (b) Phase Plot

Fig. 2-5: Bode Plot of Full-order DOB's $T_{\text{Cosen}}^{\text{DOB}}$

of $T_{\text{Sen}}^{\text{DOB}}$ (or $T_{\text{Cosen}}^{\text{DOB}}$) can be expressed as

$$C_{\text{h}}(s) = s^2 + g_{\text{pd}}s + g_{\text{pd}}g_{\text{dob}}. \tag{2.52}$$

The natural frequency and damping coefficient of Eq. (3.3) are

$$\omega_{\text{n}} = \sqrt{g_{\text{pd}}g_{\text{dob}}}, \tag{2-52a}$$

$$\zeta = \frac{g_{\text{pd}}}{2\sqrt{g_{\text{pd}}g_{\text{dob}}}}. \tag{2-52b}$$

If $\zeta \geq 0.707$, then

$$g_{\text{dob}} \leq \frac{g_{\text{pd}}}{2}. \tag{2.53}$$

2.3.5 Perfomance Comparison

The performances of the co-sensitivity function, $T_{\text{DOB}}^{\text{Cosen}}$ for both types DOBs are compared using the simulations. Both simulations are created using Matlab under three different gains. Table 2.1 shows the simulation parameters while Fig. 2-5 and Fig. 2-6 show the simulation results. As shown in the simulation results, stability is guaranteed by using the aforementioned stability conditions. However, the gradient of the plots in the full-order DOB is larger than that in the minimum-order DOB. This is because the filter is designed as a second-order high-pass filter. Thus, the noise effect suppression performance

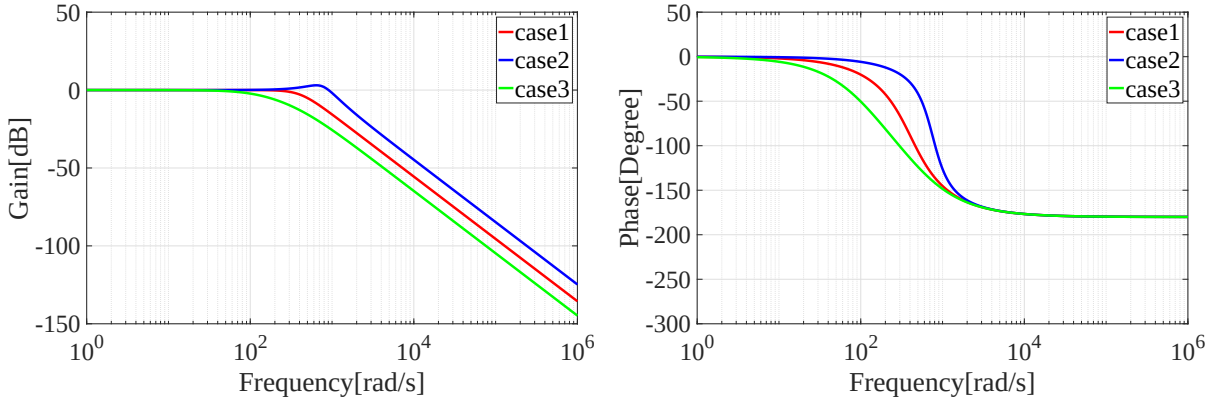

(a) Gain Plot (b) Phase Plot

Fig. 2-6: Bode Plot of Minimum-order DOB's $T_{\text{Cosen}}^{\text{DOB}}$

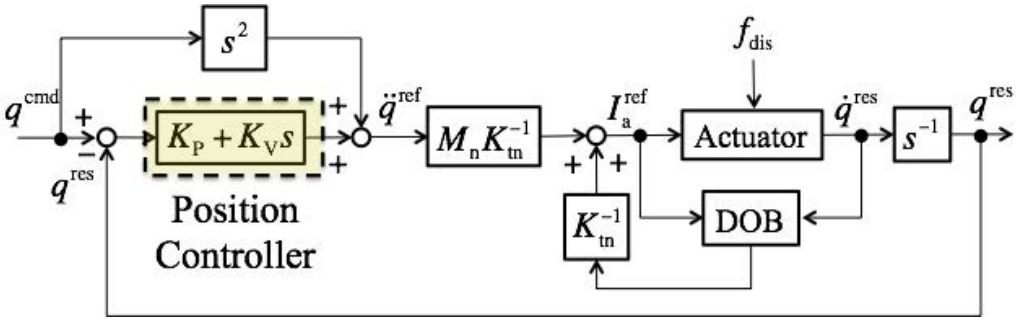

Fig. 2-7: Block Diagram of Acceleration Control Based Position control with a DOB

is improved by the full-order DOB. However, the stability conditions are severe compared to those of the minimum-order DOB. Thus, both types of DOBs have advantages as well as disadvantages, which means that the operator would need to choose a type for application.

2.3.6 Robust Acceleration Control Based Position Control

After the DOB is applied to the position control method to improve robustness, acceleration control is implemented. A block diagram of a robust acceleration-based position control method with the DOB is shown in Fig. 2-7. In Fig. 2-7, low frequency disturbance is compensated by the DOB while high frequency disturbance is attenuated by the pole calculated by position gain K_{p} and velocity gain K_{v}. If the full-order DOB is used for robust position control, the transfer function from the position command

Table 2.1: Simulation Parameters for Two Types DOB

Descriptions	**Parameters**	**Values**			**Units**
		Case1	Case2	Case3	
Design Parameters for Full Order DOB					
Cut-off Frequency of the LPF for the DOB	g_{dob}	300			$\mathrm{rad/sec}$
Gain Cross Over Frequency	ω_{gc}	300			$\mathrm{rad/sec}$
Phase Cross Over Frequency	ω_{pc}	550	300	60000	$\mathrm{rad/sec}$
Peak Gain	$\lvert T^{\mathrm{DOB}}_{\mathrm{Cosen}}\rvert(\omega_{\mathrm{p}})$	-0.0032	∞	-45.3	$\mathrm{rad/sec}$
Observer Gain	l_1	751.7	200	$8485.3 * 10$	s^{-1}
Observer Gain	l_2	$3025.0 * 10^2$	$4000.0 * 10$	$3600.0 * 10^6$	s^{-2}
Cut-Off Frequency	ω_{cut}	408.8	271.2	200.0	$\mathrm{rad/sec}$
Design Parameters for Minimum Order DOB					
Cut-off Frequency of the LPF for the DOB	g_{dob}	289	1000	100	$\mathrm{rad/sec}$
Cut-off Frequency of Pseudo Differentiation	g_{pd}	578			$\mathrm{rad/sec}$
Cut-off Frequency	ω_{cut}	408.7	760.3	240.4	$\mathrm{rad/sec}$
Mechanical parameters					
Actuator Mass	M	0.5			kg
Actuator Nominal Mass	M_{n}	0.5			kg
Torque Constant	K_{t}	33.0			$\mathrm{N/A}$
Nominal Torque Constant	K_{tn}	33.0			$\mathrm{N/A}$

to the position response is expressed as

$$\ddot{q}^{\mathrm{res}} = \frac{\xi s^2 AB(K_p + K_v s + s^2)}{A(\xi K_v l_2 s + \xi K_p B) + s(l_2 + K_v s + s^2)(\xi g_{\mathrm{dob}} l_2 + Ms(l_2 + l_1 s + s^2))}\ddot{q}^{\mathrm{cmd}} - \frac{1}{M}T^{\mathrm{PC}}_{\mathrm{SEN}} f_{\mathrm{dis}} - T^{\mathrm{PC}}_{\mathrm{Cosen}} s\dot{q}^{\mathrm{noise}} \quad , \tag{2.54}$$

where

$$A = g_{\mathrm{dob}} l_2 + s(l_2 + sl_1 + s^2), \quad B = l_2 + s^2. \tag{2.54a}$$

The open loop transfer function of the robust position control method can be expressed as:

$$L^{\mathrm{PC}}(s) = \frac{\xi\left(g_{\mathrm{dob}} l_2\left(K_p\left(l_2+s^2\right)+s\left(K_v l_2+K_v s+l_2+s^2\right)\right)\right)}{M s^2\left(s\left(K_v+s\right)+l_2\right)\left(s\left(l_1+s\right)+l_2\right)} + \frac{\xi(s(l_1+s)+l_2)\left(K_p\left(l_2+s^2\right)+K_v l_2 s\right)}{M s(s(K_v+s)+l_2)(s(l_1+s)+l_2)} \quad . \tag{2.55}$$

Likewise, if the minimum-order DOB is used for position control, the transfer function from the position command to the position response is expressed as

$$\ddot{q}_{\mathrm{m}} = \frac{\xi(s+g_{\mathrm{dob}})(s^2+K_{\mathrm{d}}s+K_{\mathrm{p}})}{s^2(s+\xi g_{\mathrm{dob}})+\xi(s+\xi g_{\mathrm{dob}})(K_{\mathrm{d}}s+K_{\mathrm{p}})}\ddot{q}^{\mathrm{cmd}} - \frac{1}{M}T^{\mathrm{pc}}_{\mathrm{Sen}} f_{\mathrm{dis}} - T^{\mathrm{pc}}_{\mathrm{Cosen}} s\dot{q}^{\mathrm{noise}}. \tag{2.56}$$

The open loop transfer function of the robust position control method can be expressed as

$$L^{\mathrm{PC}}(s) = \frac{\xi g_{\mathrm{pd}} g_{\mathrm{dob}} s^2 + \xi(s+g_{\mathrm{pd}})(s+g_{\mathrm{dob}})(K_{\mathrm{d}}s+K_{\mathrm{p}})}{s^3(s+g_{\mathrm{pd}})} \quad . \tag{2.57}$$

Bode plots of the co-sensitivity function, $T^{\mathrm{pc}}_{\mathrm{Cosen}}$, for both types of DOBs are shown in Fig. 2-8 and Fig. 2-9. Simulation parameters are shown in Table 2.1. From the both bode plot results, the robustness of $T^{\mathrm{dob}}_{\mathrm{Cosen}}$ is also guaranteed in case 1. Correspondingly, the noise suppression performance is confirmed through the experiment. Position control is applied to an oil pressure-based actuator. Generally, the oil pressure-based actuator has a head loss and a friction force as the disturbance force. Therefore, the total disturbance force is expressed as

$$f_{\mathrm{dis}} = f^{\pm}_{\mathrm{fric}} + K_{\mathrm{lin}}\dot{q}\mathrm{sgn}(\dot{q}) + K_{\mathrm{sin}}\dot{q}^2. \tag{2.58}$$

A position command signal for position control is set to a sin wave expressed as

$$q^{\mathrm{cmd}} = \mathrm{Amp}\sin(2.0\pi f t), \tag{2.59}$$

Where, Amp is the amplitude, f is the frequency, and t is the moving time. Each parameter is set to Amp $= 0.0005$(m), $f = 1.0$(Hz), and $1.0 < t \leq 6.0$(sec) respectively. In addition, a white noise is included in the simulation with an amplitude of $1.0 \cdot 10^{-6}(\mathrm{m})$. Control parameters are set to those in case 1, as described in Table 2.1. Experimental results of position control using the full-order DOB and the minimum-order DOB are shown in Fig. 2-10(a) and Fig. 2-10(b). The upper part shows the position response, the middle part shows the velocity response, and the bottom part shows the estimated disturbance force. From the results, it appears that both DOBs can control the position even if the disturbance force is included in the system. However, the noise suppression effect of the full-order DOB is better than that of the minimum-order DOB due to the second-order low-pass filter. In addition,

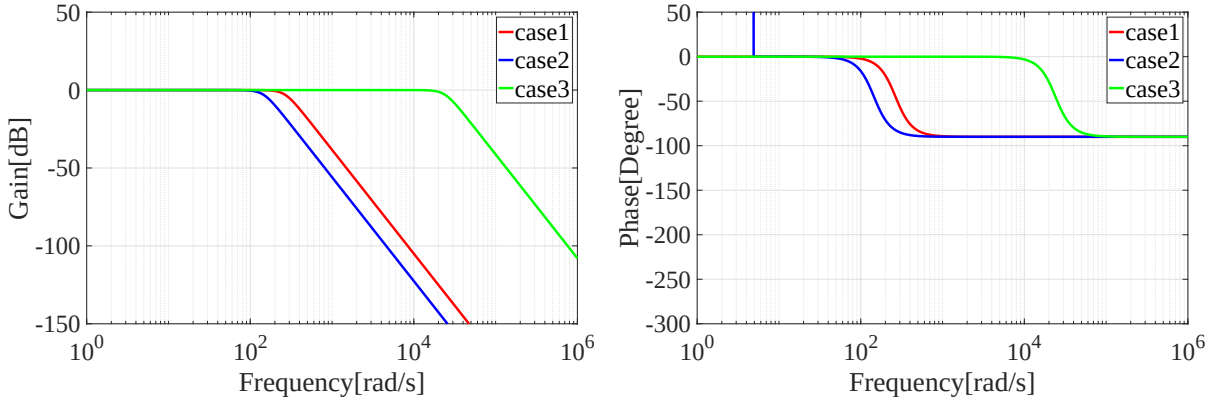

(a) Gain Plot (b) Phase Plot

Fig. 2-8: Bode Plot of Full-order DOB's Co-sensitivity Function for Position Control

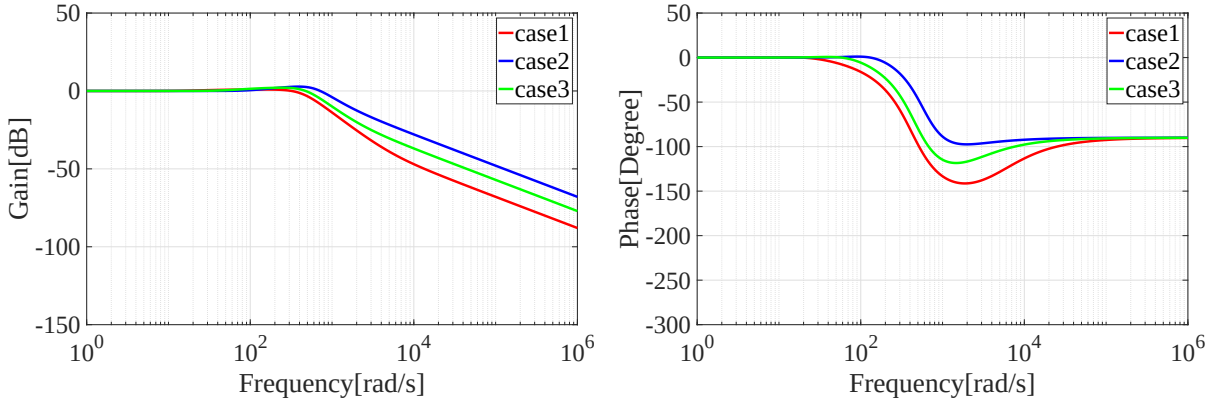

(a) Gain Plot (b) Phase Plot

Fig. 2-9: Bode Plot of Minimum-order DOB's Co-sensitivity Function for Position Control

the noise effect also influences the estimated disturbance force. From the results, it appears that the noise suppression performance improves with the use of the full-order DOB. However, the stability and robustness conditions are severe compared with those of the minimum-order DOB.

2.3.7 Robust Force Control based on the DOB and RFOB

Force control is required to measure the reaction force from the environment. Generally, a force sensor is used for force sensing and determining whether force control is achieved. However, it is difficult to use the force sensor for certain industry applications such as medical operations or operations in civil engineering fields. Force control without the use of a force sensor is an effective solution for avoiding

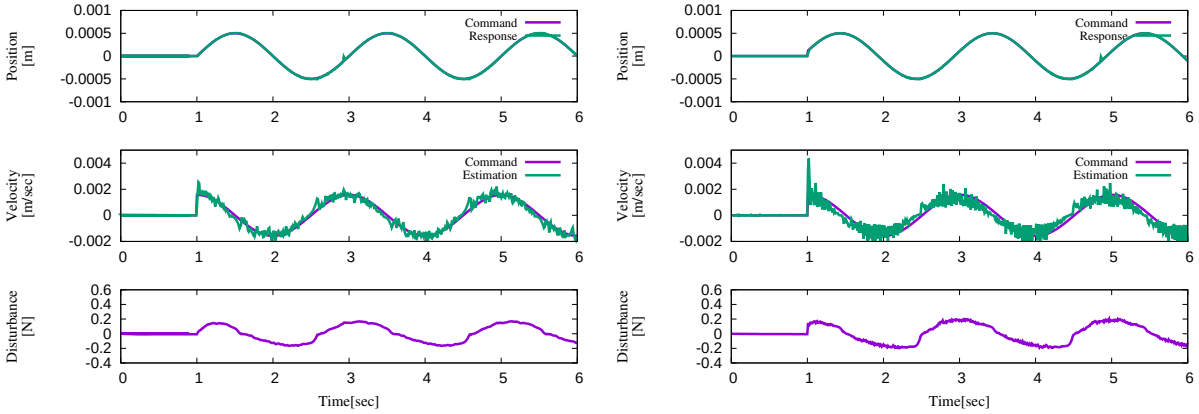

(a) Full-Order DOB (b) Minimum-Order DOB

Fig. 2-10: Experimental Results of Position Control; Upper Part: Position Response, Middle Part: Velocity Response, Bottom Part: Estimated Disturbance Force by DOB

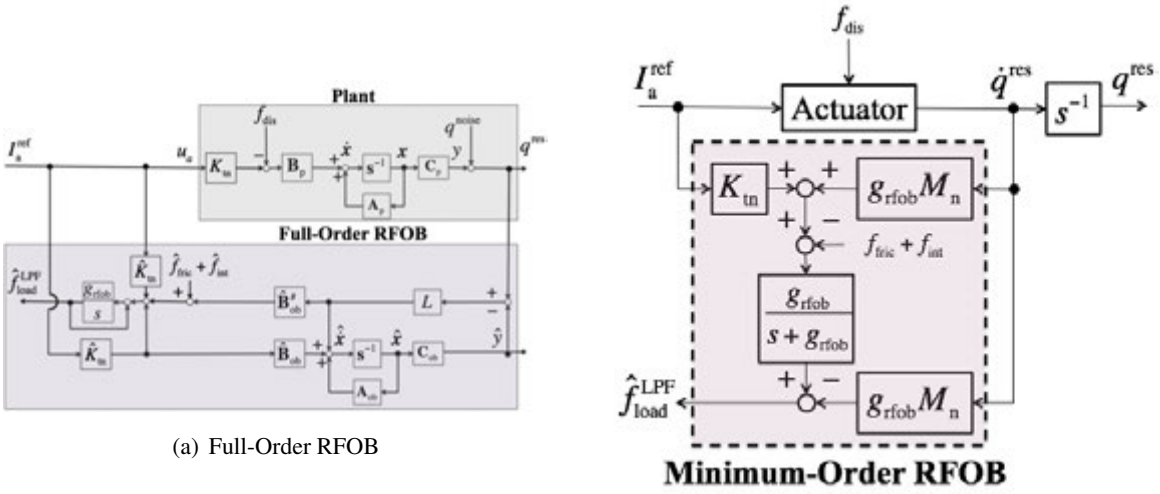

(a) Full-Order RFOB

(b) Minimum-Order RFOB

Fig. 2-11: Block Diagram of an RFOB

constraints to applications. In this section, the RFOB [19, 23], which can facilitate force estimations without the use of a force sensor, is introduced, followed by descriptions of the robust force control strategy, the bode plot simulations, and the implementation of the force control experiments.

Reaction Force Observer (RFOB)

The reaction force estimation is similar to the disturbance force estimation. If the reaction force consists of only the load force from the environment, the reaction force estimation using the full-order

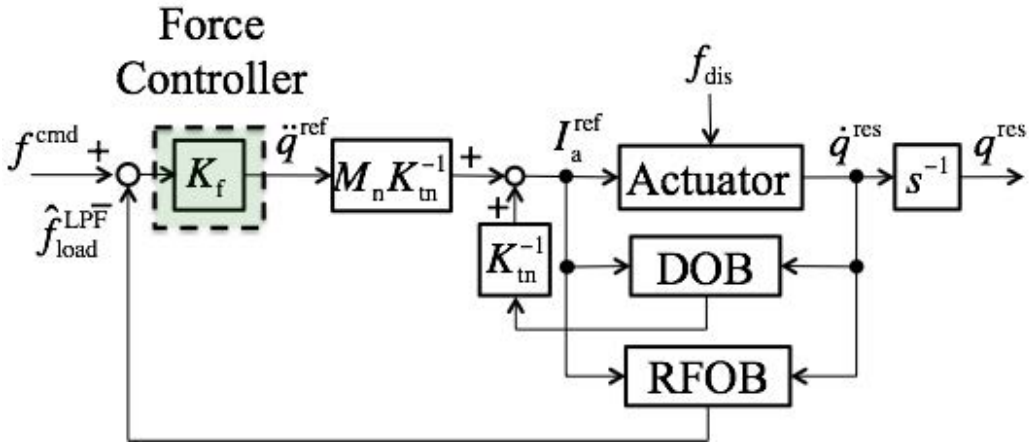

Fig. 2-12: Block Diagram of Acceleration Control Based Force control with a DOB and an RFOB

RFOB is calculated as

$$\hat{f}_{\mathrm{load}} = \hat{K}_\tau I_{\mathrm{a}} - \hat{K}_\tau I^{\mathrm{ref}} - \hat{\boldsymbol{B}}_{\mathrm{ob}}^{\#}\boldsymbol{L}\boldsymbol{C}_{\mathrm{ob}}\boldsymbol{x}_{\mathrm{e}}(t) - \hat{f}_{\mathrm{fric}} - \hat{f}_{\mathrm{int}}, \tag{2.60}$$

$$\hat{f}_{\mathrm{load}}^{\mathrm{LPF}} = \frac{g_{\mathrm{rfob}}}{s + g_{\mathrm{rfob}}}\hat{f}_{\mathrm{load}}, \tag{2.61}$$

where $\hat{K}_\tau$ is the identified torque coefficient, $\hat{\boldsymbol{B}}_{\mathrm{ob}}$is the matrix of the identified actuator mass, $\hat{f}_{\mathrm{int}}$ is the internal force, and $\hat{f}_{\mathrm{fric}}$ is the friction force. Here, $\hat{K}_\tau$ and $\hat{\boldsymbol{B}}_{\mathrm{ob}}$ are defined as

$$\hat{K}_\tau = K_{\tau\mathrm{n}} - \Delta\hat{K}_\tau, \tag{2.60a}$$

$$\hat{\boldsymbol{B}}_{\mathrm{ob}} = \begin{bmatrix} 0 \\ \frac{1}{\hat{M}} \end{bmatrix}, \hat{\boldsymbol{B}}_{\mathrm{ob}}^{\#} = \begin{bmatrix} 0 \\ \hat{M}_{\mathrm{n}} \end{bmatrix}^{\mathrm{T}}, \tag{2.60b}$$

$$\hat{M} = M_{\mathrm{n}} - \Delta\hat{M}. \tag{2.60c}$$

Likewise, the minimum-order RFOB can be expressed as

$$\hat{f}_{\mathrm{load}} = \hat{K}_\tau I_{\mathrm{a}} - M_{\mathrm{n}}\ddot{q}^{\mathrm{res}} - \hat{f}_{\mathrm{fric}} - \hat{f}_{\mathrm{int}}. \tag{2.62}$$

Block diagrams of both types of RFOBs are shown in Fig. 2-11.

Table 2.2: Force Gains for the Bode Plot Simulation of $T^{\mathrm{FC}}_{\mathrm{Cosen}}$

Descriptions	**Parameters**	**Values**			**Units**
		Case1	Case2	Case3	
Parameters for the force controller					
Force Gains	K_{f}	50.0	100.0	1.0	s^{-2}

Controller Design

If the mass variation, ΔM, and the torque ripple, ΔK_{t}, are small enough to be ignored, both parameters become equal to the nominal values of M_{n} and K_{tn}. Furthermore, if the friction compensation was applied to the control system, the influence of the friction force can be ignored. Then, the estimated load force, $\hat{f}_{\mathrm{load}}$, will be the same as the environment reaction force defined as

$$f_{\mathrm{load}} = K_{\mathrm{env}}(q_{\mathrm{env}} - q^{\mathrm{res}}) + D_{\mathrm{env}}(\dot{q}_{\mathrm{env}} - \dot{q}^{\mathrm{res}}), \tag{2.63}$$

where q_{env} is the equilibrium point of the environment and $\dot{q}_{\mathrm{env}}$ is the velocity of the equilibrium point. A load force value is obtained by the RFOB instead of the force sensor's measurement. The transfer function from the force command to the load force can be expressed as

$$\frac{\hat{f}_{\mathrm{load}}}{f^{\mathrm{cmd}}} = T^{\mathrm{fc}} = \frac{L^{\mathrm{fc}}_{\mathrm{dob}}}{1 + L^{\mathrm{fc}}_{\mathrm{dob}}}. \tag{2.64}$$

In the case of the full-order RFOB, the open loop transfer function of force control can be expressed as

$$L^{\mathrm{FC}}(s) = \frac{\xi(sA + l_2 g_{\mathrm{rfob}})C_{\mathrm{f}} A g_{\mathrm{rfob}} Z_{\mathrm{env}}}{s(Ms^2(A^2B + \xi g^2 C_{\mathrm{f}} l_2(s + l_1)) + (A(s + g_{\mathrm{rfob}}) - g_{\mathrm{rfob}}\xi C_{\mathrm{f}} s(s + l_1))(AZ_{\mathrm{env}} + s l_2 g_{\mathrm{rfob}}\xi))} \quad . \tag{2.64a}$$

$$Z_{\mathrm{env}} = D_{\mathrm{env}} s + K_{\mathrm{env}}. \tag{2.64b}$$

$$A = s^2 + l_1 s + l_2, \quad B = s + g_{\mathrm{rfob}}. \tag{2.64c}$$

In addition, the open loop transfer function of the minimum-order RFOB can be expressed as

$$L^{\mathrm{FC}}(s) = \frac{C_{\mathrm{f}} g M \xi (D_{\mathrm{env}} s + K_{\mathrm{env}})}{s\left(Ms(s + \xi g) + (D_{\mathrm{env}} s + K_{\mathrm{env}})\right)} \quad , \tag{2.65}$$

where $g = g_{\mathrm{rfob}} = g_{\mathrm{dob}}$. A block diagram of an acceleration control based force control strategy with the DOB and the RFOB is shown in Fig. 2-12.

Table 2.3: Virtual Impedances for the Bode Plot Simulation of $T_{\mathrm{Cosen}}^{\mathrm{FC}}$

Descriptions	**Parameters**	**Values**			**Units**
		Case1	Case2	Case3	
Virtual Environment Parameters					
Virtual Stiffness	K_{env}	500.0	2000.0	500.0	$\mathrm{N/m}$
Virtual Viscosity	D_{env}	20.0	20.0	1000.0	$\mathrm{N \cdot sec/m}$

Bode Plot Simulations and Experiments

Bode plots of $T_{\mathrm{Cosen}}^{\mathrm{FC}}$ are confirmed through the simulations. Three different force gains and environmental impedances are set for the simulations. Each simulation parameter is described in Table 2.2 and Table 2.3. The design parameters for the DOB and the RFOB are the same as those used in case 1 as described in Table 2.1. Fig. 2-13 shows the simulation results of $T_{\mathrm{Cosen}}^{\mathrm{DOB}}$ in the full-order DOB/RFOB under three different force gains, and Fig. 2-14 shows the simulation results of $T_{\mathrm{Cosen}}^{\mathrm{DOB}}$ in the full-order DOB/RFOB under three different environment impedance. Also, Fig. 2-15 shows the simulation results of $T_{\mathrm{Cosen}}^{\mathrm{DOB}}$ in the minimum-order DOB/RFOB under three different force gains, and Fig. 2-16 shows the simulation results of $T_{\mathrm{Cosen}}^{\mathrm{DOB}}$ in the minimum-order DOB/RFOB under three different environment impedance. In the case of Fig. 2-13, there is a peak when the force gain is set to $K_{\mathrm{f}} = 100.0$ unlike in the case of Fig. 2-15. Thus, the robustness of the force control method depends on the force gain. On the other hand, the simulation results of Fig. 2-14 and Fig. 2-16, the environmental impedance does not increase the peak gain. Therefore, no relationship exists between the environmental impedance and the robustness of the force control system.

The performance of the force control experiments using both types of DOBs and RFOBs is confirmed through the experiments. Force control is installed to the oil pressure-based remote actuator. A linear actuator implementing impedance control is mounted on the endpoint side instead of in an actual environment. Experimental results are shown in Fig. 2-17 and Fig. 2-18. In terms of noise effect suppression, the full-order RFOB shows good performance compared with the minimum-order RFOB in relation to each environment impedance. This result depends on the DOB's filter design. However, the robustness of the force control method with the full-order DOB and RFOB depends on the force gains. In addition, the stability conditions are severe compared with those of the minimum-order DOB and RFOB. Consequently, the operator would need to choose a type for each application.

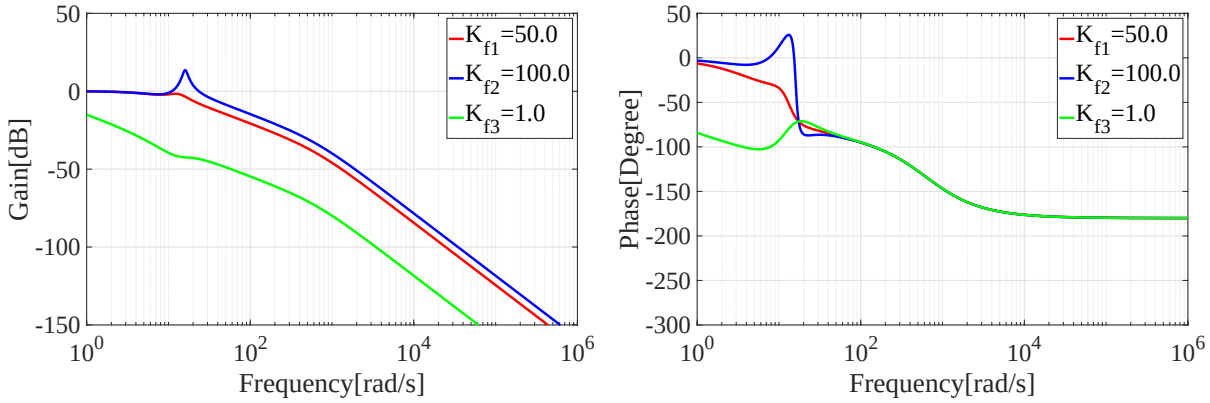

(a) Gain Plot (b) Phase Plot

Fig. 2-13: Bode Plot of Full-Order DOB and RFOB's Co-sensitivity Function of Force Control under Different Three Force Gains

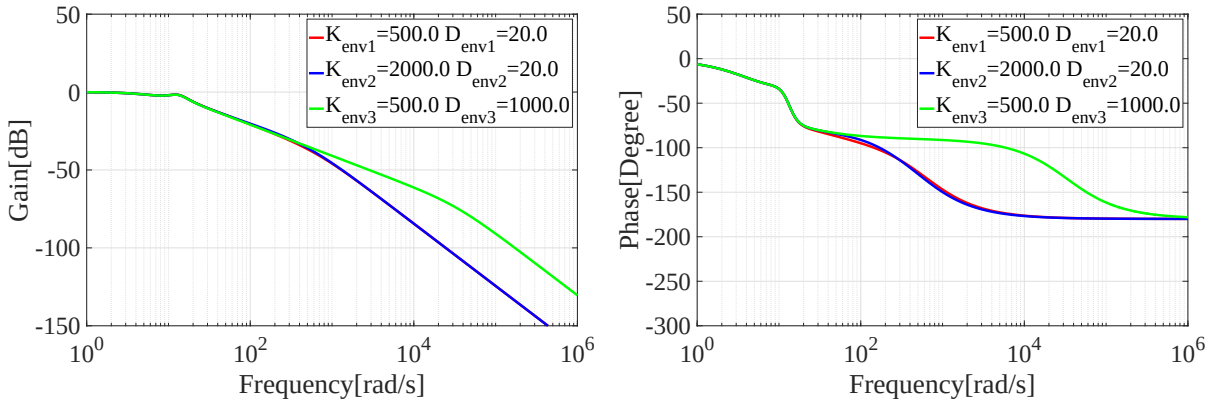

(a) Gain Plot (b) Phase Plot

Fig. 2-14: Bode Plot of Full-Order DOB and RFOB's Co-sensitivity Function of Force Control under Different Three Environmental Impedance

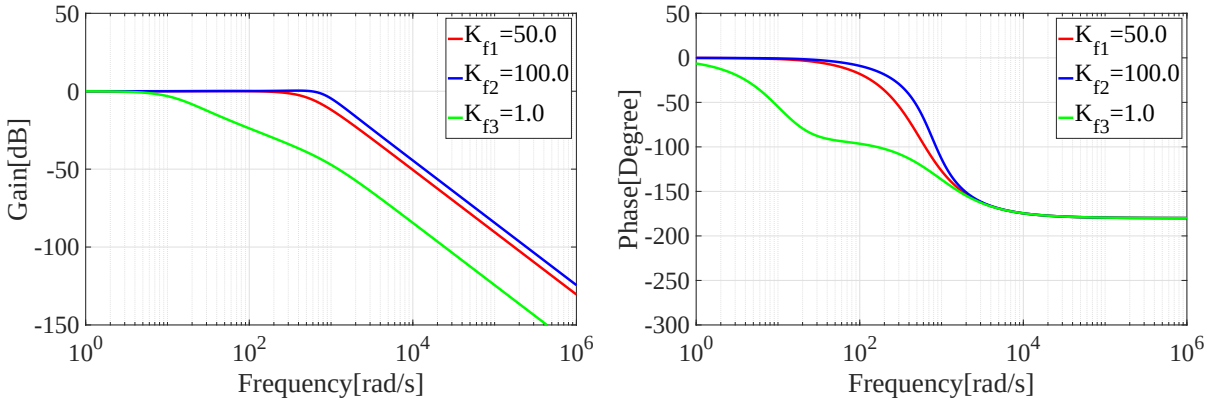

(a) Gain Plot (b) Phase Plot

Fig. 2-15: Bode Plot of Minimum-Order DOB and RFOB's Co-sensitivity Function of Force Control under Different Three Force Gains

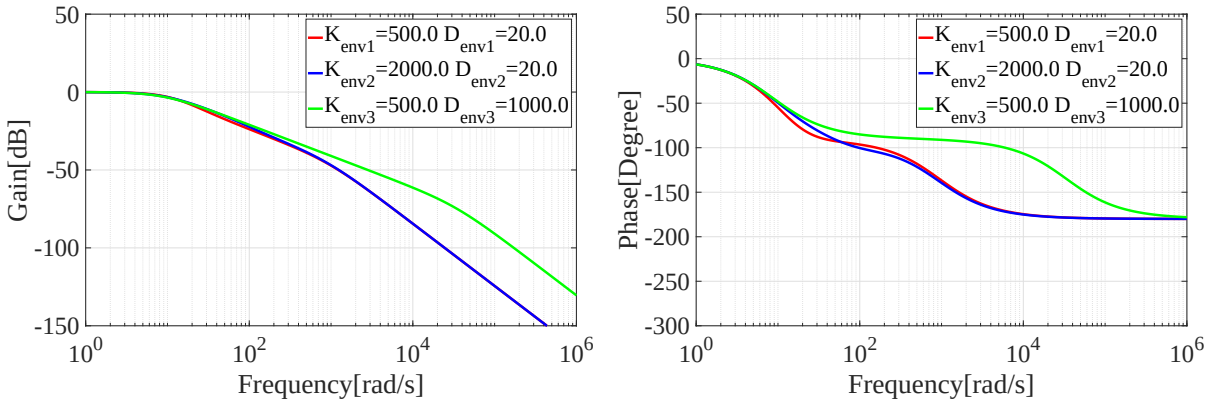

(a) Gain Plot (b) Phase Plot

Fig. 2-16: Bode Plot of Minimum-Order DOB and RFOB's Co-sensitivity Function of Force Control under Different Three Environmental Impedance

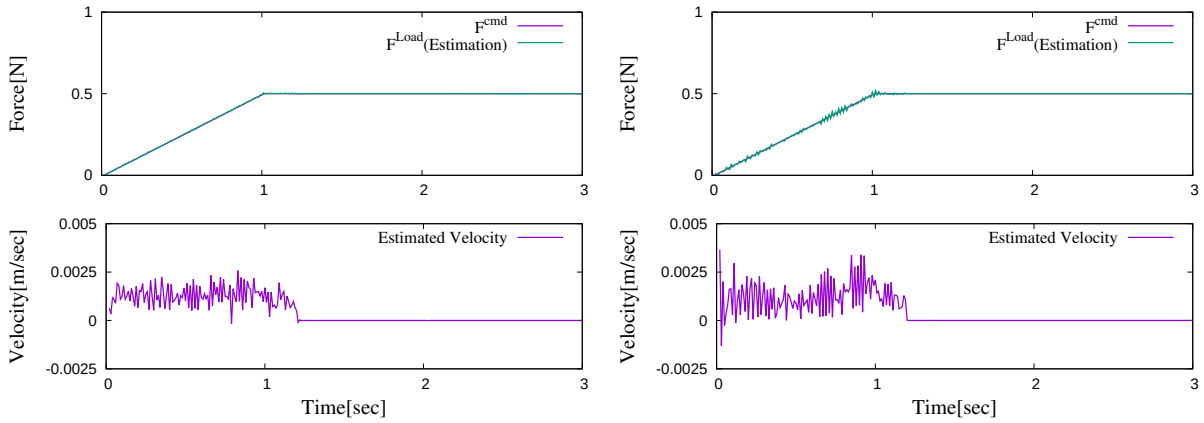

(a) Full-Order DOB and RFOB (b) Minimum-Order DOB and RFOB

Fig. 2-17: Experimental Results of Force Control ($K_{\mathrm{env}} = 500.0, D_{\mathrm{env}} = 20.0$); Upper Part: Reaction Force Response, Bottom Part: Velocity Response

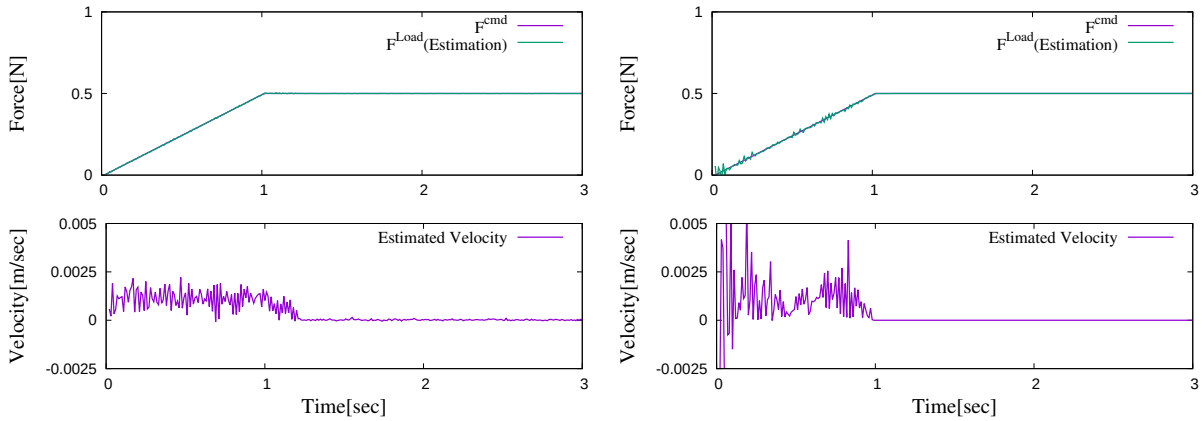

(a) Full-Order DOB and RFOB (b) Minimum-Order DOB and RFOB

Fig. 2-18: Experimental Results of Force Control ($K_{\mathrm{env}} = 2000.0, D_{\mathrm{env}} = 20.0$); Upper Part: Reaction Force Response, Bottom Part: Velocity Response

Chapter 3

Bilateral Control

This chapter describes an acceleration-based bilateral control method. Bilateral control is a remote control method to synchronize the information between a master robot and a slave robot. An operator operates a master robot, which transmits the position and force information to the slave robot. The slave robot also transmits the position and force information to the master robot. Fig. 3-1 shows an outline of the bilateral control method. Details of the bilateral control structure are described in the following sections.

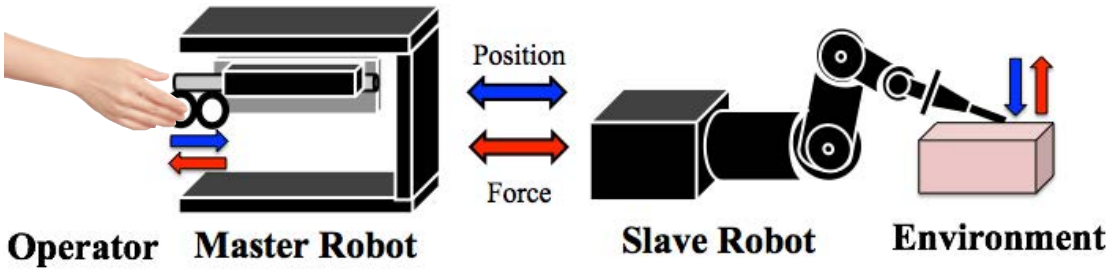

Fig. 3-1: Outline of The Acceleration Control Based Bilateral Control

3.1 Bilateral Control

The control goal of a bilateral control method is expressed as

$$\begin{aligned} q_{\mathrm{m}} - q_{\mathrm{s}} &= 0, \\ \hat{f}_{\mathrm{m}} + \hat{f}_{\mathrm{s}} &= 0, \end{aligned} \tag{3.1}$$

where $\bigcirc_{\mathrm{m}}$ means a master robot and $\bigcirc_{\mathrm{s}}$ means a slave robot. Eq. (3.1) shows how the slave position follows the master position. Additionally, the reaction force of the master robot and the slave robot achieves the action-reaction law. Likewise, the control goal of a scaled bilateral control method is expressed as

$$\begin{aligned} q_{\mathrm{m}} - \alpha q_{\mathrm{s}} &= 0, \\ \hat{f}_{\mathrm{m}} + \beta \hat{f}_{\mathrm{s}} &= 0, \end{aligned} \tag{3.2}$$

where α is the position scaling coefficient and β is the force scaling coefficient. By using the scaled bilateral controller, the operator can amplify the master side position and the reaction force from the environment however he/she wants. This method is effective for operations involving a small target, such as a cellular tissue.

3.1.1 A Bilateral Control with a 4-ch. Controller

Fig. 3-2 shows a 4-ch. controller-based bilateral control method [24]. The DOB is implemented in the master and slave robots. $\ddot{q}_{\mathrm{m,dis}}$ and $\ddot{q}_{\mathrm{s,dis}}$ are the acceleration disturbances, and $C_1, C_2, C_3, C_4, C_5, C_6, C_7$ and C_8 are the controllers for the master and slave robots. The purpose of the bilateral control method is to transmit the position and force information between the master and slave robots. Thus, each controller is set to

$$\begin{aligned} C_{\mathrm{p}} = C_1 = -C_4 = C_8 = C_9, \\ C_{\mathrm{f}} = C_2 = C_3 = C_5 = C_6. \end{aligned} \tag{3.3}$$

The 4-ch. bilateral control structure is shown in Fig. 3-3.

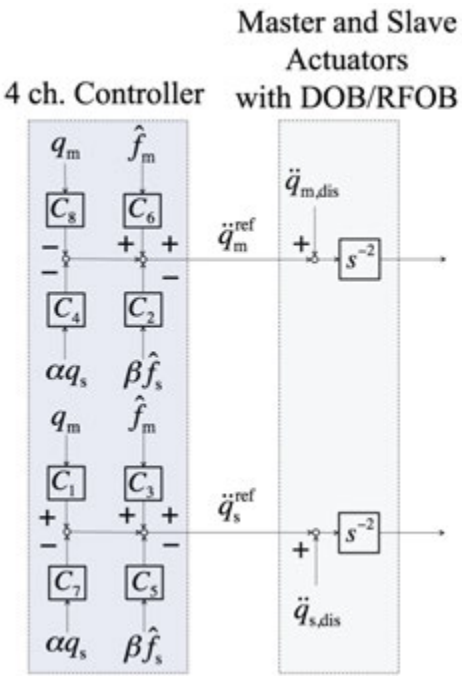

Fig. 3-2: A Block Diagram of 4ch. Bilateral Controller

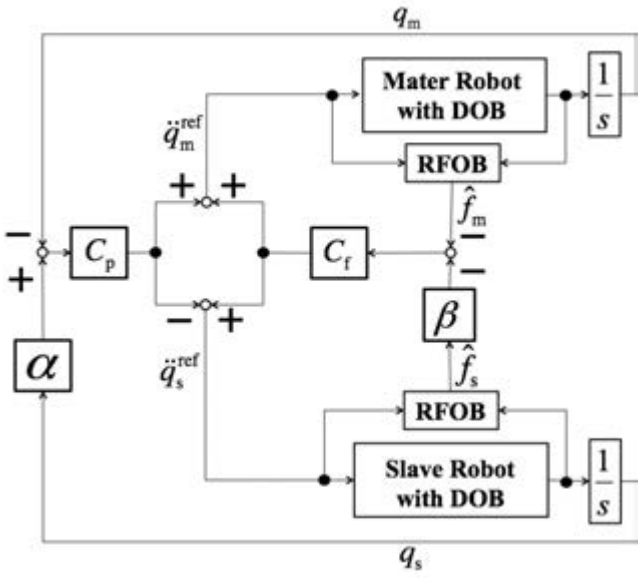

Fig. 3-3: A Block Diagram of Whole Structure of Bilateral Control

3.1.2 Bilateral Control in Modal Space

A modal space coordinate is a mapping function that describes the role of the actuator's function. The coordinate transformation from the joint space to the modal space is realized by a Hadamard matrix as follows:

$$\begin{aligned} \boldsymbol{H} &= \begin{bmatrix} H_{11} & H_{12} \\ H_{21} & H_{22} \end{bmatrix} \\ &= \begin{bmatrix} 1 & -1 \\ 1 & 1 \end{bmatrix}. \end{aligned} \tag{3.4}$$

In the case of a bilateral control method with scaling, the coordinate transformation matrix is described as

$$\boldsymbol{T} = \begin{bmatrix} 1 & -\alpha \\ 1 & \beta \end{bmatrix}. \tag{3.5}$$

Then, the coordinate transformation from the joint space to the modal space is expressed as

$$\boldsymbol{Q} = \boldsymbol{T}\boldsymbol{q}. \tag{3.6}$$

$$\begin{aligned} \begin{bmatrix} Q_{\mathrm{diff}} & F_{\mathrm{diff}} \\ Q_{\mathrm{com}} & F_{\mathrm{com}} \end{bmatrix} &= \begin{bmatrix} 1 & -\alpha \\ 1 & \beta \end{bmatrix} \begin{bmatrix} q_{\mathrm{m}} & \hat{f}_{\mathrm{m}} \\ q_{\mathrm{s}} & \hat{f}_{\mathrm{s}} \end{bmatrix}, \\ &= \begin{bmatrix} q_{\mathrm{m}} - \alpha q_{\mathrm{s}} & \hat{f}_{\mathrm{m}} - \alpha \hat{f}_{\mathrm{s}} \\ q_{\mathrm{m}} + \beta q_{\mathrm{s}} & \hat{f}_{\mathrm{m}} + \beta \hat{f}_{\mathrm{s}} \end{bmatrix}. \end{aligned} \tag{3.7}$$

The above equation describes the modal space of the position and the force response, where Q_{com} is the common mode position, Q_{diff} is the differential mode position, F_{com} is the common mode force, and F_{diff} is the differential mode force. Then, the bilateral control command in modal space is expressed as

$$\begin{aligned} Q_{\mathrm{diff}}^{\mathrm{cmd}} &= 0, \\ F_{\mathrm{com}}^{\mathrm{cmd}} &= 0. \end{aligned} \tag{3.8}$$

Further, the acceleration references in modal space can be expressed as

$$\begin{aligned} s^2 Q_{\mathrm{diff}}^{\mathrm{ref}} &= C_{\mathrm{p}}(Q_{\mathrm{diff}}^{\mathrm{cmd}} - Q_{\mathrm{diff}}^{\mathrm{res}}), \\ s^2 Q_{\mathrm{com}}^{\mathrm{ref}} &= C_{\mathrm{f}}(F_{\mathrm{com}}^{\mathrm{cmd}} + F_{\mathrm{com}}^{\mathrm{res}}). \end{aligned} \tag{3.9}$$

Finally, the acceleration references in joint space are derived as

$$\begin{bmatrix} s^2 Q_{\mathrm{m}}^{\mathrm{ref}} \\ s^2 Q_{\mathrm{s}}^{\mathrm{ref}} \end{bmatrix} = \boldsymbol{T}^{-1} \begin{bmatrix} s^2 Q_{\mathrm{com}}^{\mathrm{ref}} \\ s^2 Q_{\mathrm{diff}}^{\mathrm{ref}} \end{bmatrix}. \tag{3.10}$$

3.1.3 Oblique Coordinate Bilateral Control

The 4-ch. bilateral control scheme is a kind of hybrid control scheme that achieves position and force control. In an ideal situation, each control is achieved with no interference. However, if position scaling and force scaling are applied to the slave robot, then interference would occur. This interference increases the operational force generated from the master robot. An oblique coordinate bilateral control method, proposed by Sakaino *et al.*[20], is one of the methods used to suppress the interference. The hybrid control method implementing oblique coordinate control uses a " Task Jacobian matrix " instead of a coordinate transformation matrix. Here, the task Jacobian matrix is expressed as

$$\boldsymbol{J_t} = \begin{bmatrix} 1 & \alpha \\ 1 & -\beta \end{bmatrix}. \tag{3.11}$$

The mass matrix in modal space called " Task mass matrix " is expressed as

$$\boldsymbol{M_t} = \boldsymbol{J}_{\mathrm{t}} \boldsymbol{M}_{\mathrm{j}} \boldsymbol{J}_{\mathrm{t}}^{-\mathrm{T}} = \begin{bmatrix} M_{\mathrm{qq}} & M_{\mathrm{qF}} \\ M_{\mathrm{Fq}} & M_{\mathrm{FF}} \end{bmatrix}, \tag{3.12}$$

where M_{j} is the mass matrix in joint space. In the case of the oblique coordinate bilateral control between a 1-DoF master robot and a 1-DoF slave robot, the task mass matrix is calculated as

$$\boldsymbol{M}_{\mathrm{t}} = \frac{1}{\alpha M_{\mathrm{mn}} + \beta M_{\mathrm{sn}}} \begin{bmatrix} -\beta M_{\mathrm{sn}} & -\alpha \\ M_{\mathrm{mn}} & -1 \end{bmatrix}. \tag{3.13}$$

The oblique coordinate 4-ch. bilateral control scheme is shown in Fig. 3-4.

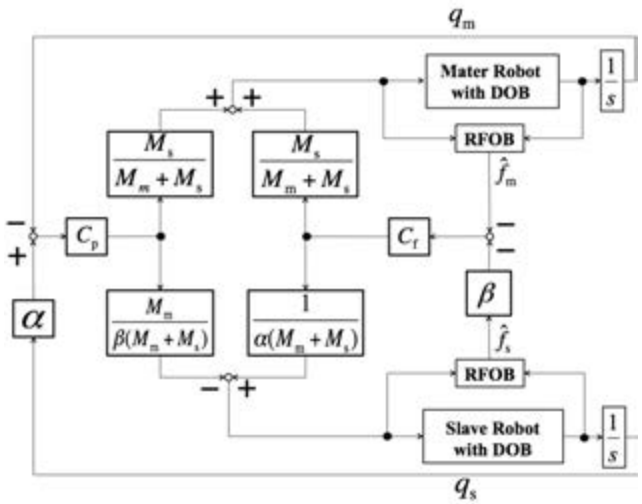

Fig. 3-4: A Block Diagram of An Oblique Bilateral Control

Chapter 4

Development of EHTS-Based Medical Instruments for the NOTES Operation

4.1 Introduction

As technology progresses, human-robot interaction becomes a popular research topic worldwide. In this research domain, there are strong research activities in the development of medical robots due to their many potential advantages and the cooperation between researchers in the medical and engineering fields. Robotics-assisted surgery offer many advantages; for example, robots can obtain the information of bio-tissues more easily, thereby allowing doctors to detect diseases more easily. Moreover, robots can penetrate areas that humans cannot easily access. In addition, robots can achieve a very precise and accurate motion compared to humans. The advantages of tele-operational medical robots have not only motivated researchers around the world to conduct work in this interesting and promising scientific area [25] but also led to the fast-growing research on the specific use of tele-operational medical robots for minimally invasive surgeries (MIS). The MIS is a surgical technique that minimizes the patient's recovery time and pain due to the very small size of the incisions during the surgical procedures [1]. One of the MIS methods is the well-known" Natural Orifice Transluminal Endoscopic Surgery "(NOTES) [3]. Usually, the NOTES technique is utilized to remove a tiny tumor such as cancer tissues or other malignant tumors. In addition, the NOTES method is applied to a suturing operation. The biggest advantage of the NOTES method is that the doctor does not make an incision in the abdomen. In the NOTES procedure, the following three tasks are required for tumor removal: (i) palpation: the doctor uses a palpation probe under an endoscope in order to detect the tumor; (ii) tumor removal: the doctor uses long, flexible tools

such as a forceps with a flexible cable for tumor removal; (iii) suturing operation: the doctor uses long, flexible tools such as a forceps with a flexible cable for suturing. However, the NOTES procedure is only applied to remove a tumor that is near the surface of bio-tissues because its required use of visual information prevents the recognition of tumors hidden within bio-tissues. In addition, the procedure includes some risks in terms of possible damages to the tissue from a large grasping force. Likewise, a large ligating force might break the suturing thread

As the application of haptic sensation to the NOTES method could be an effective solution for improving the performance of palpation, the grasping task, and the suturing task, haptics emerged as a key factor in aiding human-robot interaction. Haptic communication recreates the sense of touch by applying forces, vibrations, or motions to the user. This mechanical stimulation can be used to assist the creation of virtual objects in a computer simulation, to control such virtual objects, and to enhance the remote control of machines and devices (telerobotics). Consequently, by using haptics for medical instruments, a doctor can feel the reaction force from the bio-tissue and conduct the medical operation more safely [26–29]. Bilateral control, which is one of the haptic technologies, can achieve a force and a tactile feedback with very high performance during tele-operations [24, 30].

In addition, position control and haptic sensation through a bilateral control method in a very narrow area, which humans cannot easily access, can be achieved by a remote actuator. A flexible actuator, which consists of a metal wire, a metal tube, and a linear actuator, is a kind of remote actuator [10,11]. The metal wire and the metal tube are connected to the linear actuator, and both position and force information are transmitted to the endpoint of the metal tube. This system is adopted for many applications. Discussing conventional methods for medical applications, Phee *et al.* [12] proposed a master-slave surgical system using a flexible actuator. However, the transmission performance depends on the wire's shape due to non-linear friction[31]. Thus, the precise reaction force from the bio-tissue is difficult to obtain through the flexible actuator. Correspondingly, Do *et al.* proposed a master-slave surgical system using a flexible actuator with non-linear compensation[13]. However, the position encoder needs to be mounted on the endpoint, which increases the size of the endpoint. As a result, the use of the remote actuator leads to the deterioration of haptic sensation.

In order to overcome these problems, Bechet *et al.* proposed a novel remote actuation system called the“ Electro Hydraulic Transmission System (EHTS) ”[32]. This actuation system transmits the position and force information at a remote place by using fluid energy. The friction generated by the EHTS is not influenced by the wire's shape. Thus, the transmission performance can be constant for any wire's

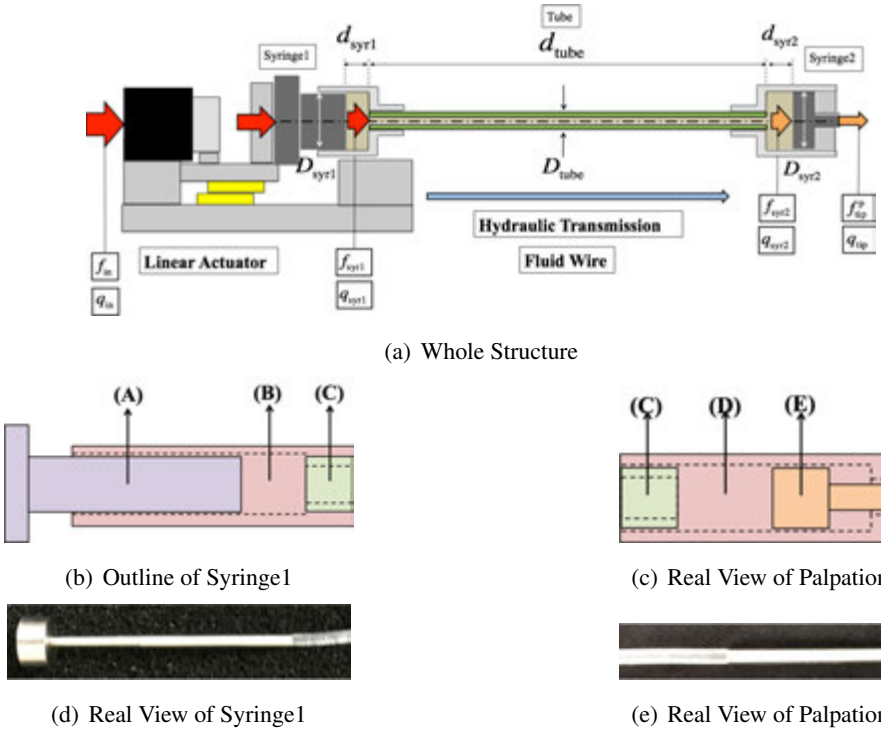

(a) Whole Structure

(b) Outline of Syringe1

(c) Real View of Palpation Probe

(d) Real View of Syringe1

(e) Real View of Palpation Probe

Fig. 4-1: Mechanical Structure of EHTS-based Palpation Probe

shape. Nevertheless, the current study uses a large-sized syringe and force control to confirm the control performance.

In this paper, EHTS-based medical instruments for the NOTES procedure are proposed. The palpation device and slider crank mechanism (SCM)-based forceps are developed, and the position and force transmission system is analyzed. The validity of the proposed forceps is confirmed by the position control, force control, and bilateral control methods, respectively.

The rest of this paper is organized as follows: in Section 4.2, the mechanical models of developed instruments and the modeling of the EHTS are described. This section also describes how the position and force transmission loss of the EHTS does not depend on the wire's posture. In Section 4.3, a control method and the experimental procedures of the position, force, and bilateral control methods are described. In Section 4.4, experimental results of the control performance of both developed instruments are described. In Section 4.5, the discussion of the experimental results is presented. This paper ends with conclusions and recommendations based on the experimental results.

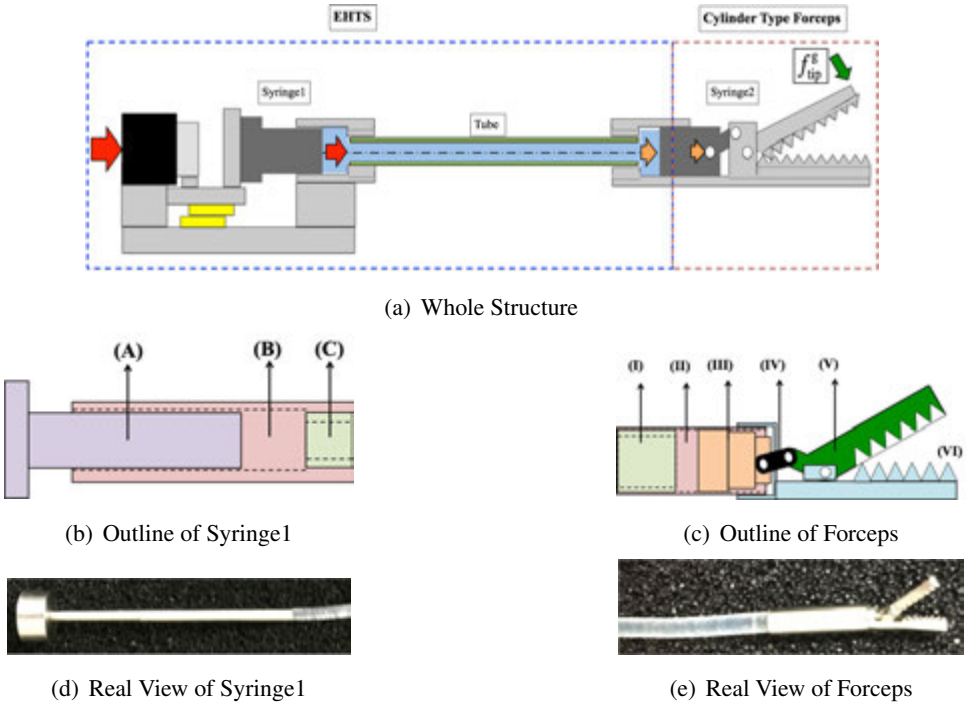

(a) Whole Structure

(b) Outline of Syringe1

(c) Outline of Forceps

(d) Real View of Syringe1

(e) Real View of Forceps

Fig. 4-2: Mechanical Structure of EHTS-based Forceps

4.2 Modeling

In this section, the developed force sensor-less palpation device is described. In 4.2.1, the mechanical design of the developed device and the selection of transmission liquid are explained. In 4.2.2, the EHTS modeling is described. In 4.2.3, the kinematics of the developed forceps is explained. Finally, the design parameters and model identification of the EHTS-based palpation device/forceps are described in 4.2.4.

4.2.1 Mechanical Design

Fig. 4.1 shows the mechanical design of the developed organ palpation device. This device consists of two differently shaped syringes and a rubber tube. The hydraulic transmission system is represented by the scheme in Fig. 4.1(a), where the D is the diameter of the syringe, d is length, $\bigcirc_{\mathrm{syr1}}$ is Syringe1, $\bigcirc_{\mathrm{syr2}}$ is Syringe2, $\bigcirc_{\mathrm{tube}}$ is the tube, $\bigcirc^{\mathrm{p}}$ describes the pushing motion and $\bigcirc^{\mathrm{tip}}$ is the endpoint side. When the motor applies a force, f_{in}, on Syringe 1, the oil transmits an effort,f_{syr1}, to Syringe 2 as f_{syr2}, and a force, $f_{\mathrm{tip}}^{\mathrm{p}}$ is applied. The position and velocity of the motor side, respectively, q_{in} and $\dot{q}_{\mathrm{in}}$, follow the position and velocity of Syringe 1, respectively, q_{syr1} and $\dot{q}_{\mathrm{syr1}}$, which follow the position and

velocity of Syringe 2, respectively, q_{syr2} and $\dot{q}_{\mathrm{syr2}}$, which follow the position and velocity of the endpoint side, respectively, q_{tip} and $\dot{q}_{\mathrm{tip}}$. The first syringe, shown in Fig. 4.1(b), is connected to the actuator (i.e., a linear motor). (A) represents the inner part of the syringe and (B) is the outer part of the syringe. The second syringe (Syringe 2), shown in Fig. 4.1(c), is used for environmental probing. (C) represents the part connected to the rubber tube, (D) is the outer part of the syringe, and (E) is the inner part of the syringe. In particular, (D) is designed so as to refrain (E) from popping out. The real view of both syringes is shown in Fig. 4.1(d) and (e). Both syringes are made from stainless steel (SUS303) and can move through an endoscope. The diameter of the outer syringe (i.e. part (B)) is 2.6 mm.

Further, the mechanical design of the EHTS-based forceps is shown in Fig. 4.1, while the whole system of the developed EHTS-based forceps is shown, in particular, in Fig. 4.1(a). Where, $\bigcirc^{\mathrm{g}}$ describes the grasping motion. The forceps assembly consists of the EHTS and the cylindrical forceps. The liquid is transmitted by the linear actuator in the same way as by the EHTS-based palpation device. Fig. 4.1(b)shows the mechanical outline of Syringe 1, which is utilized. Fig. 4.1(b) is utilized. Fig. 4.1(c) shows the outline of the forceps. The SCM is applied to perform the grasping motion. (I) represents the part connected to the rubber tube, (II) is the outer part of the syringe, (III) is the inner part of the syringe, (IV) is a link that connects part (III) and part (V), (V) is the upper jaw of the forceps, and (VI) is the lower jaw of the forceps. Linear motion is converted into rotary motion by parts (III), (IV), (V), and (VI). Fig. 4.1(d) and Fig. 4.1(e) are the real views of Syringe 1 and the forceps. The syringes and forceps are made from stainless steel (SUS304).The diameter of the forceps (i.e. part (VI)) is 2.6mm

In this research, olive oil is chosen as a transmission liquid for both systems for the following reasons: (i) olive oil is used for medical operations such as those involving fungal infections [33] and umbilical cord care [34]; (ii) olive oil includes vitamin E, which is a natural antioxidant, and thus the human body has a high affinity for it [35]; and (iii) olive oil has a high viscosity, which helps against leakage from the syringes.

4.2.2 Electro-Hydraulic Transmission Modeling

The motion equation of the EHTS for a pushing motion can be derived as

$$f_{\mathrm{syr1}} = \left(\frac{D_{\mathrm{syr1}}}{D_{\mathrm{syr2}}}\right)^2 f_{\mathrm{syr2}} + \frac{\pi D_{\mathrm{syr1}}^2 \rho}{8}(\dot{q}_{\mathrm{syr2}}^2 - \dot{q}_{\mathrm{syr1}}^2) + K_{\mathrm{lin}}\dot{q}_{\mathrm{syr1}} + K_{\mathrm{sin}}\dot{q}_{\mathrm{syr1}}^2 \cdot \mathrm{sgn}(\dot{q}_{\mathrm{syr1}}), \tag{4.1}$$

where the second term is the force transmission loss by the velocity gradient, the third term is the force transmission loss by the liquid viscous friction, and the fourth term is the force transmission loss by the

shape of the flow path called "Singular loss." Here, the coefficient of the viscous friction loss, K_{lin}, and the coefficient of the singular loss, K_{sin} are expressed as

$$K_{\mathrm{lin}} = 8D_{\mathrm{syr1}}^2\pi\mu\left(\frac{1}{D_{\mathrm{syr1}}}+\left(\frac{D_{\mathrm{syr1}}}{D_{\mathrm{tube}}}\right)^2\frac{1}{D_{\mathrm{tube}}}+\frac{1}{D_{\mathrm{syr2}}}\right), \tag{4.2}$$

$$K_{\mathrm{sin}} = \frac{D_{\mathrm{syr1}}^2\rho\pi}{8}\left(\xi_{\mathrm{sc}}\left(\frac{D_{\mathrm{syr1}}}{D_{\mathrm{tube}}}\right)^4+\xi_{\mathrm{se}}\left(\frac{D_{\mathrm{syr1}}}{D_{\mathrm{syr2}}}\right)\right), \tag{4.3}$$

where ξ_{se} means the rapid-expanding loss coefficient, ξ_{sc}means the rapid-contracting loss coefficient, μ means the viscous coefficient of the olive oil, and ρ means the density of the olive oil. In the case of a pulling motion (i.e., $\dot{q}_{\mathrm{syr1}} < 0$), $\bigcirc_{\mathrm{syr1}}$ and $\bigcirc_{\mathrm{syr2}}$ should be exchanged. Then, f_{syr1} and f_{syr2} can be rewritten as

$$f_{\mathrm{syr1}} = f_{\mathrm{in}} + f_{\mathrm{fric,syr1}}, \tag{4.4}$$

$$f_{\mathrm{syr2}} = f_{\mathrm{tip}}^{\mathrm{p}} - f_{\mathrm{fric,syr2}}, \tag{4.5}$$

where $f_{\mathrm{fric,syr1}}$ and $f_{\mathrm{fric,syr2}}$are the Coulomb and viscous friction force generated by Syringe 1 and Syringe 2. In this research, the Coulomb friction model expressed as the following Eq. (4.6) is adopted:

$$f_{\mathrm{fric,i}} = f_{\mathrm{s,i}}^{\pm} + \sigma^{\pm}\dot{q}, \tag{4.6}$$

where i is the number of syringes (i.e., $\bigcirc_{\mathrm{syr1}}$ or $\bigcirc_{\mathrm{syr2}}$), f_{s} is the static friction, σ is the viscous coefficient and the $\bigcirc^{\pm}$ expresses the pushing$(+)$ / pulling$(-)$ motion. In addition, the relation of each velocity can be expressed as the following Eq. (4.7) according to the law of conservation of mass:

$$\dot{q}_{\mathrm{i}} \approx \dot{q}_{\mathrm{syr1}} = \left(\frac{A_{\mathrm{syr2}}}{A_{\mathrm{syr1}}}\right)^2\dot{q}_{\mathrm{syr2}} = \left(\frac{D_{\mathrm{syr2}}}{D_{\mathrm{syr1}}}\right)^2\dot{q}_{\mathrm{syr2}} \approx \dot{q}_{\mathrm{o}}, \tag{4.7}$$

where A is the cross-sectional area of each syringe. In the end, Eq. (4.1) can be rewritten as

$$f_{\mathrm{in}} = \gamma f_{\mathrm{tip}}^{\mathrm{p}} + \frac{\pi D_{\mathrm{syr1}}^2\rho}{8}(\gamma^2\dot{q}_{\mathrm{i}}^2 - \dot{q}_{\mathrm{i}}^2) + (\gamma f_{\mathrm{fric,syr2}} + f_{\mathrm{fric,syr1}}) + \Big(K_{\mathrm{lin}}\dot{q}_{\mathrm{i}} + K_{\mathrm{sin}}\dot{q}_{\mathrm{i}}^2\mathrm{sgn}(\dot{q}_{\mathrm{i}})\Big), \tag{4.8}$$

where $\gamma = \left(\frac{D_{\mathrm{syr1}}}{D_{\mathrm{syr2}}}\right)^2$. In Eq. (4.8), the second term represents the force generated by the difference of the velocity head in Bernoulli's principle, the third term represents the force generated by the friction in both syringes, and the fourth term represents the force generated by the loss in fluid energy. The force

transmission loss, f_{loss}, represents the sum of all these terms. At last, f_{in} can be simplified as

$$f_{\mathrm{in}} = \gamma f_{\mathrm{tip}}^{\mathrm{p}} + f_{\mathrm{loss}}. \tag{4.9}$$

The details of the motion equation in Eq. (4.8) are as follows:

$$f_{\mathrm{in}} = \begin{cases} \max\Big(0, f_{\mathrm{tip}}^{\mathrm{p}} + \Big(f_{\mathrm{s,syr1}} + f_{\mathrm{s,syr2}}\Big)\mathrm{sgn}(f_{\mathrm{in}})\Big) \\ \qquad\qquad\qquad\qquad\qquad\qquad \text{(if } \dot{q}_{\mathrm{in}} = 0\text{)} \\ f_{\mathrm{tip}}^{\mathrm{p}} + \big(f_{\mathrm{v,syr1}} + f_{\mathrm{v,syr2}}\big) \\ +\big(\sigma_{\mathrm{v,syr1}} + \sigma_{\mathrm{v,syr2}}\big)\dot{q}_{\mathrm{in}} + K_{\mathrm{lin}}\dot{q}_{\mathrm{in}} \\ +K_{\mathrm{sin}}\ \dot{q}_{\mathrm{in}}^2 \\ \qquad\qquad\qquad\qquad \text{(if } \dot{q}_{\mathrm{in}} > 0\text{, i.e. pushing motion)} \\ f_{\mathrm{tip}}^{\mathrm{p}} - \big(f_{\mathrm{v,syr1}} + f_{\mathrm{v,syr2}}\big) \\ +\big(\sigma_{\mathrm{v,syr1}} + \sigma_{\mathrm{v,syr2}}\big)\dot{q}_{\mathrm{in}} + K_{\mathrm{lin}}\dot{q}_{\mathrm{in}} \\ -K_{\mathrm{sin}}\ \dot{q}_{\mathrm{in}}^2 \\ \qquad\qquad\qquad\qquad \text{(if } \dot{q}_{\mathrm{i}} < 0\text{, i.e. pulling motion)} \end{cases} . \tag{4.10}$$

4.2.3 Cylindrical Forceps

Forward Kinematics

SCM is used on the developed forceps. Fig. 4-3 shows the outline of the SCM, where θ_{link} is the angle of the link, θ_{tip} is the angle of the tip, $f_{\mathrm{tip}}^{\mathrm{p}}$ is the force on the syringe side, $f_{\mathrm{tip}}^{\mathrm{g}}$ is the grasping force on the tip side, T_{cor} is the torque at the center of rotation, $\bigcirc_{\mathrm{TDC}}$ is the top dead center, and $\bigcirc_{\mathrm{BDC}}$ is the bottom dead center. The relationship between θ_{link} and θ_{tip} can be expressed as

$$\theta_{\mathrm{link}} = \theta_{\mathrm{TDC}} - \theta_{\mathrm{tip}}. \tag{4.11}$$

In this mechanism, q_{tip} can be expressed as

$$q_{\mathrm{tip}} = (r_1 \left(\sqrt{\frac{1}{\rho^2} - \sin^2\theta_{\mathrm{link}}} + \cos\theta_{\mathrm{link}}\right) - q_{\mathrm{TDC}}), \tag{4.12}$$

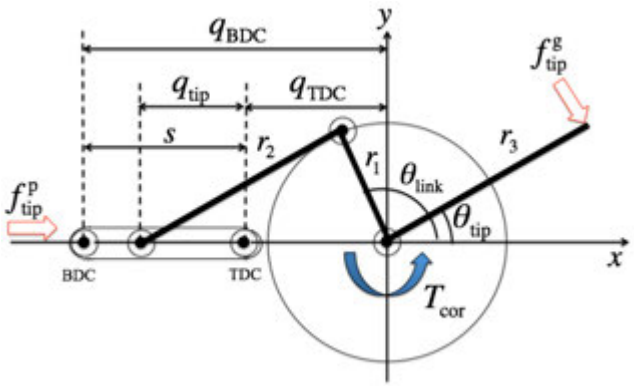

Fig. 4-3: Slider Crank Mechanism

where $\rho = \frac{r_1}{r_2}$. Additionally, the velocity of the linear motion, $\dot{q}_o$ can be expressed as

$$\begin{aligned} \dot{q}_{tip} = & \quad J_{aco}\dot{\theta}_{link} \\ = & \quad -r_1\left(\sin\theta_{link} + \frac{\sin\theta_{link}\cos\theta_{link}}{\sqrt{\frac{1}{\rho^2}-\sin^2\theta_{link}}}\right)\dot{\theta}_{link}. \end{aligned} \tag{4.13}$$

In addition, the relationship between the force on the syringe side, f^p_{tip} and the torque at the center of the link, T_o can be expressed as

$$T_{cor} = J_{aco} f^p_{tip}. \tag{4.14}$$

Further, the grasping force on the tip side can be derived as

$$f^g_{tip} = T_{cor} r_3. \tag{4.15}$$

Attention has to be paid in this research to the point of rotation singularity. When J_{aco} is equal to zero or infinity, the singular point, θ_{sp} can be obtained. If $J_{aco} = 0$, there are three singular points $\theta^0_{sp1} = 0, \theta^0_{sp1} = \pi, \theta^0_{sp3} = \pm\arcsin(\sqrt{\frac{r_2^2-1}{r_1^2-1}})$.In addition, if $J_{aco} = \infty$, there are two singular points $\theta^\infty_{sp1} = \pm\arcsin(\frac{1}{\rho})$.

Inverse Kinematics

The inverse dynamics of the SCM are described in this section. Using the cosine rule, the length, r_2 can be expressed as

$$r_2^2 = r_1^2 + (q_{tip} + q_{TDC})^2 - 2r_1(q_{tip} + q_{TDC})\cos\theta_{link}. \tag{4.16}$$

Table 4.1: Design Parameters of The Palpation Probe and The Forceps.

Parameters	Descriptions	Values	Units
Specifications of the Palpation Probe			
D_{syr1}	Diameter of Syringe 1	2.3	mm
D_{syr2}	Diameter of Syringe 2	2.1	mm
$\lambda_{\mathrm{syr1}}, \lambda_{\mathrm{syr2}}$	Length of Syringe	3.5	mm
$M_{\mathrm{syr1}}, M_{\mathrm{syr2}}$	Mass of Syringe	0.0837	kg
D_{tube}	Diameter of Tube	1.0	mm
d_{tube}	Length of Tube	2000	mm
Specifications of the Forceps			
D_{syr1}	Diameter of Syringe 1	2.3	mm
D_{syr2}	Diameter of Syringe 2	2.3	mm
l	Stroke	0.7	mm
r_1	Length of Link 1	0.75	mm
r_2	Length of Link 2	0.9	mm
r_3	Length of Link 3	5.75	mm
q_{BDC}	Bottom Dead Center of Slider	1.65	mm
θ_{BDC}	Bottom Dead Center of Rotation Angle	180.0	deg
q_{TDC}	Top Dead Center of Slider	0.9	mm
θ_{TDC}	Top Dead Center of Rotation Angle	114.6	deg

Then, the rotation angle θ_{link}can be expressed as

$$\theta_{\mathrm{link}} = \arccos\left(\frac{r_2^2 - (q_{\mathrm{tip}} + q_{\mathrm{TDC}})^2 - r_1^2}{2r_1(q_{\mathrm{tip}} + q_{\mathrm{TDC}})}\right). \tag{4.17}$$

Moreover, the angular velocity, $\dot{\theta}_{\mathrm{link}}$ can be expressed by using the inverse Jacobian as follows:

$$\begin{aligned} \dot{\theta}_{\mathrm{link}} = & \quad J_{\mathrm{aco}}^{-1}\dot{q}_{\mathrm{tip}} \\ = & \quad -\frac{\sqrt{\frac{1}{\rho^2} - \sin^2\theta_{\mathrm{link}}}}{r_1\left(\sin\theta_{\mathrm{link}}\sqrt{\frac{1}{\rho^2} - \sin^2\theta_{\mathrm{link}}} + \sin\theta_{\mathrm{link}}\cos\theta_{\mathrm{link}}\right)}, \end{aligned} \tag{4.18}$$

where J_{aco}^{-1} is the inverse Jacobian.

Table 4.2: Identified Parameters for the EHTS-based Palpation and Forceps

Descriptions	**Parameters**	**Values**		**Units**
		Palpation	Forceps	
Static Friction in Pushing/Grasping Motion	f_{s}^{+}	0.19	0.17	N
Static Friction in Pulling/Opening Motion	f_{s}^{-}	-0.24	-0.14	N
Viscous Coefficient in Pushing/Grasping Motion	σ^{+}	83.94	76.18	$(\mathrm{N}\cdot\mathrm{sec})/\mathrm{m}$
Viscous Coefficient in Pulling/Opening Motion	σ^{-}	33.20	84.14	$(\mathrm{N}\cdot\mathrm{sec})/\mathrm{m}$
Frictional Head Loss Term	K_{lin}	40.30		$\mathrm{kg}\cdot\mathrm{s}^{-1}$
Singular Head Loss Term	K_{sin}	0.0401		$\mathrm{kg}\cdot\mathrm{m}^{-1}$

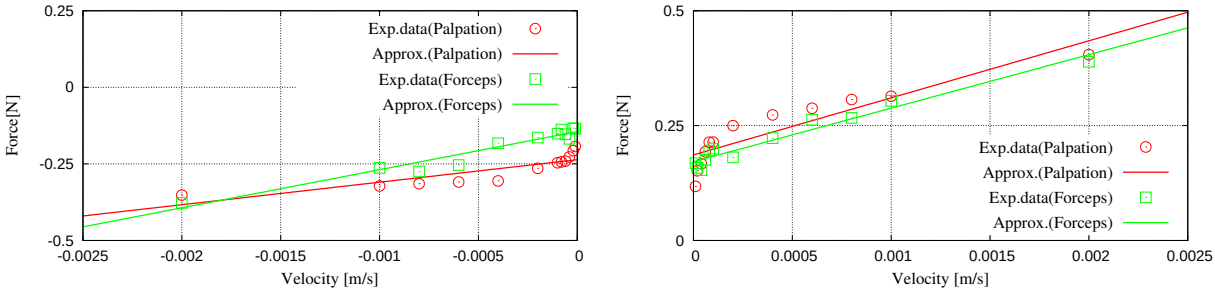

(a) Pulling/Opening Cycles

(b) Pushing/Grasping Cycles

Fig. 4-4: Identification Results of Transmission Loss

4.2.4 Design Parameters and Transmission Loss Model Identification

Mechanical parts of the EHTS and the forceps are designed as shown in Table 4.1. The transmission loss, which is defined in Eq. (4.9), is identified by the constant velocity test with 11 different velocity inputs. Transmission loss is measured by the full-order RFOB. Furthermore, the viscous coefficient, (σ), is identified by the least square method. Fig. 4-4 shows the experimental results, where the plots indicate the results of the actual transmission loss, and the line indicates the identified transmission loss model. In addition, the results of the identified parameters are shown in Table 4.2. Both results show that the identified model is well fitted to the actual transmission loss value for each constant velocity test. Hence, each experimental result of the developed model has satisfied the desired objectives.

4.3 Method

This section describes the control methodologies for the palpation device and the forceps, as well as the system configurations and procedures of the experiments. The control performance of both developed instruments is confirmed by the position control, force control, and bilateral control methods, respectively. The control design for each control method is described in 4.3.1. In addition, this research conducts a set of six experiments, the setup and procedure of which are described in 4.3.2.

4.3.1 Control Design

Position Control

The goal of position control in this research is to control the tip's position q_{tip}. However, the developed instruments does not mount on the position sensing device at the tip's side. Therefore, the desired tip's position is achieved by using following equation:

$$q_{\mathrm{tip}}^{\mathrm{des}} = \gamma q_{\mathrm{in}}^{\mathrm{cmd}}, \tag{4.19}$$

$$\dot{q}_{\mathrm{tip}}^{\mathrm{des}} = \gamma \dot{q}_{\mathrm{in}}^{\mathrm{cmd}}, \tag{4.20}$$

where $\bigcirc^{\mathrm{des}}$ is the desired value. A block diagram of the position control method for the EHTS is shown in Fig. 4-5. Where, "FO-DOB" means Full-order DOB described in chapter 2.

Angle Control of the Tip

The goal of angle control is to control the angle of the tip, θ_{tip}. However, the developed system does not rely on a rotary encoder to measure θ_{tip}. Thus, the coordinate transformation by the Jacobian as defined in Eq. (4.13) is required to transform the actuator position, q_{tip}, into the tip angle, θ_{tip}. The whole structure of the position control scheme is diagrammatically shown in Fig. 4-6, where $\tilde{\bigcirc}$ is a value on the tip side.

Force Control

The goal of force control in this research is to control the tip's side force. As mentioned in 4.2.2, in order to achieve the desired force on the endpoint side, the transmission loss force, (f_{loss}) needs to be compensated. In this research, f_{loss} is compensated by a feed-forward-based compensation using the

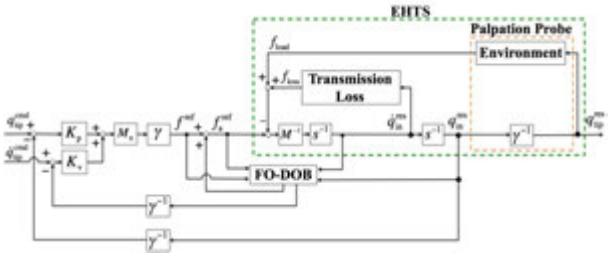

Fig. 4-5: Block Diagram of the Position Control Method for the EHTS-Based Palpation Probe

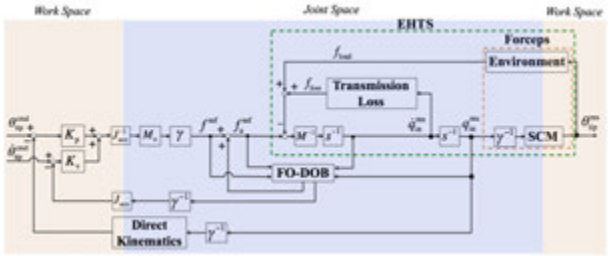

Fig. 4-6: Block Diagram of the Position Control Method for the EHTS-Based Forceps

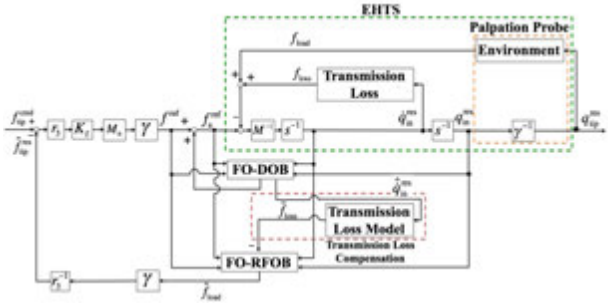

Fig. 4-7: Block Diagram of the Force Control Method for the EHTS-Based Palpation Probe

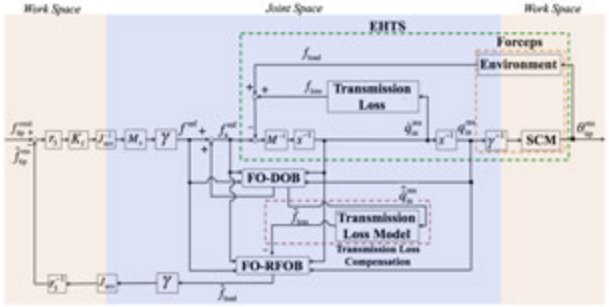

Fig. 4-8: Block Diagram of the Force Control Method for the EHTS-Based Forceps

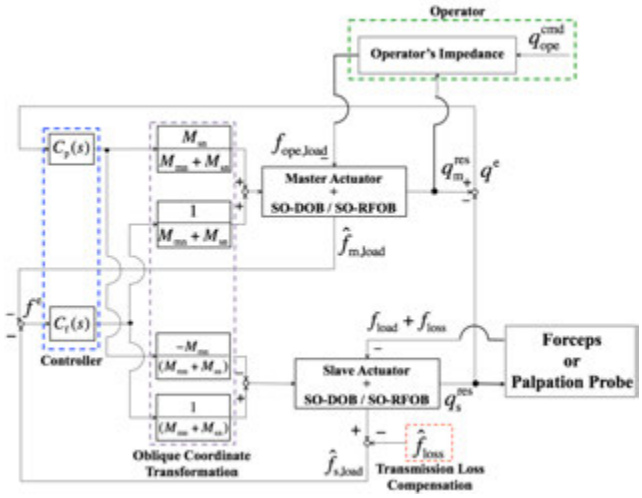

Fig. 4-9: Block Diagram of Bilateral Control for the EHTS-Based Palpation Probe and the Forceps

RFOB, according to Eq. (4.9), as follows:

$$\begin{aligned} f_{\mathrm{in}} &= \gamma \hat{f}_{\mathrm{tip}}^{\mathrm{p}} + (\hat{f}_{\mathrm{loss}} - \tilde{f}_{\mathrm{loss}}) \\ &\approx \hat{f}_{\mathrm{tip}}^{\mathrm{p}}, \end{aligned} \tag{4.21}$$

where $\tilde{f}_{\mathrm{loss}}$is an identified force transmission loss model, as mentioned in 4.2.4. A block diagram of the force control method for the EHTS is shown in Fig. 4-7.

Grasping Force Control

The goal of the force control technique in this research is to control the grasping force at the tip of the forceps, $f_{\mathrm{tip}}^{\mathrm{g}}$. The coordinate transformation by the Jacobian is utilized to achieve this task. In addition, the feed-forward-based friction compensation is applied to suppress the transmission loss of the EHTS. A block diagram of the grasping force control method is shown in Fig. 4-8. Where, "FO-RFOB" is the Full-order RFOB described in chapter 2.

Bilateral Control

In this research, an oblique coordinate bilateral control method, which is explained in Chapter 3, is applied. The whole structure of the 4-ch. bilateral control system is shown in Fig. 4-9.

Table 4.3: Control Parameters of Six Experiments.

Position and Force Transmission Performance	
Sampling Time (st)	$0.1\,\mathrm{msec}$
Cut off frequency of the DOB (g_{dob})	$300\,\mathrm{rad/s}$
Cut off frequency of the RFOB (g_{rfob})	$300\,\mathrm{rad/s}$
Actuator Nominal/Actual Mass (M_{n}, M)	$0.5\,\mathrm{kg}$
Nominal/Actual Torque Constant ($K_{\tau\mathrm{n}}, K_{\tau}$)	$33.0\,\mathrm{N/A}$
Position Proportional gain (K_{p})	$2500.0\,\mathrm{s}^{-2}$
Position Differential gain (K_{v})	$100.0\,\mathrm{s}^{-1}$
Tip's Position Control / Tip's Angle Control Experiment	
Tip's Force Control / Tip's Grasping Force Control Experiment	
Sampling Time (st)	$0.1\,\mathrm{msec}$
Cut off frequency of the Full-Order DOB (g_{dob})	$100\,\mathrm{rad/s}$
Cut off frequency of the Full-Orer RFOB (g_{rfob})	$100\,\mathrm{rad/s}$
Observer Gain (l_1)	383.1
Observer Gain (l_2)	78400.0
Actuator Nominal/Actual Mass (M_{n}, M)	$0.03\,\mathrm{kg}$
Nominal/Actual Torque Constant ($K_{\tau\mathrm{n}}, K_{\tau}$)	$0.57\,\mathrm{N/A}$
Position Proportional gain (K_{p})	$10000.0\,\mathrm{s}^{-2}$
Position Differential gain (K_{v})	$200.0\,\mathrm{s}^{-1}$
Force Differential gain (K_{f})	$2.0\,\mathrm{s}^{-2}$
Virtual Stiffness for Impedance Control (K_{env})	1500.0
Virtual Damping for Impedance Control (D_{env})	20.0

4.3.2 Experimental Setup

Position Control Experiment

A Voice Coil Motor (VCM, Technohands Co., Ltd. AVM 12-6.4) is connected to the developed palpation device. The displacement of the actuator side (q_{in}) is measured by the linear encoder (See Fig. 4-11(a)). Position tracking performance is tested under three different configurations: (i) 0° configuration

Bilateral Control Experiment	
Sampling Time (st)	$0.1\,\mathrm{msec}$
Cut off frequency of the Full-Order DOB (g_{dob})	$600\,\mathrm{rad/s}$
Cut off frequency of the Full-Order RFOB (g_{rfob})	$600\,\mathrm{rad/s}$
Observer Gain (l_1)	2473.9
Observer Gain (l_2)	$3240.0 * 10^3$
Master Side Nominal/Actual Mass ($M_{\mathrm{nm}}, M_{\mathrm{m}}$)	$0.5\,\mathrm{kg}$
Slave Side Nominal/Actual Mass ($M_{\mathrm{sn}}, M_{\mathrm{s}}$)	$0.03\,\mathrm{kg}$
Virtual Operator Side Nominal/Actual Mass ($M_{\mathrm{nvir}}, M_{\mathrm{vir}}$)	$0.5\,\mathrm{kg}$
Master Side Nominal/Actual Torque Constant ($K_{\tau\mathrm{mn}}, K_{\tau\mathrm{m}}$)	$33.0\,\mathrm{N/A}$
Slave Side Nominal/Actual Torque Constant ($K_{\tau\mathrm{sn}}, K_{\tau\mathrm{s}}$)	$0.57\,\mathrm{N/A}$
Virtual Operator Side Nominal/Actual Torque Constant ($K_{\tau\mathrm{virn}}, K_{\tau\mathrm{vir}}$)	$33.0\,\mathrm{N/A}$
Position Proportional gain (K_{p})	$10000.0\,\mathrm{s}^{-2}$
Position Differential gain (K_{v})	$200.0\,\mathrm{s}^{-1}$
Force Proportional gain (K_{f})	$2.0\,\mathrm{s}^{-2}$

(ii) 90° configuration (iii) 180° configuration. The 0° configuration represents a configuration in which the hydraulic cable is set straight; the 90° configuration represents a configuration in which the hydraulic cable is bent to 90° and the 180° configuration represents a configuration in which the hydraulic cable is bent to 180°. Furthermore, the position control of a step input is conducted using the following three different command scenarios:

$$q_{\mathrm{tip}}^{\mathrm{des}} = \begin{cases} 0.0005 & (\mathrm{case1}) \\ 0.001 & (\mathrm{case2}) \\ 0.0015 & (\mathrm{case3}) \end{cases}. \tag{4.22}$$

Similarly, the position control of a ramp input is conducted using the following three different commands:

$$q_{\mathrm{tip}}^{\mathrm{des}} = \begin{cases} 0.00025 \cdot t & (\mathrm{case1}) \\ 0.0005 \cdot t & (\mathrm{case2}) \\ 0.00075 \cdot t & (\mathrm{case3}) \end{cases}, \tag{4.23}$$

Table 4.4: Specification of the Thrust Wire.

Outer Tube (Stainless Tube)	
Outer Diameter	0.00211 m
Inner Diameter	0.00169 m
Spring Pitch	0.0021 m
Inner Tube (Nickel - Titan Wire)	
Diameter	0.0006 m
Whole Structure	
Outer Diameter	0.0028 m
Length	2.0 m

Fig. 4-10: The Endpoint Shape of the Thrust Wire

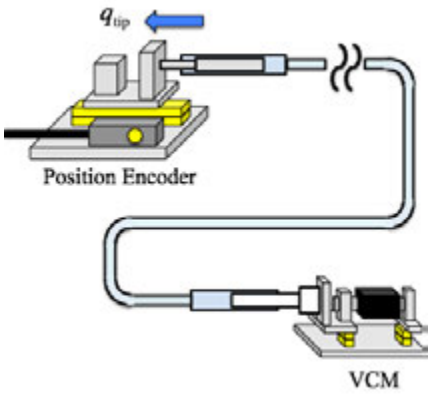

(a) Setup for the position transmission performance

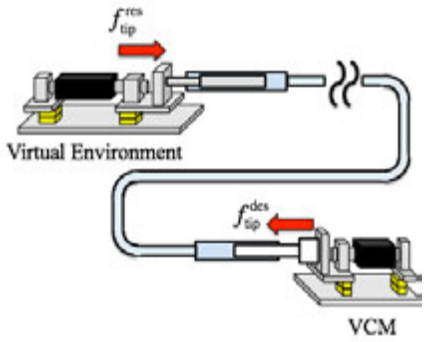

(b) Setup for the force transmission performance

Fig. 4-11: Experimental Setup for Transmission Performance Verification.

where t is the moving time. This experiment defines $0 < t \leq 2.0$. The endpoint side position, $q_{\mathrm{tip}}^{\mathrm{res}}$, is measured by an optical encoder (RENISHAW plc. RGH24).

Angle Control Experiment of the Tip

System configurations are the same as during the position tracking performance of the palpation device. In addition, the tracking performance is tested under the same configurations for the palpation device. In the case of the angle control experiment of the tip of the forceps, the angle control of a step

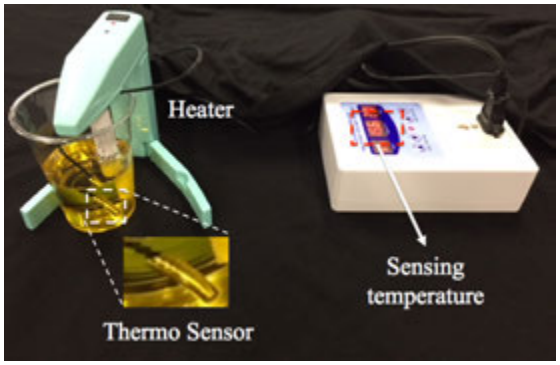

Fig. 4-12: Experimental Setup for The Temperature Dependency Test

input is conducted using the following two different command scenarios:
(In opening cycles)

$$\theta_{\mathrm{tip}}^{\mathrm{des}} = -30.0^{\circ}, \tag{4.24}$$

(In grasping cycles)

$$\theta_{\mathrm{tip}}^{\mathrm{des}} = -30.0^{\circ} + \theta_{\mathrm{tip}}^{\mathrm{init}}. \tag{4.25}$$

Similarly, the angle control of the ramp input is conducted using the following two different command scenarios:
(In opening cycles)

$$\theta_{\mathrm{tip}}^{\mathrm{des}} = -7.5^{\circ} \cdot t, \tag{4.26}$$

(In grasping cycles)

$$\theta_{\mathrm{tip}}^{\mathrm{des}} = -7.5^{\circ} \cdot t + \theta_{\mathrm{tip}}^{\mathrm{init}}, \tag{4.27}$$

where $\theta_{\mathrm{tip}}^{\mathrm{init}}$ is the initial tip's angle before the start of the grasping motion. In this experiment, $\theta_{\mathrm{tip}}^{\mathrm{init}}$ is set to 30°. The moving time is set to $0 < t \leq 4.0$. The actual tip angular is observed by a digital microscope camera (PlumRiver Inc. DJ-KNBKY-1000) and is measured using motion analysis software (Kinovea version 0.8.25). The outline of the experimental setup for the tip's angle control is described in Fig. 4-13(a).

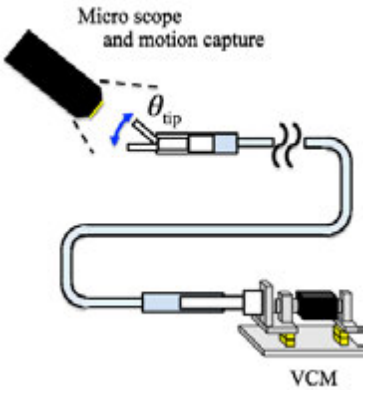

(a) Setup for the tip's angle control

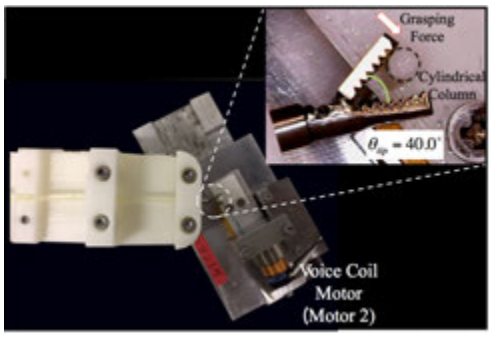

(b) Setup for the grasping force control

Fig. 4-13: Experimental Setup for the EHTS based Forceps.

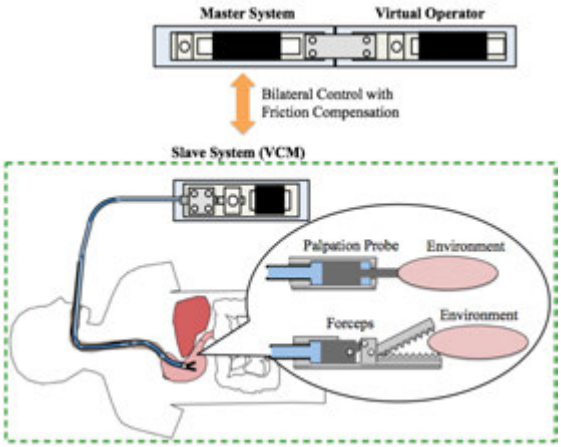

Fig. 4-14: Experimental Setup of the Bilateral Control Experiment

Force Control Experiment

The developed palpation probe is connected to the VCM and the force is applied to the palpation device. A linear actuator (Motor 2) is utilized to measure the reaction force at the endpoint and an impedance control is implemented in Motor 2. Therefore, the same experimental setup described in Fig. 4-11(b) were used. In this experiment, the virtual stiffness and virtual viscosity are set as shown in Table 4.3.1. The force control of a step input is conducted using the following three different command

scenarios:

$$f_{\mathrm{tip}}^{\mathrm{des}} = \begin{cases} 0.5 & (\mathrm{case1}) \\ 0.75 & (\mathrm{case2}) \\ 1.0 & (\mathrm{case3}) \end{cases}. \tag{4.28}$$

In addition, the force transmission performances under three different configurations ((i) 0°, (ii) 90°, (iii) 180°) are tested.

Grasping Force Experiment

The developed forceps is connected to the VCM. The grasping force is applied to the proposed system. Another VCM (Motor 2) is utilized to measure the grasping force. An impedance control is implemented in Motor 2. In this experiment, the virtual stiffness and virtual viscosity are set as shown in Table 4.3.1. . Further, the contacting point of the tip is set to $\theta_{\mathrm{tip}} = 40.0°$. When the grasping force feedback is implemented in the VCM, the reaction force is measured by the Full-Order RFOB applied to Motor 2. The scheme of the grasping force measurement system is shown in Fig. 4-13(b). The force control command is set as

$$f_{\mathrm{tip}}^{\mathrm{des}} = 0.2. \tag{4.29}$$

In addition, the force transmission performances under three different configurations ((i) 0°, (ii) 90°, (iii) 180°) are tested.

Transmission Performance Verification of the EHTS

- Comparison with Flexible Actuator

  The objective of this experiment is to verify the position and force transmission efficiencies of the EHTS using the developed system. Two electromagnetic linear motors are used (GMC HIL-STONE CO., LTD. S160Q) for this experiment. One linear actuator (Motor 1) is connected to the EHTS while the other (Motor 2) is mounted on the endpoint side as shown in Fig. 4-11(a). The position transmission performance is evaluated by the position control method using the step input ($q_{\mathrm{tip}}^{\mathrm{des}} = 0.002$m). The position command value and the position response value in a steady state response are compared. The endpoint position is measured by a linear encoder (Renishaw plc. RGH24) implemented in Motor 2. The force transmission performance is also evaluated by the

force control method using the step input ($f_{\rm tip}^{\rm des} = 0.5$N). The force command value and the force response value in a steady state response are compared. The endpoint force is measured by Motor 2, which is fixed to the same position using position control. The endpoint force is measured by the RFOB as shown in Fig. 4-11(b). In addition, the EHTS is compared with the flexible actuator. The specification of the thrust wire is shown in Table 4.3.1. Consequently, the size of the thrust wire is similar to that of the EHTS, and the transmission performances of both systems can be compared fairly. Both transmission performances are evaluated with transmission rates. The position transmission rate, (α), is defined as the ratio of the position command to the position response. Thus, $\alpha = q_{\rm tip}^{\rm res}/q_{\rm tip}^{\rm des}$. Further, the force transmission, (β), is defined as $\beta = \hat{f}_{\rm load}/f_{\rm tip}^{\rm des}$. These values are calculated for 12 different wire shape configurations.

- Frequency Analysis

  The frequency analysis of the EHTS was confirmed through the experiment. 13 different position / force sine wave commands ($q^{\rm cmd}$ and $f^{\rm cmd}$) were used and the position response ($q^{\rm res}$) and the force response ($\hat{f}_{\rm load}$) at the endpoint side were measured. The bode plots are plotted by using the measurement data and frequency characteristics are analyzed. The measurement method of position response and the force response are same to transmission performance comparison experiment. In this experiment, some hypothesis are set as follows: (i) The transmission loss was compensated by the Full-Order DOB. Therefore, the position / force control are ideally working. (ii) The nominal mass equals to the actual mass.

- Time-related Deterioration Test

  The dependency of the Time-related deterioration was confirmed through the experiment. Position and force transmission characteristics were confirmed by using the olive oil from one day to seven day after opening. Same experimental setups as shown in Fig. 4-11 is used for the position and force transmission performance confirmation.

- Temperature Dependency Test

  A temperature dependency test was confirmed through the experiment. Olive oil's temperature was controlled by using a thermo heater (compact ceramic heater : JTB TRADING Inc.) and a thermostat (Digital Thermostat AC 110-240V 10A:KKMoon,Inc.). The setups of the temperature control methodology is shown in Fig. 4-12. Operator observed the current temperature measured by the thermo sensor and operator turn off the thermo heater when the current temperature was reached

at the desired temperature. In this experiment, three different temperature $(20\mathrm{C}^{\circ}, 30\mathrm{C}^{\circ}, 40\mathrm{C}^{\circ})$. Same experimental setups as shown in Fig. 4-11 is used for the position and force transmission performance confirmation.

Bilateral Control Experiment

Fig. 4-14 shows the experimental setup for bilateral control. Two electromagnetic linear actuators and one VCM are used in the bilateral control experiment. One linear actuator is utilized as the master actuator. The VCM is connected to the proposed forceps (the slave actuator). Another linear actuator is connected to the master actuator. The sinusoidal position command is inputted to the master actuator (instead of a human). In this experiment, sinusoidal motion is inputted to the master actuator. The experimental work is done under three different conditions: (i) free motion; (ii) manipulation of a soft object (hemispherical Urethan gel); (iii) manipulation of a hard object (aluminum block). In addition, transmission loss compensation is implemented during grasping cycles and the compensation performance is compared by using the force response during both the grasping and opening cycles of the operation.

4.4 Results

The experimental results are described in this section. In 4.4.1, the position control performance of the EHTS-based palpation device is explained. In 4.4.2, the performance of the tip's angle control is described. In 4.4.3, the force control results of the EHTS-based palpation device are explained. In addition, the grasping force control results of the EHTS-based forceps are explained in 4.4.4. The position and force transmission performance results are explained in 4.4.5. Finally, the bilateral control results of both instruments are described in 4.4.6.

4.4.1 Position Control Experiments of EHTS-based Palpation

The step response results are shown in Fig. 4-15. Fig. 4-15(a) shows the step response at the actuator side under three different commands and Fig. 4-15(b) shows the error between the command and the response. From both results, the overshoot became large in proportion as large position command. However, the steady-state error converged to almost zero. Fig. 4-15(c) shows the step response at the endpoint side under three different commands and Fig. 4-15(d) shows the error between the ideal trajectory and the response. From Fig. 4-15(c) and (d) the overshoot is lower than the result in Fig. 4-15(a). The po-

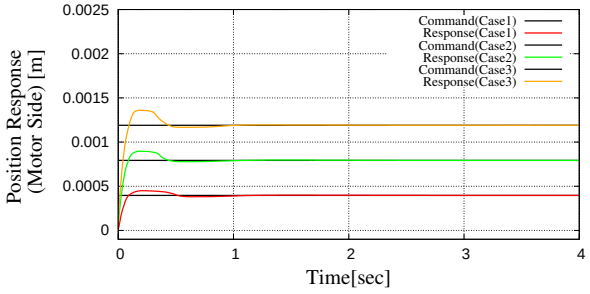

(a) Response of the Motor Side in Pushing Motion under Three Different Commands

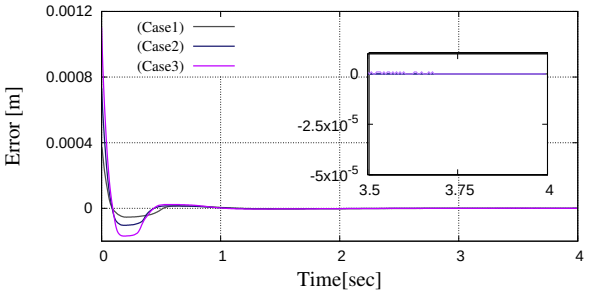

(b) Error between q^{cmd} and $q_{\mathrm{tip}}^{\mathrm{res}}$

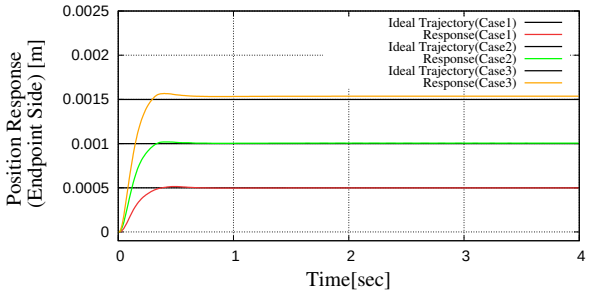

(c) Response of the Tip Side in Pushing Motion under Three Different Commands

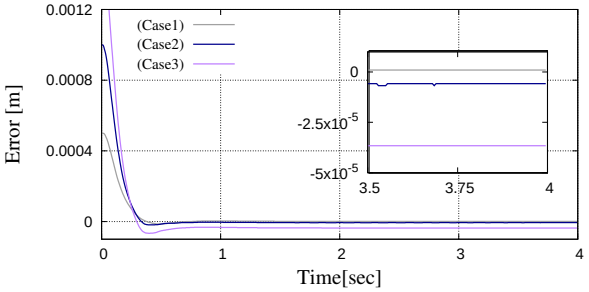

(d) Error between $\gamma^{-1}q^{\mathrm{cmd}}$ and q_{o}

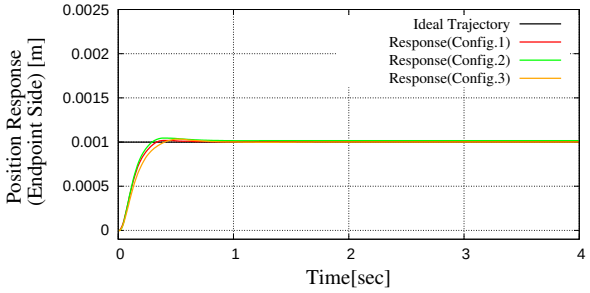

(e) Response of the Tip Side in Pushing Motion under Three Different Configurations

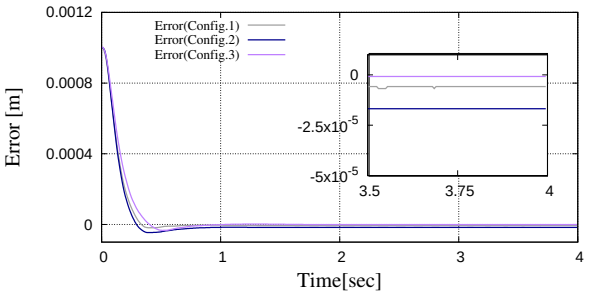

(f) Error between $\gamma^{-1}q^{\mathrm{cmd}}$ and q_{o}

Fig. 4-15: Step Response of Position Control with EHTS based Palpation Device

sition tracking performance under three different configurations are shown in Fig. 4-15(e). The tracking performance did not decline despite the increasing bending angle. The steady-state error in Fig. 4-15(e) is within $4.0\mathrm{x}10^{-5}$m.

Likewise, the position ramp response under three different commands is shown in Fig. 4-16. In the case of the ramp response, the error in transient response between the position command and the actuator-side response was lower than the step response error shown in Fig. 4-16(b). Fig. 4-16(c) shows the ramp

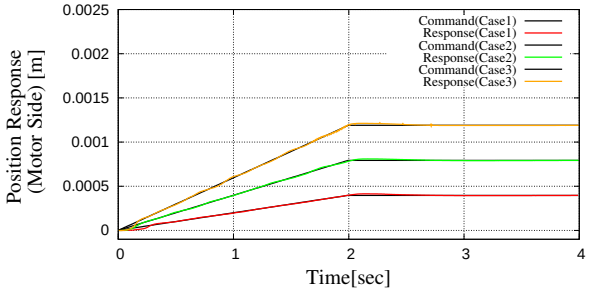

(a) Response of the Motor Side to Pushing Motion under Three Different Commands

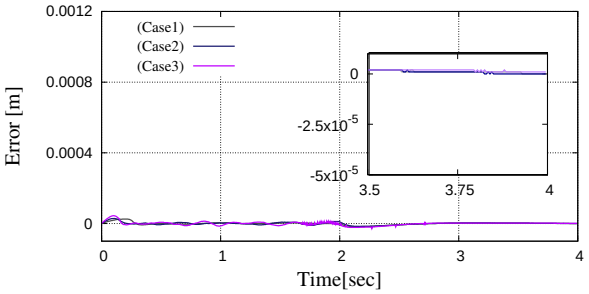

(b) Error between $\gamma^{-1}q^{\mathrm{cmd}}$ and $q_{\mathrm{tip}}^{\mathrm{res}}$

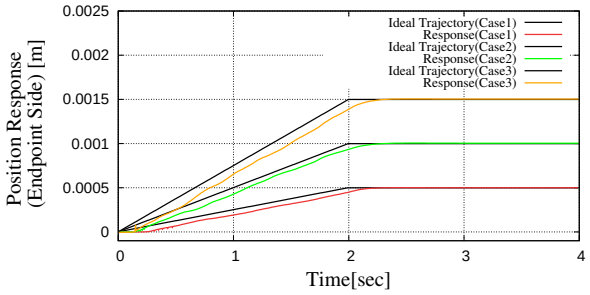

(c) Response of the Tip's Side to Pushing Motion under Three Different Commands

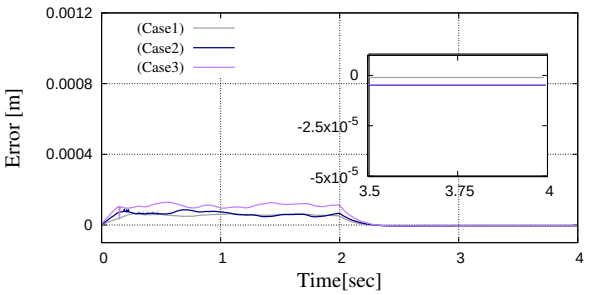

(d) Error between $\gamma^{-1}q^{\mathrm{cmd}}$ and $q_{\mathrm{tip}}^{\mathrm{res}}$

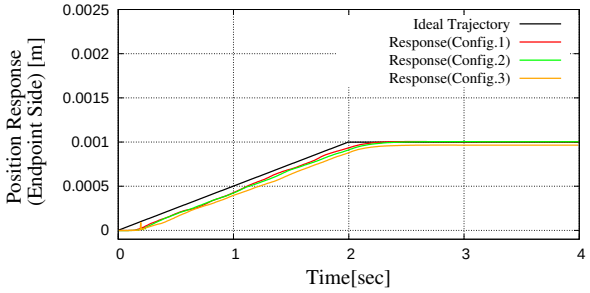

(e) Response of the Tip's Side to Pushing Motion under Three Different Configurations

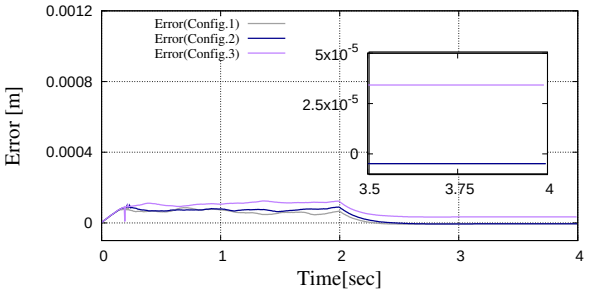

(f) Error between $\gamma^{-1}q^{\mathrm{cmd}}$ and $q_{\mathrm{tip}}^{\mathrm{res}}$

Fig. 4-16: Ramp Response of Position Control with EHTS based Palpation Device

response at the endpoint side and Fig. 4-16(d) shows the error between the ideal trajectory and endpoint-side response. The error during ramp motion was within $2.0\text{x}10^{-4}$m. Fig. 4-16(e) shows the ramp response at the endpoint side under three different configurations. The steady-state error converged to almost zero in all cases (maximum error was $4.0\text{x}10^{-5}$m). Therefore, the tracking performance did not depend on the wire's configuration compared with the results of Fig. 4-16(e).

4.4.2 Results of the Tip Angle Control Experiment

Fig. 4-17 shows the results of the tip's angle response to step input. Fig. 4-17(a) and Fig. 4-17(c) show the tip's angle response to step input in opening cycles at the actuator side/tip side. The steady-state error in Fig. 4-17(b) and Fig. 4-17(d) shows the tip's angle response to step input in opening/grasping cycles observed by the digital microscope. Furthermore, Fig. 4-17(e) and Fig. 4-17(f) show the tip's angle response to step input in opening/grasping cycles under three different configurations observed by the digital micro scope. Fig. 4-18 shows the results of the tip's angle response to ramp input in opening/grasping cycles. Fig. 4-18(a) and Fig. 4-18(c) show the tip's angle response to ramp input in opening/grasping cycles at Motor 1 ($\theta_{\mathrm{tip}}^{\mathrm{res}}$). Fig. 4-18(b) and Fig. 4-18(d) the tip's angle response to ramp input in opening/grasping cycles observed by the digital microscope. Furthermore, Fig. 4-18(e) and Fig. 4-18(f) show the tip's angle response to ramp input in opening/grasping operation under three different configurations observed by the digital microscope.

4.4.3 Force Control Experiments of EHTS based Palpation

Fig. 4-19 shows the experimental results of force control performance. Fig. 4-19 (a) shows the force transmission performance with and without transmission loss compensation and Fig. 4-19(b) shows the force response error. The steady-state error of force control without transmission loss compensation was 0.4 N, while the force transmission performance with transmission loss compensation was approximately 0.8 N. Therefore, the force transmission loss compensation was effective in improving force tracking performance. Fig. 4-19 (c) and Fig. 4-19(e) show the results of the actuator-side and endpoint-side force response, respectively, under three different commands with transmission loss compensation. The errors of each result are shown in Fig. 4-19(d) and Fig. 4-19(f), respectively. The experimental results indicate good force transmission performance and that the steady-state error of the force tracking performance of each force command was within 5.0^{-2} N. Furthermore, Fig. 4-19(g) shows the force control response under three different configurations and Fig. 4-19(h) shows the force response error. These results indicate that the force transmission performance did not deteriorate for any wire shape and the maximum steady-state error was 5.0^{-2} N.

4.4.4 Grasping Force Control Experiments of EHTS-based Forceps

Fig. 4-20 shows the experimental results of grasping force control performance. Fig. 4-20 (a) shows the grasping force transmission performance with and without transmission loss compensation. The steady-state error of the grasping force without transmission loss compensation was 0.16 N, while the grasping force transmission performance was 0.007 N. Therefore, the force transmission loss compensation was effective in improving the grasping force tracking performance. Fig. 4-20 (b) shows the experimental results of force control for three different postures with transmission loss compensation. The steady-state error of the grasping force tracking performance was within 2.4^{-2} N. In addition, the grasping force transmission performance did not depend on the shape of the tube.

4.4.5 Position/Force Transmission Performance of The EHTS-based Palpation

Comparison with Flexible Actuator

Fig. 4-21(a) shows the position transmission rate compared with the flexible actuator. The position transmission rate of the thrust wire is greater than that of developed device. However, the difference is very small and the transmission rate of the proposed device shows less dependence on the bending angle. Fig. 4-21(b) shows the force transmission rate compared with the flexible actuator. The force transmission of the flexible actuator decreases with increasing bending angle, whereas the transmission rate of the EHTS seems to be independent of the bending angle. However, EHTS did not reduce the force transmission performance despite increasing bending angle. The above results show that the developed device can solve the force attenuation problem without limiting the position transmission efficiency.

Frequency Analysis

Gain plots of the position transmission performance and the force transmission performance are shown in Fig. 4-22. Where, the blue line shows the -3dB. From Fig. 4-22, the cut-off frequency of the position and the force transmission was around 2.0Hz. According to some researches, the bandwidth of a surgeon during fine manipulation is below 2.0Hz [36,37]. Thus, the proposed device is satisfied to manipulate the fine motion under tele-operation. The bandwidth of transmission performance depends on the viscous effect of the fluid and the fluid leaking.

Time-related Deterioration Test

Fig. 4-23(a) and Fig. 4-23(c) show the position step and position ramp response for time-related deterioration test. From both results, there were no deterioration in all results. Correspondingly, the results of the force step response is shown in Fig. 4-23(e). This result also indicated that there were no dependency of the time-related deterioration.

Temperature Dependency Test

Results of the temperature dependency test for position step response and the position ramp response are shown in Fig. 4-24(a) and Fig. 4-24(c). Both results indicated that the position transmission performance did not depend on the oil temperature. Likewise, Fig. 4-24(e) shows the force step response of different oil temperature. This results also indicated that the oil temperature did not depend on the force transmission performance.

4.4.6 Results of the Bilateral Control Experiments

Results of the EHTS-based Palpation

The command of the sinusoidal wave motion is determined by the results of the cut-off frequency of the position control and force control. The sine wave input was set to 1.4 Hz. Fig. 4-25 shows the bilateral control results of the EHTS-based palpation probe. Where, the yellow area describes the contact motion. Fig. 4-25 (a) and Fig. 4-25(b) show the position and force responses in bilateral control without contacting an object (i.e., free motion). Also, Fig. 4-25 (c) and Fig. 4-25 (d) show the position and force time responses in bilateral control when the virtual operator uses the master system to interact with soft environments. In addition, Fig. 4-25 (c) and Fig. 4-25 (d) show the position and force time responses in bilateral control when the virtual operator uses the master system to interact with hard environments. The experimental results shown in Fig. 4-25 demonstrate that operating force losses can be reduced using transmission loss compensation. Therefore, an operator can feel the environmental force more clearly, which is a good contribution for NOTES surgery. In addition, according to the experimental results of contacting motion shown in Fig. 4-25(d) and Fig. 4-25(f), the reaction force was varied with each environment. The behavior shown in Fig. 4-25 can be also felt by the human operator. Even if the human operator operates the proposed forceps, the operator can feel the reaction force clearly without facing the large operating force.

Results of the EHTS-based Forceps

The command of the sinusoidal wave motion is determined by the result of the cut-off frequency of the tip's angler control and the grasping force control. The sine wave input was set to 0.71 Hz. Fig. 4-26 shows the bilateral control results of the EHTS-based forceps. Where, the yellow area describes the contact motion. Fig. 4-26 (a) and Fig. 4-26 (b) show the position and force time responses in bilateral control without contacting an object through bilateral control and proposed forceps. Fig. 4-26 (c) and Fig. 4-26 (d) show the position and force time responses in bilateral control when the virtual operator uses the master system to interact with soft environments. Fig. 4-26 (c) and Fig. 4-26 (d) show the position and force time responses in bilateral control when the virtual operator uses the master system to interact with hard environments. The experimental results shown in Fig. 4-26 demonstrate that operating force losses can be reduced using transmission loss compensation. Therefore, an operator can feel the environmental force more clearly, which is a good contribution for NOTES surgery. In addition, from the experimental results of the contacting motion shown in Fig. 4-26(d) and Fig. 4-26(f), the reaction force varied with each environment. The behavior shown in Fig. 4-26 can also be felt by the human operator. Even if the human operator operates the proposed forceps, the operator can feel the reaction force clearly without facing the large operating force.

4.5 Discussions

In this study, two types of haptic medical instruments for safe NOTES surgery are developed. The originality of the proposed mechanism is that the force and position information are transmitted by the fluid energy. The advantage of this mechanism is force transmission performance is guaranteed in any wire's configurations. In general, the doctor cannot measure the configurations of the wire during NOTES operation because the instruments are inserted into the patient's body. Therefore, this unique structure is effective to realize haptic NOTES surgery. The transmission loss of the developed instruments is indicated by the physical model, while the position and force transmission performance of both medical instruments were confirmed through the experiments. The position and force transmission performance compared with release-type instruments (i.e., a flexible actuator) were confirmed. Moreover, oblique coordinate control-based 4-ch. bilateral control was applied to both instruments and the validity of the haptic sensation was confirmed under three different conditions.

The size of syringes, which is used for palpation probe, are different diameter ($D_{\mathrm{Syr1}} = 0.0023\mathrm{mm}$,

$D_{\mathrm{Syr2}} = 0.0021\mathrm{mm}$). By using different size syringes, the physical scaling and velocity head influence described in 4.2.2 is occurred. Thus, the position and force response generated at the endpoint side differed from the response generated at the motor side (See Fig. 4-13, Fig. 4-14 and Fig. 4-17). Therefore, this system is quite severe to the diameter of the syringe but the operator can obtain the desired value by taking into account the influence of the γ. In addition, the stroke of the palpation probe is approximately $5.0\mathrm{mm}$ and is sufficient to push the environment. The diameter of the outer tube is $2.6\mathrm{mm}$. This size is enough small to insert an endoscope camera. The abnormal tissue detection performance depends on the depth of the abnormal tissue. In case of this probe, If the depth of the pushing target, such as cancer tissue, is over 5 mm, it is difficult to measure the reaction force of the abnormal tissue. This constraint depends on the length of the probe.

The SCM mechanism was applied to the EHTS-based forceps. The tip's angle and grasping force are derived using the Jacobian described in Eq. (4.13) and the lengths of the links (r_1, r_2, r_3) are essential parameters to define the Jacobian. Therefore, the large grasping force was obtained by setting a large value for the Jacobian. However, there is a limitation to setting the Jacobian owing to the singularity points. In this research, the length of links 1 and 2 was designed in order to obtain the Jacobian as large as possible.

The experimental results of the position control and the tip's angle control show that there were errors between the command value and response value at the motor side caused by the overshoot. The magnitude of the overshoot increased when the position commands increased. This phenomenon was also observed in the results of the step response of the EHTS-based forceps. This overshoot is due to the limitation of the disturbance suppression performance by the Full-Order DOB. The disturbance suppression performance can be further improved by setting a large cut-off frequency value (g_{dob}). However, this overshoot did not influence the response at the endpoint side because of the law bandwidth of the proposed forceps.

Let us consider the force control experiments of both instruments. The force control performance was improved by applying transmission loss compensation. However, the steady-state error remained for each experimental result. The cause of this steady-state error was the modeling error of the transmission loss model. As mentioned in 4.2.4, the transmission loss model was identified using the steady-state value of the actual transmission loss. Hence, the transient response of the transmission loss was not taken into account. In addition, the feedforward-type compensation was applied to the system. Therefore, the error was not modified. In order to improve compensation performance, online parameter modification

methodologies, such as an adoptive control method, could be effective. Further, the compensation model is not continuous function as mentioned in Eq. (4.8). Thus, the compensation performance would be worse in low velocity area due to the noise of the estimated velocity by a state observer. As mentioned in Section 2, the influence of the estimated velocity noise of full-order RFOB can suppress compared with the minimal-order RFOB but the noise effect cannot suppress completely. However, the reaction force of free motion and the contact motion in bilateral control experiment indicated that the compensation error is small enough to feel the environment reaction force. From this reason, the force transmission with feed-forward compensation can achieve the clear environmental force transmission.

In addition, the comparison results of the force transmission performance indicated the force transmission performance of the developed device was guaranteed for any wire's configurations. In case of the flexible actuator, the force transmission performance depended on the wire's shape owing to the nonlinear friction. Therefore, the proposed instruments can utilize such a penetrate area where the operator cannot measure the configurations of the wire. Further, the proposed instruments does not depend on the oil temperature. In general, human's body temperature is around 37C$^\circ$ and the proposed instruments were guaranteed the transmission performance. Moreover, there was no time-related deterioration within 7days after opening. Considering about frequency characteristics, the cut-off frequency of the developed instruments was around 2.0Hz. Consequently, the developed device was difficult to transmit the impulsive force such as a knocking motion and proposed instruments have a limitation to the medical applications. Wagner *et al.* analyzed the role of force feedback in tele-operation robot and they described that the surgeon's movements during fine manipulation within surgical procedures are 1.0 - 2.0 Hz. However, this research is only focused on the blunt dissection[37].

However, the proposed system has a limitation. There were the origin drifts of position transmission performance by the EHTS. It would be caused either due to oil leakage or due to the compressibility of the oil. These influences caused the transmission performance to deteriorate, and the charge pressure has to be kept constant in order to maintain the transmission performance. In this study, the operator regularly injects olive oil into the syringes and tube using a small injector. However, this research does not manage the drifts quantitatively. As a solution for maintaining the charge pressure at a constant value, the rotary pumps [38] or the mechanical sealing such as an O rings are effective solutions. However, the large force input has a risk to make bio-tissue damage. According to my previous research, palpation over 1.5N force seemed bleeding [39]. Therefore, the proposed device is suitable for using a medical application for palpation or grasping bio-tissue.

4.6 Summary

This chapter presents a newly developed two types EHTS-based medical instruments in order to improve the haptic feedback of NOTES surgical system. The proposed forceps is physically small enough to be attached to the endoscope. In addition, the research results have shown that the position and force transmission performance are guaranteed for any wire's shape. Each transmission performance was experimentally tested and verified. In addition, a bilateral control using transmission loss compensation was implemented to the proposed EHTS-based forceps. The obtained results have demonstrated that an operator will be able to correctly get the force feedback and tactile sensation in manipulating a patient's internal organs.

Through the experimental results, proposed instruments had a limitation for output force due to the oil leakage. This problem would be solved by using a mechanical sealing method such as a O-ring and it requires to take into account as a future work.

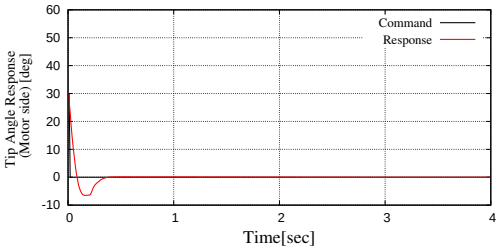

(a) Response of the motor side in closing cycle

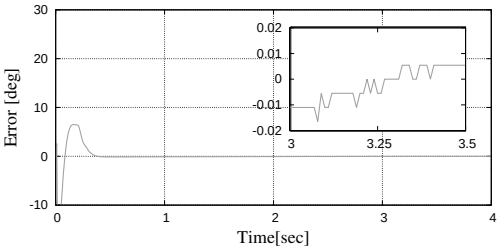

(b) Error of the motor side in closing cycle

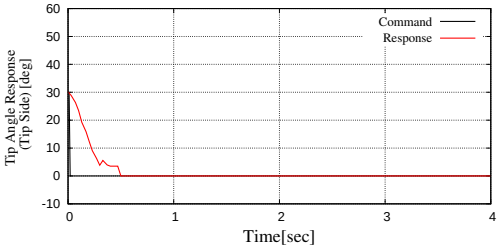

(c) Response of the tip side in closing cycle

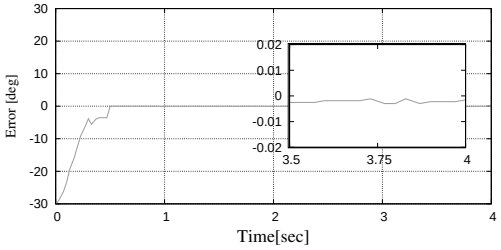

(d) Error of the tip side in closing cycle

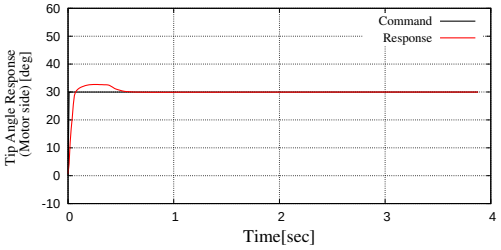

(e) Response of the motor side in opening cycle

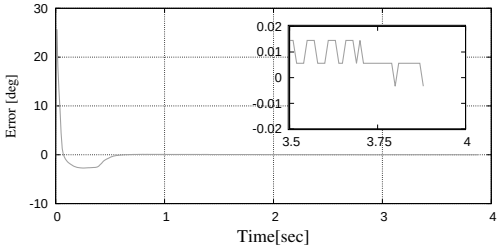

(f) Error of the motor side in opening cycle

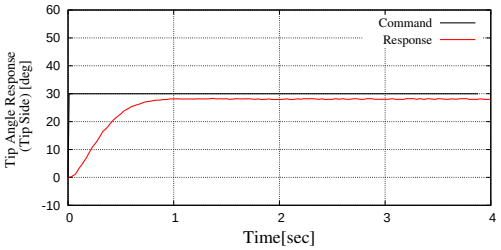

(g) Response of the tip side in opening cycle

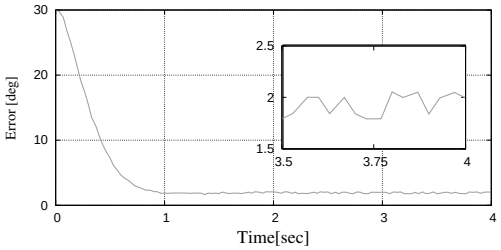

(h) Error of the tip side in opening cycle

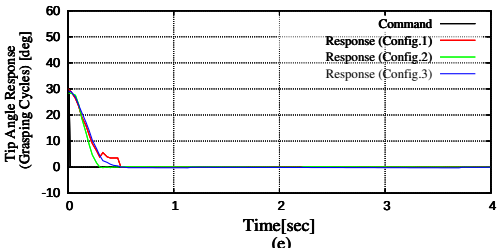

(i) Response to step input of the different configurations in closing cycles

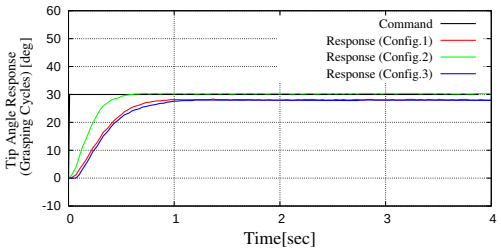

(j) Response to step input of the different configurations in opening cycles

Fig. 4-17: Step Response of Position Control with EHTS based Forceps

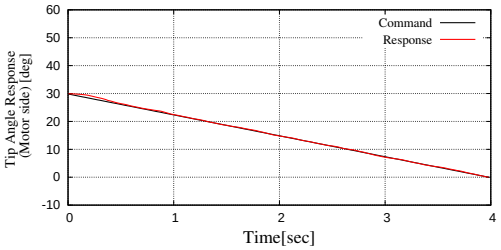

(a) Response of the motor side in closing cycle

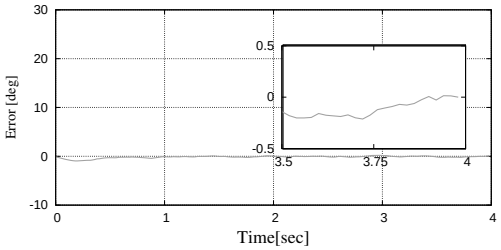

(b) Error of the motor side in closing cycle

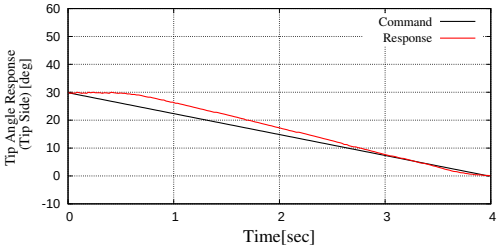

(c) Response of the tip side in closing cycle

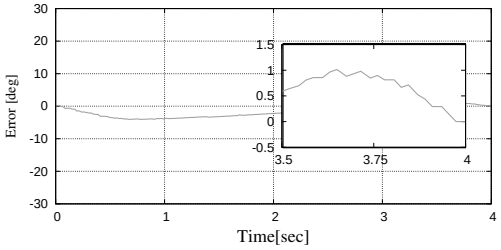

(d) Error of the tip side in closing cycle

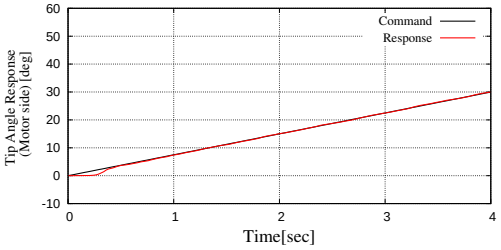

(e) Response of the motor side in opening cycle

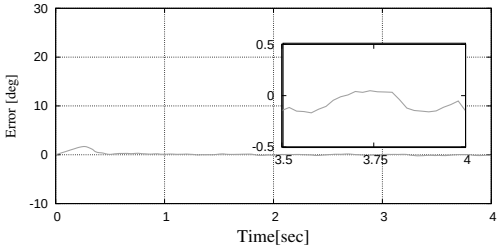

(f) Error of the motor side in opening cycle

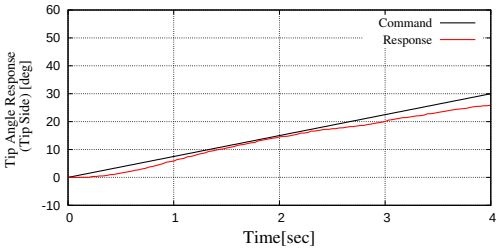

(g) Response of the tip side in opening cycle

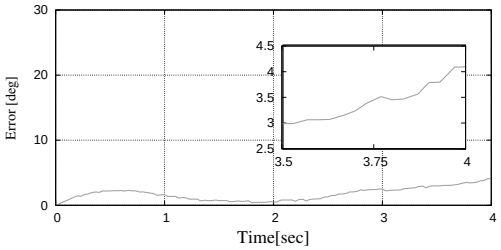

(h) Error of the tip side in opening cycle

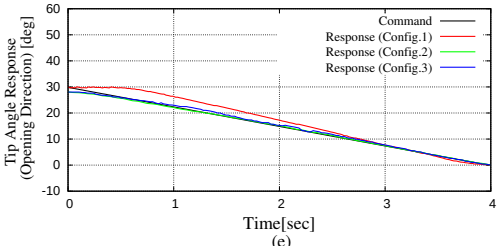

(i) Response to ramp input of the different configurations in closing cycles

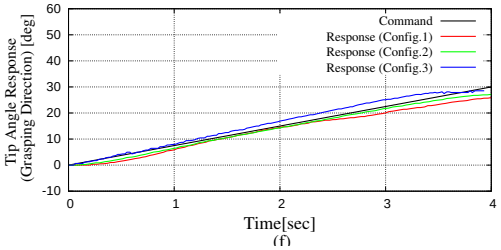

(j) Response to ramp input of the different configurations in opening cycles

Fig. 4-18: Ramp Response of Position Control with EHTS based Forceps

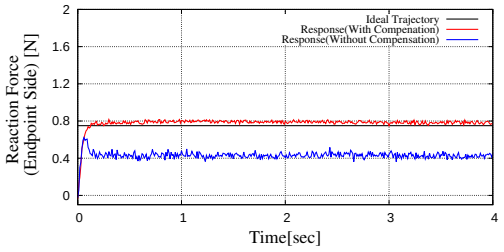

(a) Comparison of the Force Step Results for EHTS-Based Palpation Probe (with and without compensation)

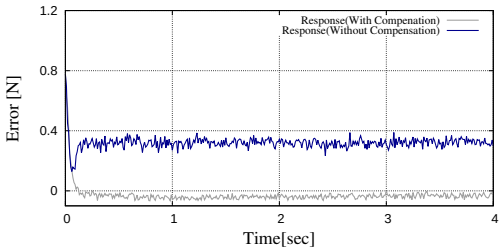

(b) Error of the Force Step Results for EHTS-Based Palpation Probe

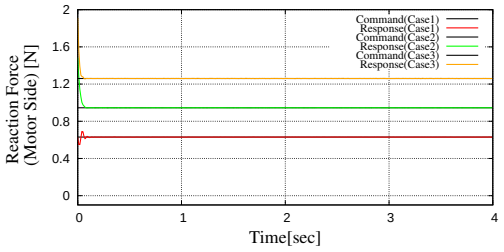

(c) Response of the Motor Side in Pushing Motion under Three Different Commands

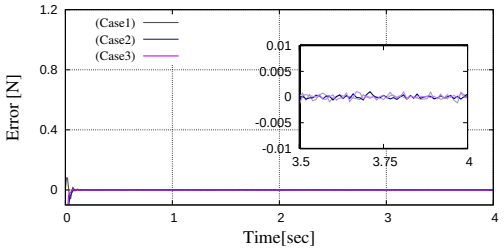

(d) Error of the Motor Side in Pushing Motion under Three Different Commands

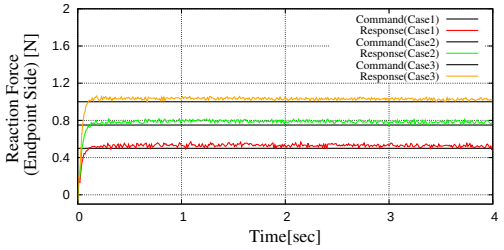

(e) Response of the Tip's Side in Pushing Motion under Three Different Commands

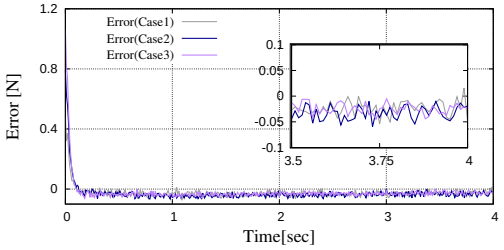

(f) Error of the Tip's Side in Pushing Motion under Three Different Commands

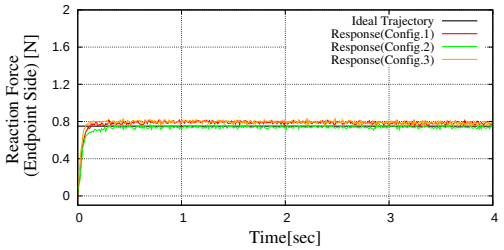

(g) Response of the Tip's Side in Pushing Motion under Three Different Configurations

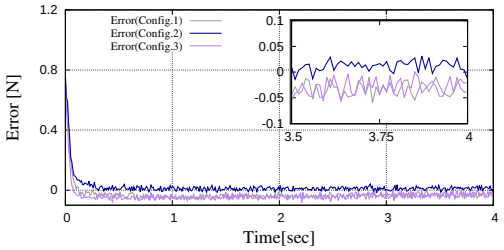

(h) Error of the Tip's Side in Pushing Motion under Three Different Configurations

Fig. 4-19: Step Response of Position Control with EHTS-Based Palpation Probe

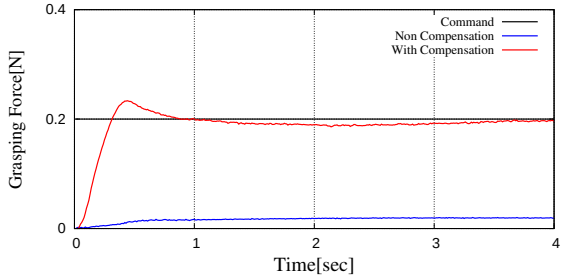

(a) Comparison of the force step results (with and without Compensation)

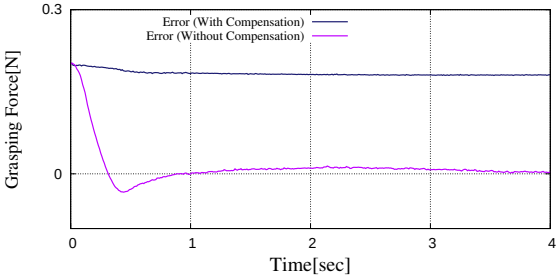

(b) Error of the Comparison Results (with and without Compensation)

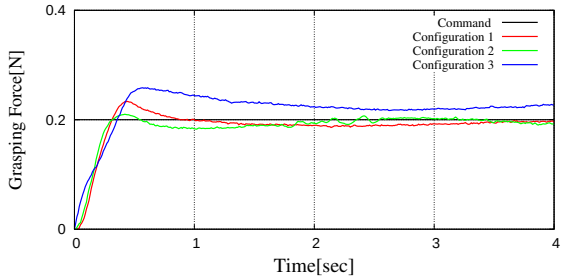

(c) Response of the Tip's Side in Closing Cycle under Three Different Configurations

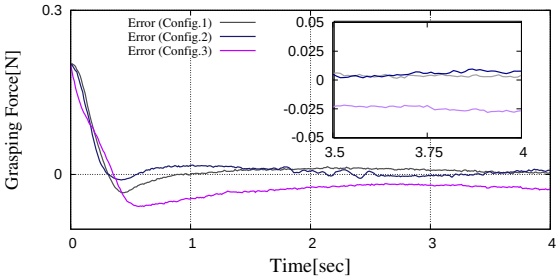

(d) Error of the Tip's Side in Closing Cycle under Three Different Configurations

Fig. 4-20: Experimental Results of the Grasping Force Control

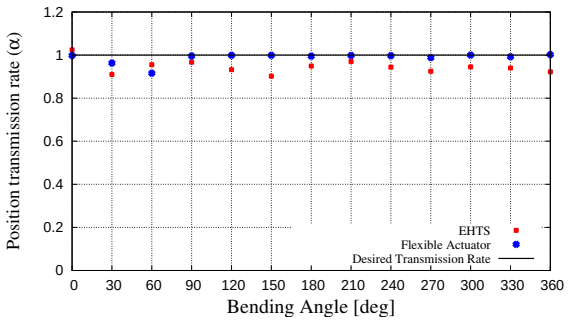

(a) Position Transmission Performance

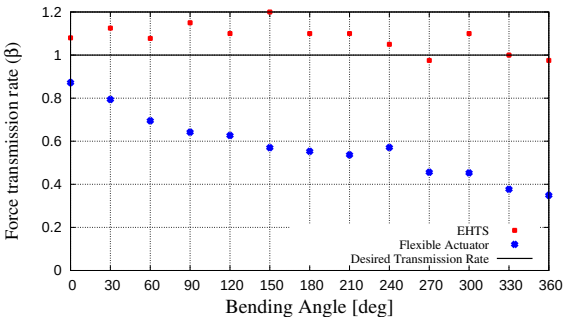

(b) Force Transmission Performance

Fig. 4-21: Position/Force Transmission Performance Comparison With Flexible Actuator under 13 different Configurations.

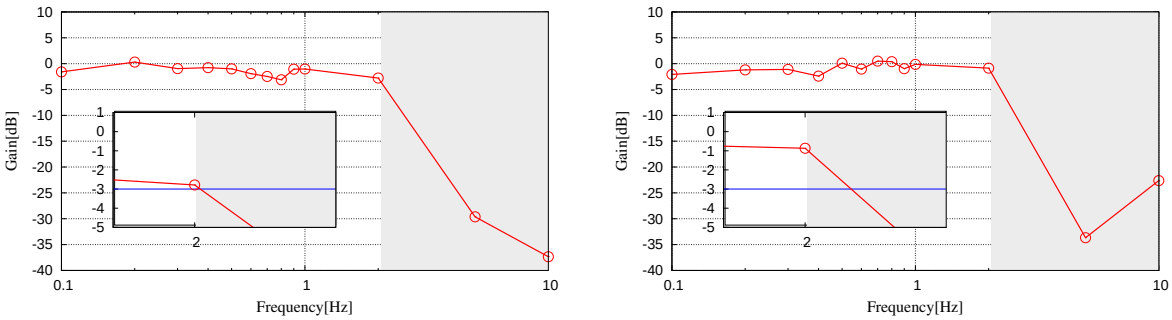

(a) Position Transmission Characteristics

(b) Force Transmission Characteristics

Fig. 4-22: Gain Plots of the Position and the Force Transmission Characteristics.

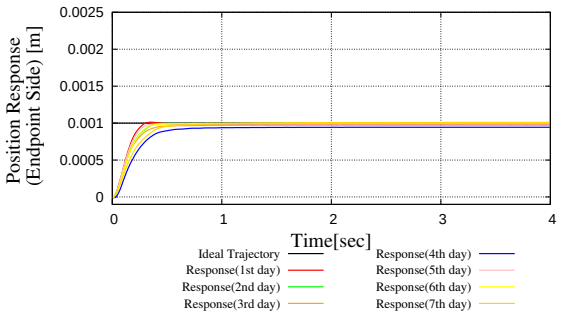

(a) Position Step Response

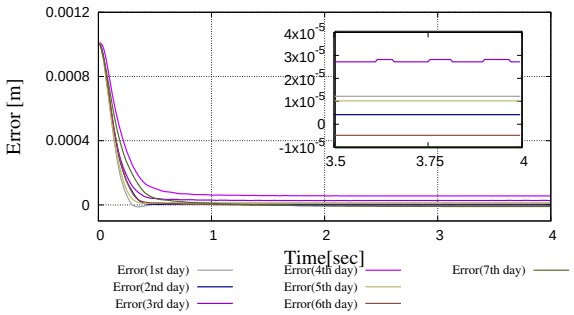

(b) Error of Position Step Response

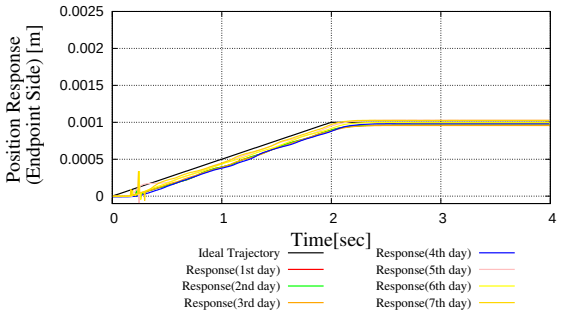

(c) Position Ramp Response

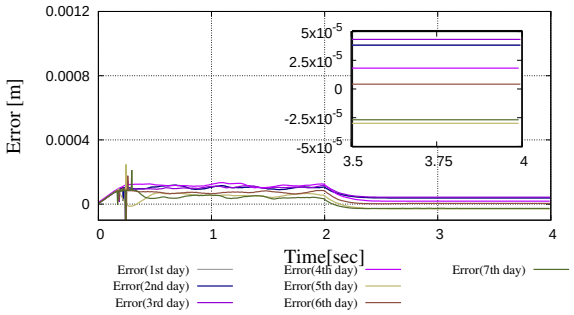

(d) Error of Position Ramp Response

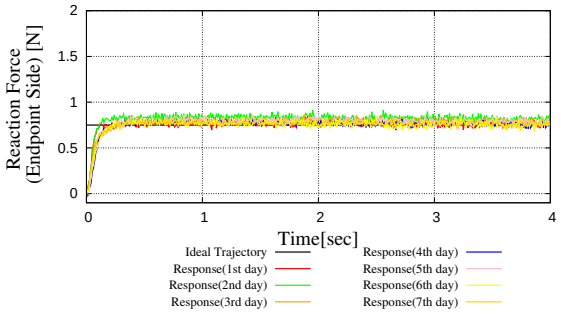

(e) Force Step Response

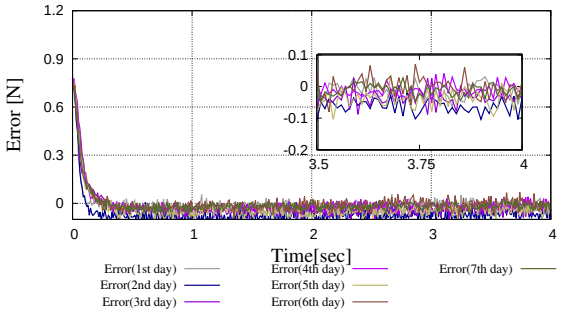

(f) Error of Force Step Response

Fig. 4-23: Results of the Day Variation Experiments.

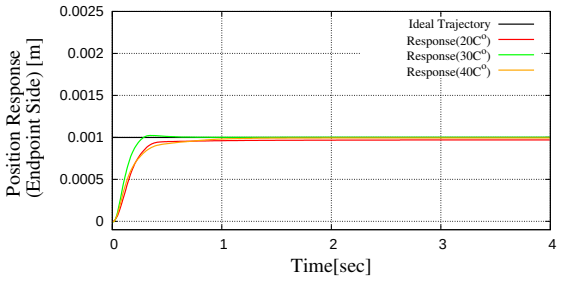

(a) Position Step Response

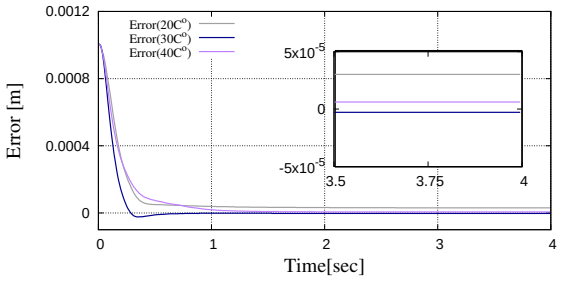

(b) Error of Position Step Response

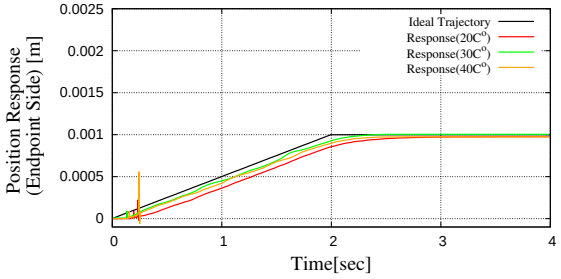

(c) Position Ramp Response

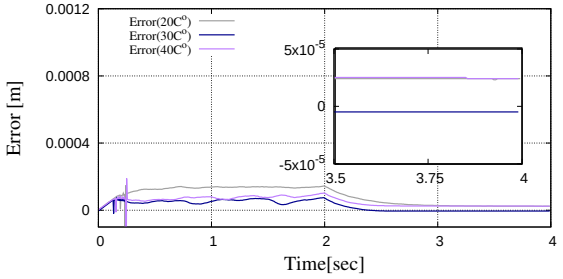

(d) Error of Position Ramp Response

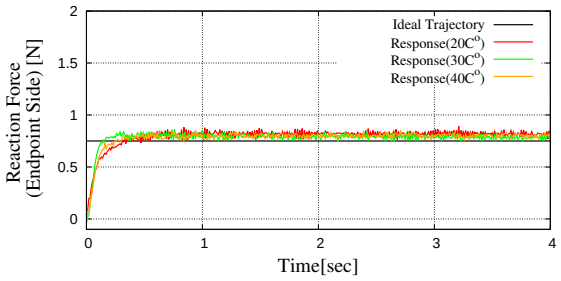

(e) Force Step Response

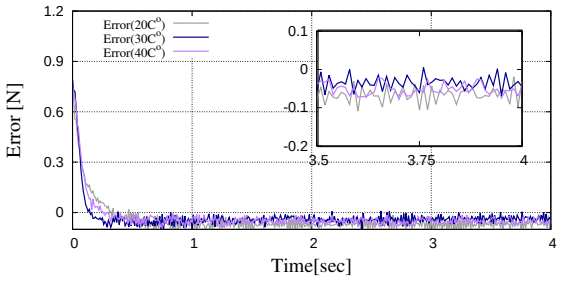

(f) Error of Force Step Response

Fig. 4-24: Results of the Temperature Dependency Test

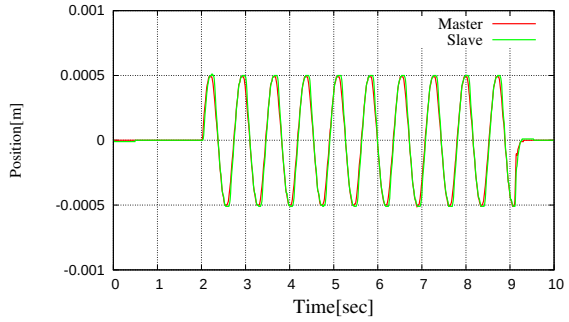

(a) Position Response in Free Motion

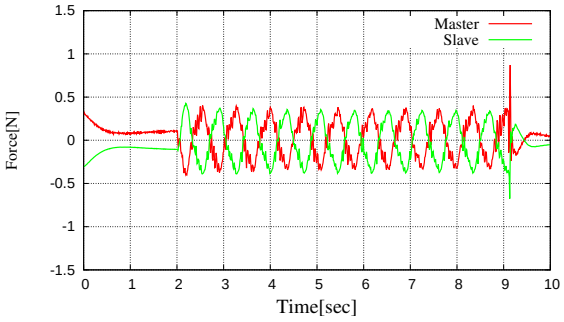

(b) Force Response in Free Motion

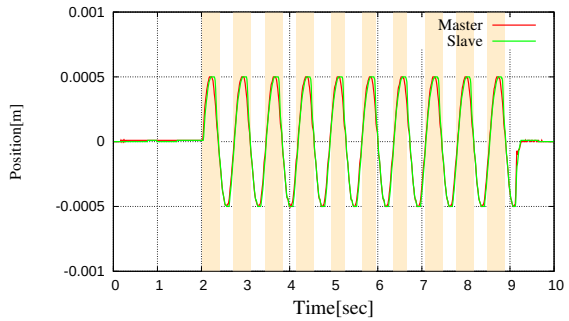

(c) Position Response in Contact Motion with A Hemispherical Urethane Gel

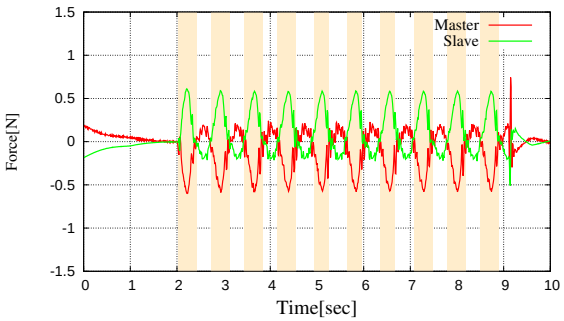

(d) Force Response in Contact Motion with A Hemispherical Urethane Gel

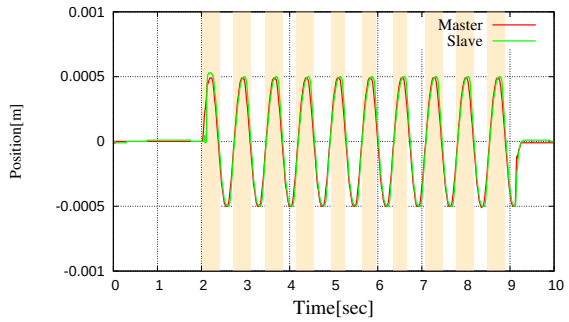

(e) Position Response in Contact Motion with An Aluminum Block

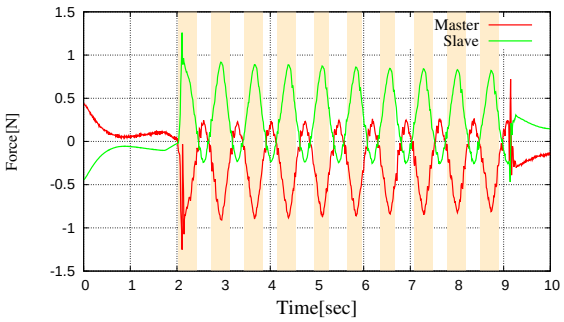

(f) Force Response in Contact Motion with An Aluminum Block

Fig. 4-25: Bilateral Control Results of EHTS based Palpation Probe.

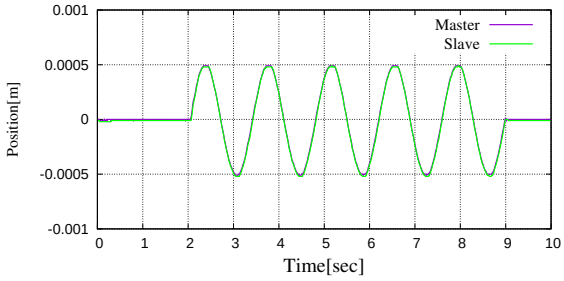

(a) Position Response in Free Motion

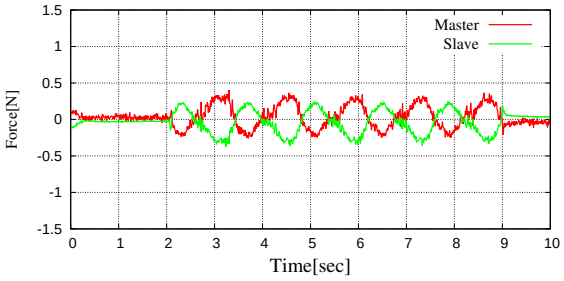

(b) Force Response in Free Motion

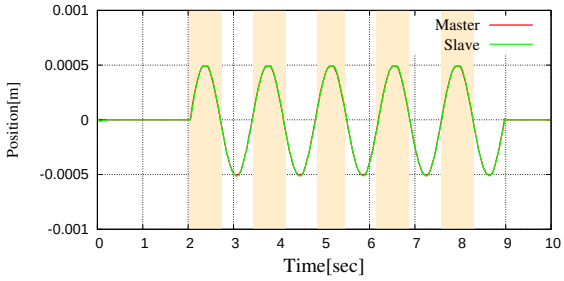

(c) Position Response in Contact Motion with A Hemispherical Urethane Gel

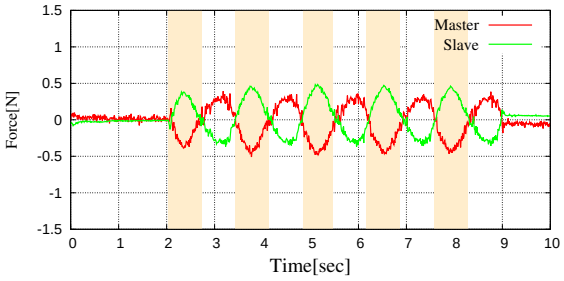

(d) Force Response in Contact Motion with A Hemispherical Urethane Gel

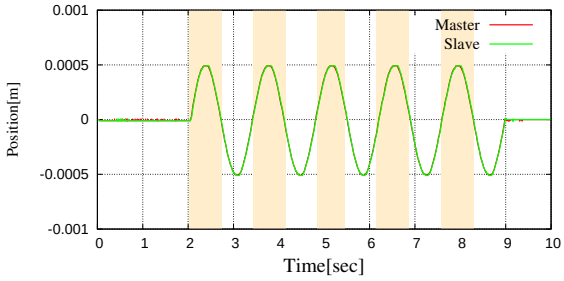

(e) Position Response in Contact Motion with An Aluminum Block

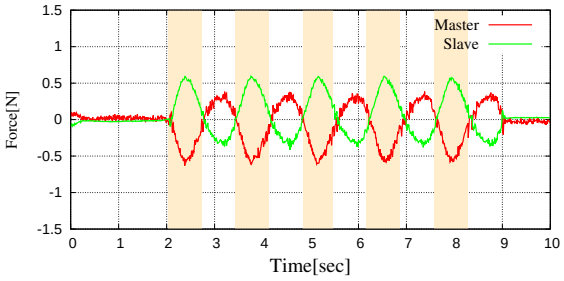

(f) Force Response in Contact Motion with An Aluminum Block

Fig. 4-26: Bilateral Control Results of EHTS based Forceps.

Chapter 5

A Quantitative Evaluation Method for Evaluating Non-Obstructive Azoospermia

5.1 Introduction

Recently, the number of patients struggling with infertility has increased worldwide due to the trend of late marriage and the aging population [40]. In fact, approximately 15% of couples are unable to conceive after one year of unprotected intercourse. The cause of infertility involves men as well as women. The rate of male infertility is about 20% in all infertility patients. Furthermore, the rate of infertility caused by both the male and the female is about 38% [41]. Therefore, male infertility is a crucial problem. Although some treatment methodologies for male infertility have been established [42], most of the established treatment methods and discussions by medical doctors on solutions to infertility currently concern female infertility [43, 44].

“ Azoospermia, ”one of the famous diseases related to male infertility[45–47], is defined as a complete absence of sperm in the ejaculate. The rate of azoospermia is approximately 1% in all men [48] and 10% to 15% in infertile men[49]. There are two types of azoospermia: obstructive azoospermia (OA) and non-obstructive azoospermia (NOA). In the case of OA, a sperm cannot pass through the spermatic duct due to a vasectomy or alternate etiologies[47, 50]. The rate of OA in male infertility patients is approximately 6.1% [51] to 13.6 % [52] . In the case of NOA, there is no sperm in the ejaculate due to the impaired production of sperm[14]. The rate of NOA in azoospermia patients is 60%[15]. Currently, many NOA treatment methods have been suggested; in particular, Intracytoplasmic Sperm Injection (ICSI) is a standard method. There are five well-known methods for ICSI: Fine Needle Aspiration

(FNA), Percutaneous Testis Biopsy (PTB), Open Testicular Biopsy (OTB), Testicular Sperm Extraction (TESE), and Microdissection Testicular Sperm Extraction (MD-TESE).

In terms of the sperm retrieval rate and level of invasiveness, MD-TESE is the best method [15, 16]. In MD-TESE, the sperm is extracted from the seminiferous tubule by using a microscope. In fact, it is possible for the sperm to exist in as a part of the seminiferous tubule. After extraction, in-vitro fertilization is done. However, according to some papers, the sperm retrieval rate is lower than the rate of OA. Hibi *et al.* attempted to compare the sperm retrieval rates between conventional TESE and MD-TESE. From the results, they found that the retrieval rate of MD-TESE is 25.8% and that of conventional TESE is 30.2%, thereby concluding that the MD-TESE does not improve the sperm retrieval rate [53]. Bernie *et al.* reviewed the related literature and found that the sperm retrieval rate of MD-TESE is about 60% [54]. These results suggest that increasing the sperm retrieval rate has remained challenging. One of the reasons for low retrieval rate is the sole use of visual information by a doctor when retrieving the sperm through MD-TESE. In other words, MD-TESE is done by qualitative judgment. This is the problem with MD-TESE. A good solution for improving the sperm retrieval rate is to utilize the quantitative data. A common characteristic of the seminiferous tubule of NOA patients is that its wall is thicker than that of normal patients [55]. Therefore, by measuring the thickness of the tubule's wall, the judgment of whether a patient has NOA or not is possible. However, measuring the thickness of the tubule's wall during an MD-TESE operation is difficult because of the length of time required for measurement.

Due to the reasons discussed above, hardness is used as a quantitative index instead of the thickness of the tubule's wall. Two experiments are done. First, the stiffness evaluation of a normal testis and a testis under the spermatogenesis model is done. In order to compare the difference of stiffness between each testis, 15 normal testes and 16 spermatogenesis-model testes are utilized. In addition, the stiffness evaluation of the seminiferous tubule between the cryptorchidism group and the normal group is described. In order to compare the difference of stiffness between each testis, 9 normal testes and 9 spermatogenesis-model testes are utilized.

This paper is organized into four sections as shown in Fig. 5.1. In Section 5.2, the spermatogenesis evaluation of the testis is described. In Section 5.3, the spermatogenesis evaluation of the semaphores tubule is described. The conclusion is presented in Section 5.4.

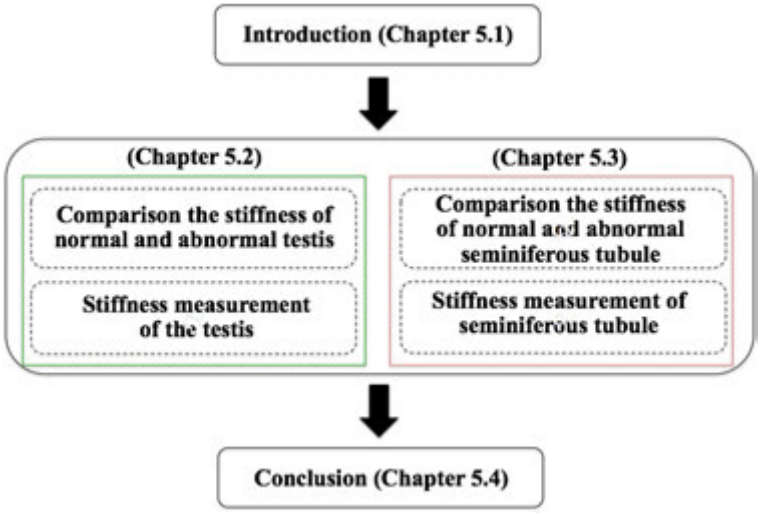

Fig. 5-1: Chapter Organization

5.2 Spermatogenesis Evaluation based on the Hardness Measurements of the Testis

This section describes a hardness evaluation of the testis between the cryptorchidism group and the normal group for NOA judgment. Two types of stiffness are used as the quantitative hardness index for the testis hardness evaluation. Both stiffness models are described in 5.2.1. In 5.2.2, a measurement method and experimental setup are described. In 5.2.3, the experimental results are described. Finally, the discussion is explained in 5.2.4.

5.2.1 Stiffness of the Testis

A testis consists of components such as the testis membrane, the stroma, and the seminiferous tubule. If these components are defined as the sub-systems of which the testis consists, the reaction force increases as the deformation of the testis increases. Then, the total reaction force can be expressed as

$$f_{\mathrm{t}}(q_{\mathrm{t}}, \dot{q}_{\mathrm{t}}) = \sum_{i}^{n} f_i(q_{\mathrm{t}}, \dot{q}_{\mathrm{t}}), \tag{5.1}$$

where f_{t} is the total reaction force from the components, f_i is the reaction force from ith component, and n is the total number of the components. The components include the elastic effect and viscous effect.

Therefore, the reaction force from one sub-system can be expressed as

$$f_i(q_i, \dot{q}_i) = k_i q_i + d_i \dot{q}_i, \tag{5.2}$$

where k_i is the stiffness of the ith sub-system, d_i is the viscosity of the i sub-system, q_i is the deformation generated ith sub-systems, and $\dot{q}_i$ is the deformation velocity generated ith sub-systems. Then, the total reaction force can be expressed by using the stiffness and viscosity of each sub-system as follows:

$$f_{\mathrm{t}}(q_{\mathrm{t}}, \dot{q}_{\mathrm{t}}) = \sum_{i}^{n} k_i q_i + \sum_{i}^{n} d_i \dot{q}_i. \tag{5.3}$$

In actual situations, measuring the deformation of each sub-system is difficult. Thus, by using the total deformation amount, q_{t}, Eq. (5.3) is rewritten as

$$f_{\mathrm{t}}(q_{\mathrm{t}}, \dot{q}_{\mathrm{t}}) = K_{\mathrm{t}}(q_{\mathrm{t}}) q_{\mathrm{t}} + D_{\mathrm{t}}(\dot{q}_{\mathrm{t}}) \dot{q}_{\mathrm{t}}, \tag{5.4}$$

where q_{t} is the deformation amount generated at the testis, $\dot{q}_{\mathrm{t}}$ is the deformation velocity, $K_{\mathrm{t}}(q_{\mathrm{t}})$ is the non-linear stiffness, and $D_{\mathrm{t}}(\dot{q}_{\mathrm{t}})$ is the non-linear viscous coefficient. Therefore, stiffness and viscosity are varied by the deformation amount and velocity. The mechanical model expressed as Eq. (5.4) includes the influence of viscosity. In order to exclude the influence of viscosity, the deformation velocity is set to very slow. Thus, Eq. (5.4) is rewritten as

$$f_{\mathrm{t}}(q_{\mathrm{t}}, \dot{q}_{\mathrm{t}} \approx 0) \approx K_{\mathrm{t}}(q_{\mathrm{t}}) q_{\mathrm{t}} \tag{5.5}$$

In addition, the linear approximation is applied to simplify the non-linear characteristics. The linear approximation is expressed as

$$f_{\mathrm{t}}(q_{\mathrm{t}}) \approx \tilde{K}_{\mathrm{t}}(q_{\mathrm{t}}) q_{\mathrm{t}}, \tag{5.6}$$

where $\tilde{K}_{\mathrm{t}}$ is the linear approximation of time-variant stiffness. The linear approximation can be expressed in detail as

$$\tilde{K}_{\mathrm{t}}(q_{\mathrm{t}}) = \frac{f_{\mathrm{t}}^{\mathrm{init}}}{q_{\mathrm{t}}^{\mathrm{init}}} + \frac{1}{m} \sum_{j=1}^{m} K_j, \tag{5.7}$$

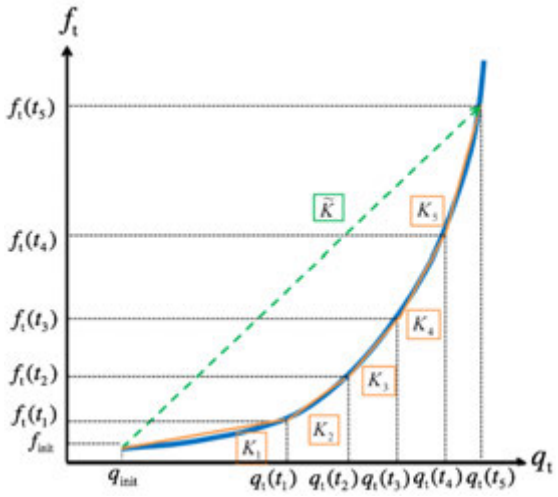

Fig. 5-2: Relationship Between $\tilde{K}_t$ and K_j

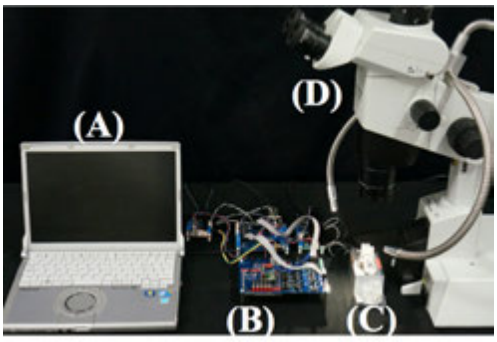

(a) Whole System

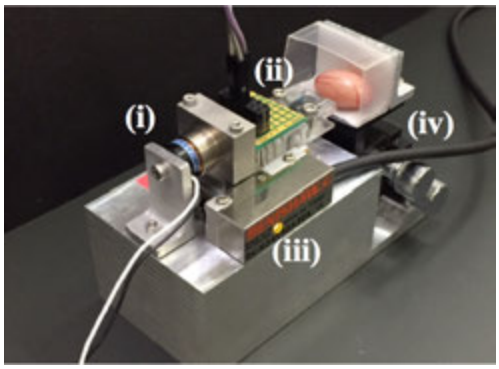

(b) Measurement Device

Fig. 5-3: The Whole Testis Stiffness Measurement System

where K_j is the minor change of stiffness, j is the sample number, m is the maximum number of samples. Here, the minor change stiffness can be expressed as

$$K_j = \frac{f_t(t_j) - f_t(t_{j-1})}{q_t(t_j) - q_t(t_{j-1})}, \tag{5.8}$$

where t_j is the time in the jth sample. The difference between $\tilde{K}_t$ and K_j is shown in Fig. 5-2.

Table 5.1: Parameters for the Experiments

Parameters	Descriptions	ValuesUnits
	Mechanical Parameters	
st	Sampling Time	0.1 msec
M_{n}	Nominal Mass of VCM	0.03 kg
$K_{\tau \mathrm{n}}$	Nominal Torque Coefficient	0.56 N/A
	Control Parameters	
K_{p}	Position Gain	3600.0 s^{-2}
K_{v}	Velocity Gain	120.0 s^{-1}
g_{dob}	Cut-off Frequency of DOB	100.0 rad/sec
g_{pd}	Cut-off Frequency of Pseudo Differentiation	200.0 rad/sec

5.2.2 Measurement and Control Method

System Configurations and Control Method

Experimental systems are shown in Fig. 5-3(a). Four systems are used for the experiment: (A) represents a personal computer to control the actuators; (B) is a control system (the microcontroller [STMicroelectronics Co., Ltd: STM32F411RET6 MCU], linear amplitude motor driver, counter board, 13-bit analog-digital convertor); (C) is a measurement device; and (D) is a microscope. Fig. 5-3(b) shows the structure of the measurement device: (i) is a Voice Coil Motor (VCM) used to achieve a pushing motion; (ii) is a micro force (FTS-10000, FEMTO TOOLS A.G.); (iii) represents a linear encoder (RGH24, RENISHAW plc.) used to measure the VCM's position; and (iv) is an XZ mechanical stage (XZmechanicalstage, Misumi, Inc.). The testis is set on a wet box to prevent drying. The measurement motion is produced by position control implemented with a minimum-order DOB. The parameters of position control are shown in Table 5.1. The specifications of the micro force sensor are shown in Table 5.2. The sensing probe is made from silicone. The tip of this sensing probe (the shape is 50 μm square) makes contact with the testis, and the force is measured by the deformation of the sensing probe. The sensor's shape is shown in Fig. 5-4. The measurement motion is shown in Fig. 5-5. In the initial state, the sensing probe makes contact with the surface of the testis (Fig. 5-5(a)). Afterwards, a pushing motion is started (Fig. 5-5(b)). The motion is stopped when the position reaches the setting position (Fig. 5-5(c)). The stiffness of the testis is calculated by using the results of the position and reaction force.

Table 5.2: Specifications of a Micro Force Sensor (FEMTO TOOLS FTS-10000).

Descriptions	**Values**	**Units**
Force Resolution (10Hz)	0.5	μN
Maximum Deformation of Measurement Tip	1.5±0.5	μm
Sensor Force Range	±10000.0	μN
Stiffness of Measurement Tip	6666.7	μN/μm
Sensor Gain	5000.0	μN/V
Resolution of AD Convertor	13	bit

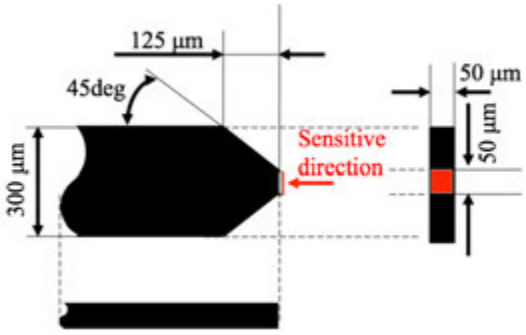

Fig. 5-4: Micro Force Sensor's Shape (FEMTO TOOLS FTS-10000)

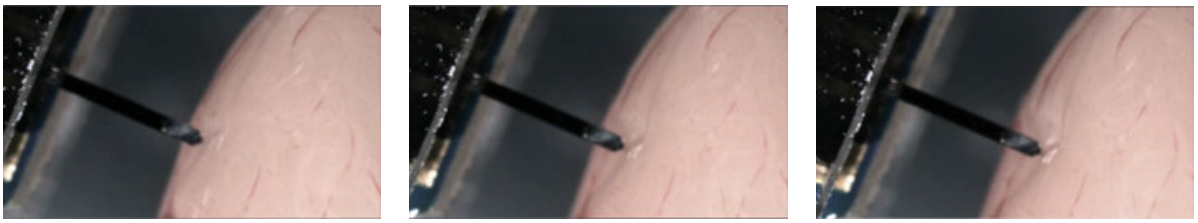

(a) Initial Position (b) Pushing Motion (c) Finish

Fig. 5-5: Scheme of the Testis Stiffness Measurement Motion

Stiffness Model Validation Experiment Setup

In this research, the testis includes the stiffness component and the viscous component as defined in Eq. (5.4). The influence of both components is confirmed by two pre-experiments. The first experiment is the confirmation of viscosity dependency. The linearity of stiffness is confirmed by the five different constant velocity test. The four different velocity commands are set as $\dot{q}^{\mathrm{cmd1}}$ = 10.0, $\dot{q}^{\mathrm{cmd2}}$ = 50.0, $\dot{q}^{\mathrm{cmd3}}$ = 100.0, $\dot{q}^{\mathrm{cmd4}}$ = 500.0 [μm/sec], and the deformation amount is set to 500μm. Mechanical impedance, which is defined in Eq. (5.9), is calculated by using the velocity of the VCM and the instant reaction force obtained by the micro force sensor. Here, the instant reaction force is defined as the reaction force

when the VCM reaches $500\mu\mathrm{m}$:

$$\frac{f(q,\dot{q})}{q} = G(q,\dot{q}) \tag{5.9}$$

The second experiment is the confirmation of stiffness dependency. The linearity of stiffness is confirmed by the constant velocity test. The five position commands are set as, q^{cmd1} = 400.0, q^{cmd2} = 800.0, q^{cmd3} = 1200.0, q^{cmd4} = 1600.0, q^{cmd5} = 2000.0 [μm], and the velocity command is set to $50\mu\mathrm{m/sec}$. Mechanical impedance, which is defined in Eq. (5.9), is calculated by using the position response of the VCM and the reaction force obtained by the micro force sensor.

Hamster Model with Experimental Cryptorchidism

Eleven to fourteen week-old male Syrian hamsters with bilateral experimental cryptorchidism are used as the NOA model. Hamsters are anesthetized by using Isoflurane (Wako Pure Chemical Industries). The left-side testis is lifted up to the abdominal cavity, and both testes are extracted after two weeks. The left-side testes are defined as the cryptorchidism group (Crypt) and the right-side testes are defined as the control group (Control).

Stiffness Measurement Method and Spermatogenesis Pathological Evaluation Method

The testis used for stiffness measurement is extracted from the Syrian hamsters after euthanasia by CO2 gas. The adipose tissues are removed, and all of the testes are placed in a plastic petri dish and preserved at 4 degrees. Stiffness is measured at five points, as shown in Fig. 5-6, in order to take into account the contact angle of the sensor's probe and the regional differences of the testis. The horizontal and vertical direction adjustments are made on the XZ mechanical stage, and the measurement order is defined as Center-Right-Left-Down-Up. The maximum deformation amount is set to $500\mu\mathrm{m}$ and the deformation velocity is set to $10.0\mu\mathrm{m/sec}$. The measured testes are fixed by the bounds solution, and the preparation of the paraffin-embedded specimens is conducted. In addition, the Hematoxylin and Eosin stain (HE stain) is done. The Johnsen score (JS) [56], which is a quantitative score for spermatogenesis maturity (from 1 to 7), is used in spermatogenesis evaluation. Thirty different cross-sectional areas of the seminiferous tubule are evaluated, with the average value being used as the JS. As the JS is generally used for the spermatogenesis evaluation of humans, it is modified in this research for the spermatogenesis evaluation of hamsters. If the JS is within 5, we apply the normal JS. If the maturity of the sperm cell reaches the stage of round spermatids, the JS is defined as 6. If the maturity of the sperm cell reaches the

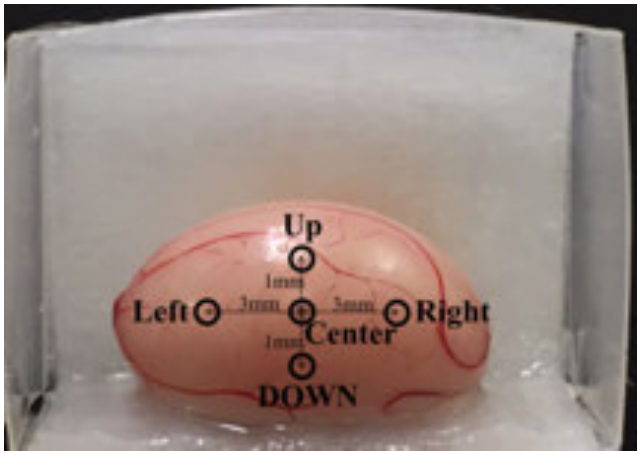

Fig. 5-6: Stiffness Measurement Points

stage of initial elongation, the JS is defined as 6.5. Moreover, if the maturity of the sperm cell reaches the stage of late elongation, the JS is defined as 7.

Morphological Evaluation

A morphological evaluation is done for all measured testes. The following five terms are evaluated: (i) thickness of the testis membrane, as shown in Fig. 5-7(a) (10 points are measured per one testis); (ii) occupancy rate of the seminiferous tubule, as shown in Fig. 5-7(b) (1 point is calculated per one testis), (iii) thickness of the seminiferous tubule's basement membrane, as shown in Fig. 5-7(c) (100 points are measured per one testis); (iv) thickness of the seminiferous tubule's cell layer, as shown in Fig. 5-7(e) (50 points are measured per one testis); and (v) diameter of the seminiferous tubule, as shown in Fig. 5-7(d) (10 seminiferous tubules are measured per one testis). All terms are compared with those of the normal testis, and a significance test by the paired t-test is conducted.

Static Analysis Method

Static analysis is done by using JMP ver. 12 (SAS Japan) and R version 3.1.3. Analysis of variance is used for the multiple group comparison and a paired t-test is used for the two dependent groups. The significant probability is set to 5% for both analyses.

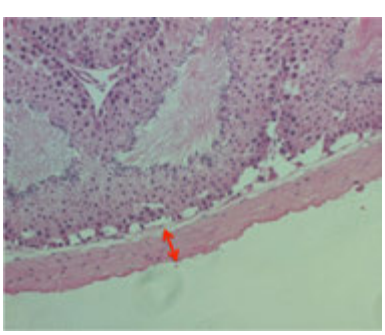

(a) Thickness of Testis Membrane

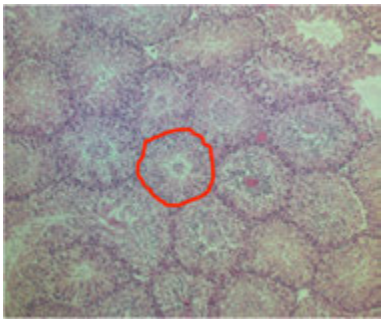

(b) Occupancy Rate of the Seminiferous Tubule

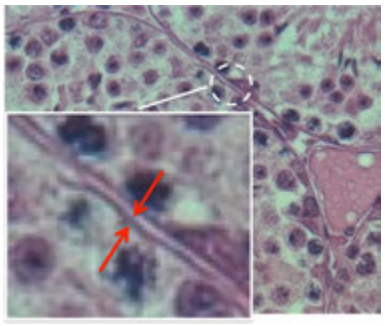

(c) Thickness of the Seminiferous Tubule's Basement Membrane

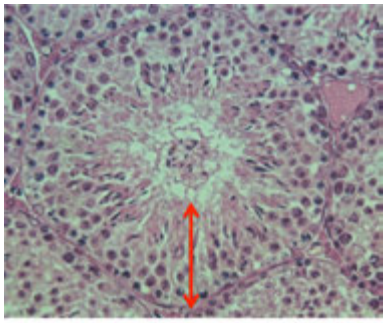

(d) Thickness of the Seminiferous Tubule's Cell Layer

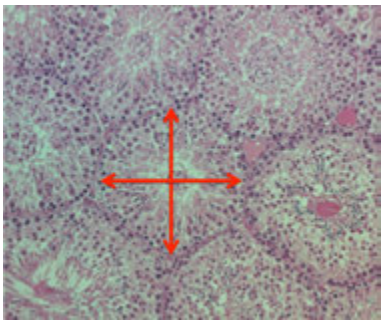

(e) Diameter of the Seminiferous Tubule

Fig. 5-7: Scheme of Morphological Analysis

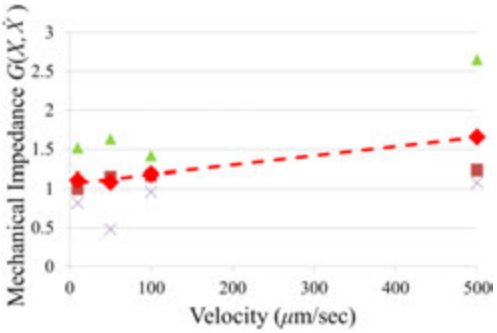

(a) Dependency of the Deformation Velocity

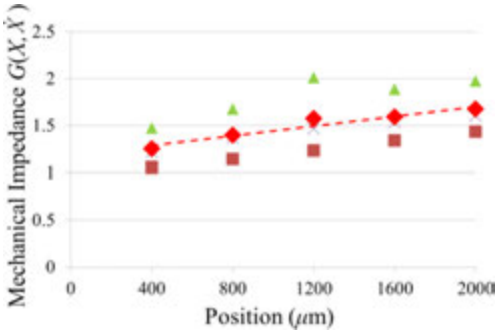

(b) Dependency of the Deformation Amount

Fig. 5-8: The Whole Seminiferous Tubule Stiffness Measurement System

5.2.3 Experimental Results

Model Validation Results

Fig. 5-8(a) shows the mechanical impedances for four different velocity commands. As shown in Fig. 5-8(a), mechanical impedance increases when the velocity increases. The maximum deformation

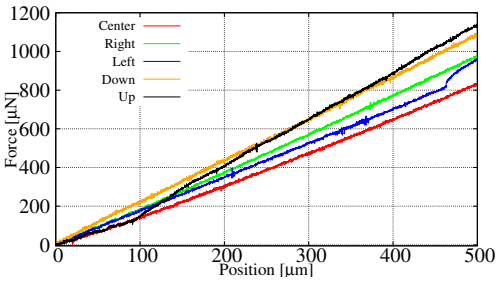

(a) Normal Testis

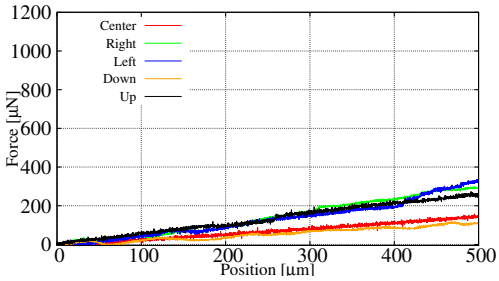

(b) Crypt Testis

Fig. 5-9: Position vs Force Plots of the Testis's Stiffness

Table 5.3: Results of the ANOVA for the Stiffness Variation between Each Experimental Day

day	n	mean±SD	p-value	α
1st	2	1.674±0.458		
2nd	3	1.432±0.335		
3rd	3	1.594±0.271		
4th	7	1.354±0.288		
Total	15	1.460±0.313	0.5341	>0.05

Table 5.4: Results of the ANOVA for the Stiffness Variation at Each Measurement Point

Point	n	mean±SD	range
Center	43	1.041±0.572	0.218-2.266
Right	43	1.051±0.575	0.187-2.185
Left	43	1.039±0.583	0.163-2.109
Bottom	43	1.096±0.642	0.200-2.398
Upper	43	1.008±0.601	0.195-2.280
Total	215	1.047±0.589	0.163-2.398

is the same in all cases while the increase of mechanical impedance is due to the influence of viscosity. Therefore, the testes are influenced by viscosity. The operator would need to select a low-speed pushing command in order to avoid the viscous effect. In this research, the effect of viscosity (i.e., within 100.0 μm/sec of the experimental results) is small enough to be ignored.

Correspondingly, the results of the mechanical impedances for five different position commands are shown in Fig. 5-8(b). The results presented in Fig. 5-8(b) are similar to the results presented in Fig. 5-8(a). Mechanical impedance increases with the increase of the deformation amount. The velocity commands are set as the same value in all cases. Consequently, the increase of mechanical impedance is due to the increase of stiffness. If stiffness has linearity, a constant value would be obtained even if the deformation amount increases. However, the results presented in Fig. 5-8(b) are not constant. Thus, the stiffness of the testis has a non-linear effect. The non-linearity is approximated by the linear approximation defined

Table 5.5: Results of the t-test for $\tilde{K}_{\mathrm{t}}$ and Other Parameters

	Control($n = 15$)		Crypt($n = 16$)		p-Value	α
	mean±SD	range	mean±SD	range		
Testis's Mass	1.86 ± 0.15	1.52-2.08	0.614±0.118	0.42-0.89	< 0.00001	< 0.01
Major Axis	20.9±0.80	19.0-22.0	15.2±1.22	13.0-18.0	< 0.00001	< 0.01
Minor Axis	14.7±0.70	14.0-16.0	10.4±1.15	8.0-13.0	< 0.00001	< 0.01
Stiffness	1.46±0.31	1.01-2.00	0.40±0.13	0.24-0.68	< 0.00001	< 0.01
Johnsen score (1-7)	6.96±0.04	6.9-7.0	4.08±0.71	2.93-5.43	< 0.00001	< 0.01

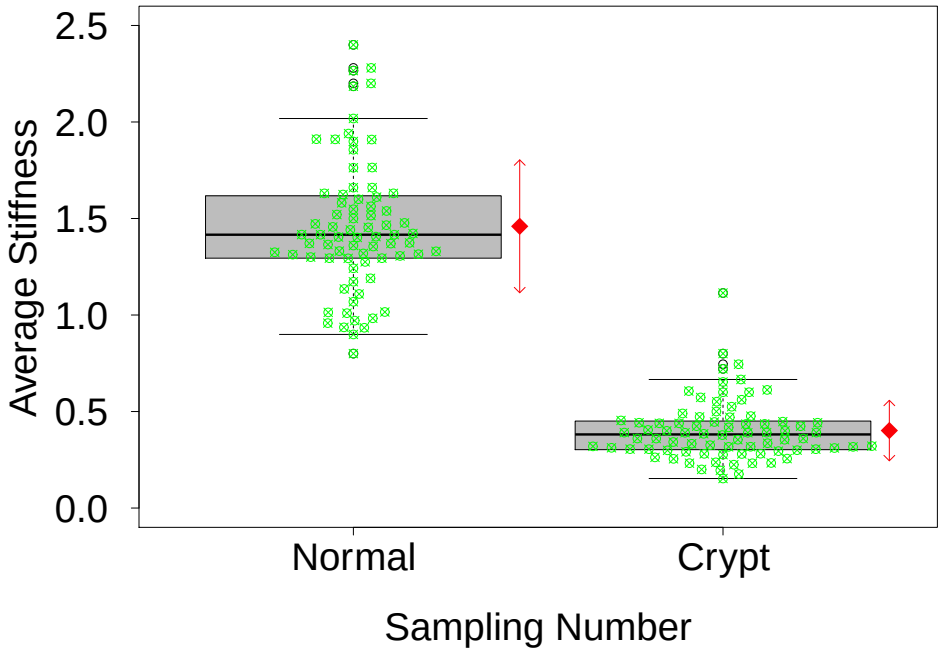

Fig. 5-10: Results of the Box plot and the Beeswarm between the Normal and the Crypt Testis's Stiffness.

in Eq. (5.7).

Stiffness Variation between Each Experimental Day

The average stiffness of the control group on each experimental day is compared by the analysis of variance (ANOVA). The results of average stiffness and the results of the t-test for each experimental day are shown in Table 5.3, where α shows the significant probability. As indicated by the results, the average stiffness recorded on each experimental day does not depend on the experimental day ($p = 0.53$). Thus, we are not required to take into account the variation of testis stiffness between each experimental day.

Stiffness Variation at Each Measurement Point

The average stiffness of the control group at each measurement point is compared by the ANOVA. The results are shown in Table 5.4. In addition, the stiffness data are analyzed by the paired t-test. From the results of the paired t-test, we find no significant differences among the measurement points. Thus, we are not required to take into account the variation of testis stiffness at each measurement point.

Comparison of the Average Stiffness and Other Parameters

Fig. 5-9 shows an example of the position vs the force plot for each measurement point of the testis's stiffness. Further, measurement results of the testis mass, the size of the testis between the control group and the crypt group, the average stiffness, $\tilde{K}_{\mathrm{t}}$, and the JS are shown in Table 5.5. Each parameter between the control group and the crypt group is compared by using the paired t-test. All parameters have a significant difference, and spermatogenesis failure is clearly recognized. In addition, the box plot of the average testis stiffness with the beeswarm between the normal testis and the crypt testis is shown in Fig. 5-10. Where, green plots are the beeswarm results, red diamond is the average of the $\tilde{K}_{\mathrm{t}}$ and red arrow is the standard derivation. From Fig. 5-10, the stiffness of the both testis is significant difference.

Comparison of Minor Stiffness, K_j

Fig. 5-11 shows the box plot with beeswarm of the minor stiffness, K_j between the normal group and the crypt group. In this figure, the blue line indicates the approximation of K_j. The results show that the slope of the minor stiffness, K_j of the crypt group is larger than that of the normal group. The dynamic characteristic is varied. The results of the approximation line of the stiffness of the normal testis and the crypt testis were $K_j = 0.047j + 1.2$ and $K_j = 0.0037j + 0.42$, respectively.

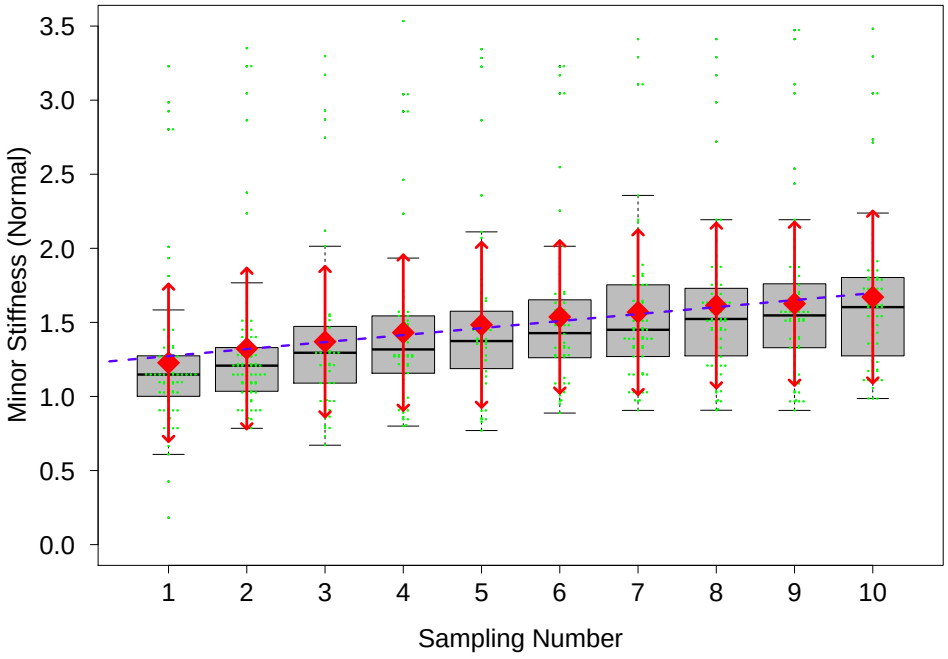

(a) Normal Group

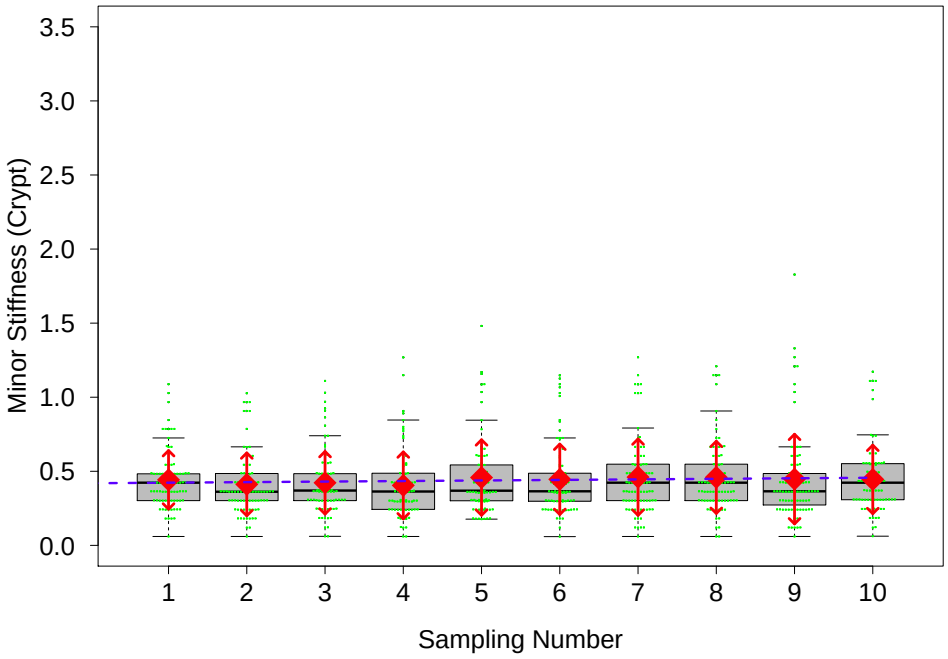

(b) Crypt Group

Fig. 5-11: Results of the Box plot and the Beeswarm between the Normal and the Crypt Testis's Minor Stiffness

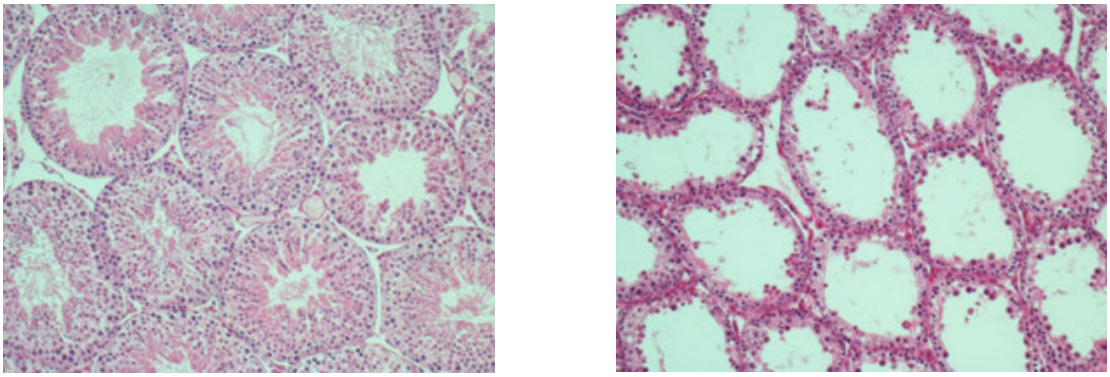

(a) Normal Group (b) Crypt Group

Fig. 5-12: Histopathological Images.

Morphological Analysis

Fig. 5-12 shows the sectional area of the crypt group testis and the control group testis. The structure of the testis is clearly different. Fig. 5-13 shows the results of the morphological analysis. All results have significant differences between the crypt group and the control group. Fig. 5-13(a) and Fig. 5-13(b) show the thickness of the testis and the occupancy rate of the seminiferous tubules. As shown by both results, the testis membrane of the crypt group is thicker than that of the control group. However, the occupancy rate of the seminiferous tubes in the crypt group is smaller than that of the tubes in the control group. Fig. 5-13(d) and Fig. 5-13(e) show the results of the thickness of the seminiferous tubule's cell layer and the diameter of the seminiferous tubule. Both results have the same variation, and the thickness of the basement membrane and the diameter of the seminiferous tubule of the crypt group's seminiferous tubules are smaller than those of the control group. However, Fig. 5-13(c) shows a different result from those in Fig. 5-13(d) and Fig. 5-13(e). Therefore, the thickness of the seminiferous tubule's basement membrane in the crypt group is larger than that of the control group.

5.2.4 Discussions

In this section, the spermatogenesis model hamster testis is measured in order to verify the relationship between stiffness and the spermatogenesis testis for the treatment of NOA. The hardness of the testis is measured by the developed measurement device. Reaction force is measured by the micro force sensor and the pushing motion is produced via position control. The DOB is applied to position control to sup-

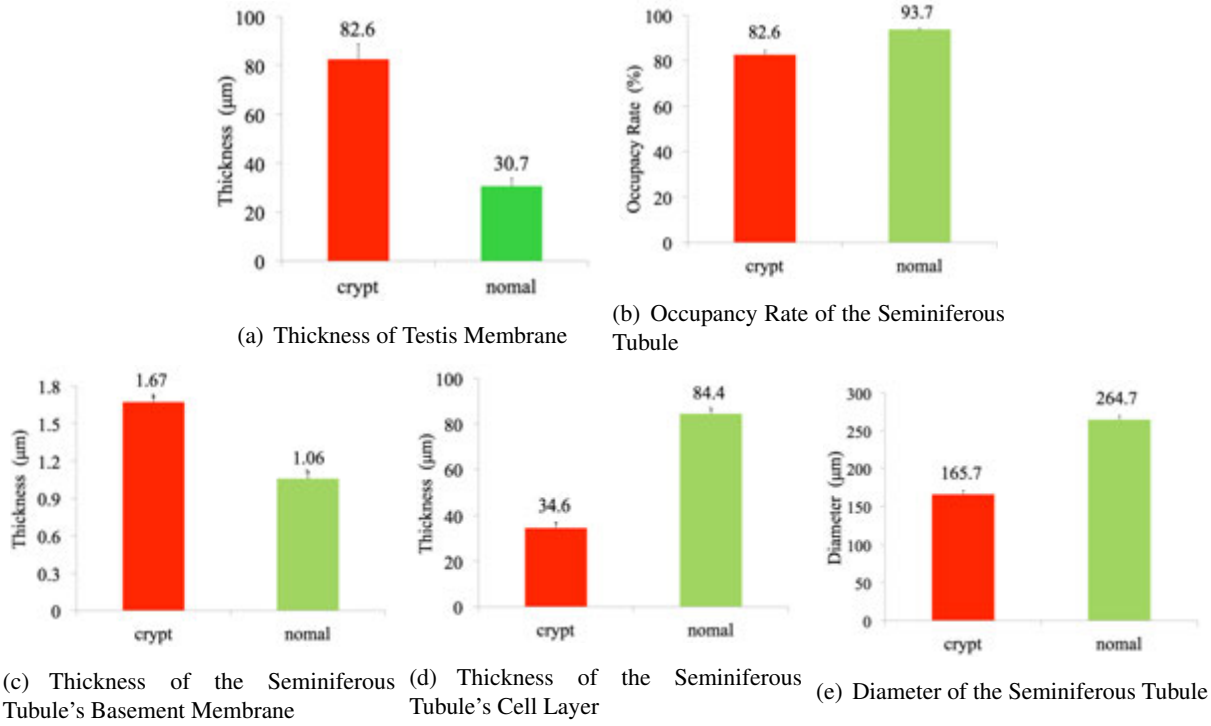

(a) Thickness of Testis Membrane

(b) Occupancy Rate of the Seminiferous Tubule

(c) Thickness of the Seminiferous Tubule's Basement Membrane

(d) Thickness of the Seminiferous Tubule's Cell Layer

(e) Diameter of the Seminiferous Tubule

Fig. 5-13: Results of the Morphological Analysis

press the unknown disturbance and modeling error. Hence, robust position control is achieved, allowing the operator to measure the hardness precisely. In addition, stiffness is calculated as a quantitative index of the hardness evaluation of the testis. This research applies two types of stiffness indexes so as to analyze the dynamic behavior (infinitesimal stiffness, K_j) and static behavior (average stiffness, $\tilde{K}$) of stiffness. The mechanical models are applied to both stiffness indexes. The validity of both stiffness indexes is confirmed by the pre-experiment, and the spermatogenesis of the Syrian hamster's testis is evaluated through static analysis. The normal testis and the experimentally cryptorchid testis are used for stiffness measurement. As shown in the measurement results, both stiffness indexes (K_j and $\tilde{K}$) have significantly low measurements in the case of the cryptorchidism model. As a conventional method for spermatogenesis evaluation, the histocytological preparation technique is well known. To the best of our knowledge, there are currently no techniques to evaluate spermatogenesis in the raw testis.

In this research, the maximum deformation amount is set to 500.0μm, and deformation velocity is set to 10.0 μm/sec. As shown in the results presented in Fig. 5-8(a), the viscous effect increases with the increase of deformation velocity. As the influence of the viscous effect requires suppression, deformation

velocity is set to 10.0 μm/sec. Correspondingly, the results presented in Fig. 5-8(b) show non-linearity in terms of stiffness. Therefore, the maximum deformation amount is set to 500.0 μm in order to achieve a definite pushing motion against the testis. From the morphological evaluation results, we find that the thickness of the testis membrane is about 25 30 μm. Hence, the thickness of the membrane is too small compared with the maximum deformation amount. The micro force sensor would have to measure the reaction force from the sub-systems.

Owing to the 50μm square shape of the tip of the micro force sensor, the probe does not pierce through the testis. In addition, the contact area is small compared to the area of the testis. Thus, the frictional force generated between the testis and the sensor's probe can be exceedingly small. For this reason, the micro force sensor with its particular shape is an appropriate sensing device for measuring the hardness of the testis.

In terms of infinitesimal stiffness, K_j, the K_j of the control group increases as the deformation amount increases. However, the K_j of the crypt group does not increase even if the deformation amount increases. In addition, from the viewpoint of morphological analysis, the occupancy rate of the seminiferous tubule and the thickness of the seminiferous tubule's cell layer both decrease. From these results, we gather that the density of the sub-systems in the crypt group testis would decrease compared with that of the control group.

Examining the morphological analysis outcomes, we find two interesting results.

- Morphological Analysis of Testicles

  The testis membrane of the crypt group is twice thicker than that of the control group. However, the occupancy rate of the seminiferous tubule in the crypt group is smaller than that of the control group. If the thickness of the membrane only becomes large without compositional transformation, the stiffness of the crypt group would be larger than the stiffness of the control group. Therefore, we have two assumptions regarding the cause of the decrease in stiffness in the crypt group. First, compositional transformation would occur in the testis membrane. Indeed, the membrane of the crypt group changes into two different layers. Second, the occupancy rate of the seminiferous tubule in the crypt group decreases. In other words, the area of the stroma increases in the crypt group. In this research, we cannot identify which assumption is correct. However, these results are interesting as they provide new knowledge.

- Morphological Analysis of Seminiferous Tubules

In the case of the seminiferous tubule of the crypt group testis, the diameter of the seminiferous tubule and the cell layer of the seminiferous tubule are smaller than those of the control group. However, the thickness of the basement membrane of the seminiferous tubule is larger than that of the control group. This variation is similar to that of the testis and we can predict that the hardness of the seminiferous tubule of the crypt group testis will be lower than that of the control group. In this research, the reason of this phenomenon could not identify. However, these results lead to two assumptions. First, the crypt group's testis and the seminiferous tubule would have undifferentiated sections and this undifferentiated section is included as a part of a basement membrane. Second, the structure of the basement membrane and the cell layer would be varied independently. As future works, it requires to identify this phenomenon.

5.3 Spermatogenesis Evaluation based on the Hardness Measurements of Seminiferous Tubules

This section describes the hardness evaluation of the seminiferous tubule between the cryptorchidism group and the normal group for NOA judgment. Two types of stiffness are used as the quantitative hardness index for the hardness evaluation of the testis. Both stiffness models are described in 5.3.1. In 5.3.2, a measurement method and the experimental setup are described. In 5.3.3, the experimental results are described. Finally, the discussion is explained in 5.3.4.

5.3.1 Modeling

Stiffness of the Seminiferous Tubule

A testis consists of some components, which are mostly occupied by seminiferous tubules. The seminiferous tubules entangle one another and become a ball of wall. When the membrane incised testis is deformed by the force sensor's probe, each tubule experiences a reaction force and the stroma experiences fluid viscosity. If the diameter of the probe is small enough compared to the diameter of the tubules, the measured reaction force could vary by the number of seminiferous tubules in serial connection. The purpose of this research is to ascertain only one seminiferous tubule's stiffness. Thus, the maximum deformation has to be within the diameter of the seminiferous tubule. According to the results of the morphological analysis as shown in Fig. 5-12, the maximum pushing deformation was set to 100 μm. The structure of the seminiferous tubule assumes a parallel connection with the spring and damping components. Thus, the total reaction force can be derived as

$$f_{\mathrm{sem}}(q_{\mathrm{sem}}, \dot{q}_{\mathrm{sem}}) = K(q_{\mathrm{sem}})q_{\mathrm{sem}} + D(\dot{q}_{\mathrm{sem}})\dot{q}_{\mathrm{sem}}, \tag{5.10}$$

where $K(q_{\mathrm{sem}})$ is the non-linear stiffness and $D(\dot{q}_{\mathrm{sem}})$ is the non-linear viscous coefficient described as

$$K_{\mathrm{sem}}(q_{\mathrm{sem}}) = \sum_{i}^{n} k_i \tag{5.11}$$

$$D_{\mathrm{sem}}(q_{\mathrm{sem}}) = \sum_{i}^{n} d_i, \tag{5.12}$$

where n is the maximum number of parallel connections with the spring components and i is the number of parallel connections with the spring components. This model is same to testis model described in

5.2.1. Consequently, the linear approximated stiffness in low speed deformation is expressed as

$$\tilde{K}_{\mathrm{sem}}(q_{\mathrm{sem}}) = \frac{f^{\mathrm{init}}}{q^{\mathrm{init}}} + \frac{1}{m}\sum_{i=1}^{m} K_j, \tag{5.13}$$

where $\tilde{K}_{\mathrm{sem}}(q_{\mathrm{sem}})$ is the linear approximated stiffness, the F^{init} is the reaction force generated at the contacted point of the seminiferous tubule, the X^{init} is the deformation amount during F^{init} measurement, j is the section number, and m is the number of the division for maximum deformation $q^{\max}$. Likewise, minor stiffness can be expressed as

$$\tilde{K}_j = \frac{F(t_j) - F(t_{j-1})}{q_{\mathrm{sem}}(t_j) - q_{\mathrm{sem}}(t_{j-1})}, \tag{5.14}$$

where t_j is the time in the jth sample. $\tilde{K}_{\mathrm{sem}}(q_{\mathrm{sem}})$ and the K_j are utilized as indexes of stiffness.

XYZ Manipulator

The stiffness measurement position is adjusted by an XYZ manipulator. The X and Y directions are controlled by linear actuators and the Z direction is controlled by a rotary actuator and a Z-direction mechanical stage. Then, the work space coordinate on the endpoint side is defined as

$$\begin{bmatrix} X \\ Y \\ Z \end{bmatrix} = \begin{bmatrix} q^{\mathrm{L1}} \\ q^{\mathrm{L2}} \\ \frac{l_z}{2\pi}\theta^{\mathrm{R1}} \end{bmatrix}, \tag{5.15}$$

where $\bigcirc^{\mathrm{L1}}, \bigcirc^{\mathrm{L2}}, \bigcirc^{\mathrm{R1}}$ are actuators for the XYZ manipulator, q is the position of the joint space, θ is the angle of the joint space, l_{z} is the pitch of the Z direction mechanical stage. Furthrer, the velocity of the work space coordinate is expressed as

$$\begin{bmatrix} \dot{X} \\ \dot{Y} \\ \dot{Z} \end{bmatrix} = \begin{bmatrix} \dot{q}^{\mathrm{L1}} \\ \dot{q}^{\mathrm{L2}} \\ \frac{l_z}{2\pi}\dot{\theta}^{\mathrm{R1}} \end{bmatrix}. \tag{5.16}$$

Therefore, the Jacobian matrix is expressed as

$$\begin{bmatrix} \dot{X} \\ \dot{Y} \\ \dot{Z} \end{bmatrix} = \boldsymbol{J}_{\mathrm{aco}} \begin{bmatrix} \dot{q}^{\mathrm{L1}} \\ \dot{q}^{\mathrm{L2}} \\ \dot{\theta}^{\mathrm{R1}} \end{bmatrix}. \tag{5.17}$$

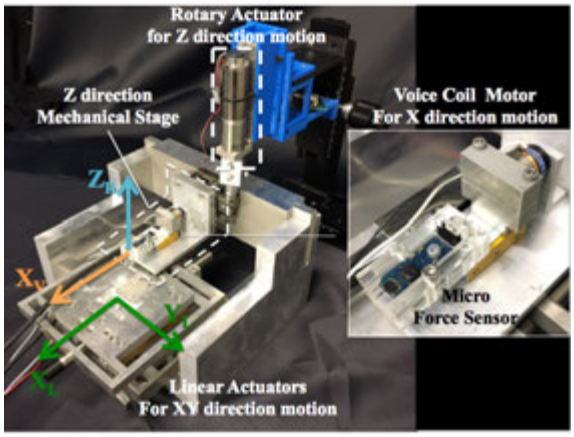

(a) An XYZ stage with a Micro Force Sensor and a VCM

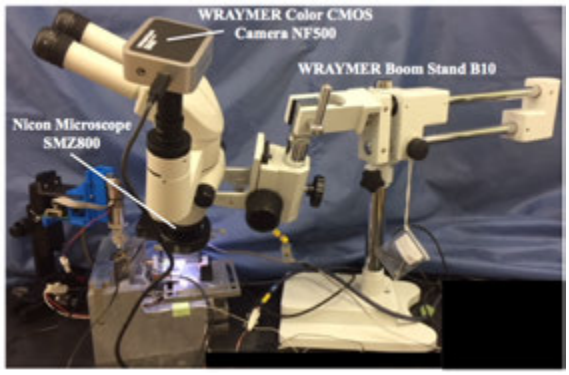

(b) Seminiferous Tubule Recording System

Fig. 5-14: Whole Systems of Seminiferous Tubule Stiffness Measurement System.

$$\boldsymbol{J}_{\mathrm{aco}} = \begin{bmatrix} 1 & 0 & 0 \\ 0 & 1 & 0 \\ 0 & 0 & \frac{l_{\mathrm{z}}}{2\pi} \end{bmatrix}. \tag{5.18}$$

The inverse Jacobian is expressed as

$$\boldsymbol{J}_{\mathrm{aco}}^{-1} = \begin{bmatrix} 1 & 0 & 0 \\ 0 & 1 & 0 \\ 0 & 0 & \frac{2\pi}{l_{\mathrm{z}}} \end{bmatrix}. \tag{5.19}$$

A motion equation of the XYZ stage is

$$\boldsymbol{f}^{\mathrm{ref}} = \boldsymbol{M}\boldsymbol{J}_{\mathrm{aco}}^{-1}\ddot{\boldsymbol{Q}}^{\mathrm{ref}}, \tag{5.20}$$

where $\boldsymbol{M}$ is the mass matrix, $\boldsymbol{f}^{\mathrm{ref}}$ is the force reference, and $\ddot{\boldsymbol{Q}}^{\mathrm{ref}}$ is the acceleration reference of joint space. Each matrix can be expressed as

$$\boldsymbol{f}^{\mathrm{ref}} = \begin{bmatrix} f^{\mathrm{refL1}} & f^{\mathrm{refL2}} & \tau^{\mathrm{refR1}} \end{bmatrix}^{\mathrm{T}}, \tag{5.21}$$

$$\boldsymbol{M} = \begin{bmatrix} M^{\mathrm{L1}} & 0 & 0 \\ 0 & M^{\mathrm{L2}} & 0 \\ 0 & 0 & J^{\mathrm{R1}} \end{bmatrix}, \tag{5.22}$$

$$\ddot{\boldsymbol{Q}}^{\mathrm{ref}} = \begin{bmatrix} \ddot{q}^{\mathrm{refL1}}, \ddot{q}^{\mathrm{refL2}}, \ddot{\theta}^{\mathrm{refR1}} \end{bmatrix}^{\mathrm{T}}. \tag{5.23}$$

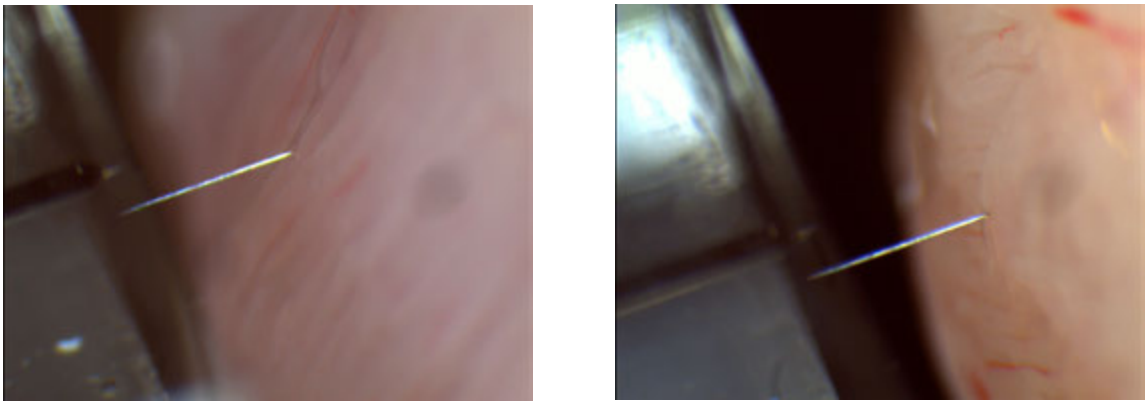

(a) Normal Seminiferous Tubule (b) Crypt Group Seminiferous Tubule

Fig. 5-15: Scheme of the Force Measurement of Seminiferous Tubules

Table 5.6: Specifications of the Micro Force Sensor (FEMTO TOOLS FTS-100).

Descriptions	**Values**	**Units**
Force Resolution (10Hz)	0.005	μN
Maximum Deformation of Measurement Tip	0.015±0.005	μm
Sensor Force Range	±100.0	μN
Stiffness of Measurement Tip	6666.7	μN/μm
Sensor Gain	50.0	μN/V
Resolution of AD Convertor	16	bit

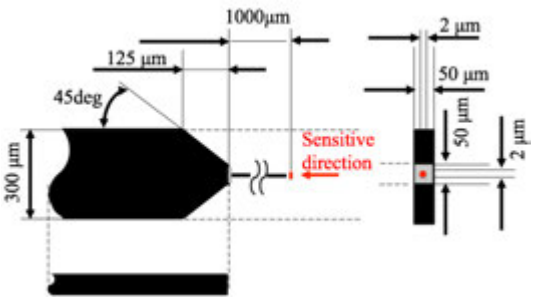

Fig. 5-16: Shape of the Micro Force Sensor (FEMTO TOOLS FTS-100).

5.3.2 Measurement and Control Method

Configurations

Fig. 5-14 shows the measurement system. This system has four Degree-of-freedoms (Dofs). The X- and Y-direction motions are controlled by two electromagnetic linear actuators (GHC Hillstone, Inc. S120D) and one VCM (Technohands AVM12-6.8). The Z-direction motion is controlled by a rotary actuator (MAXON, Inc. SDC22) and a mechanical stage (Misumi, Inc. ZLBS40). Three different motor drivers are used for each actuator. Linear actuators are actuated by the Movo SVFM series, 16-bit, current resolution motor driver. The VCM is actuated by the ELMO Gold Twitter, 12-bit, current

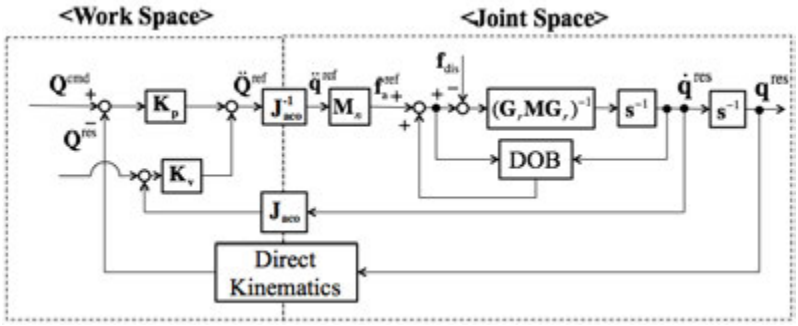

(a) Block Diagram of the XYZ Stage

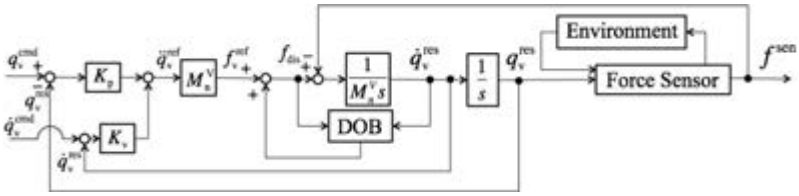

(b) Block Diagram of the Micro Force Measurement System

Fig. 5-17: Block Diagram of the Whole System

resolution motor driver. In addition, the rotary actuator is actuated by the Escon module 50/5. Position information is obtained by a linear encoder (RENISHAW.plc) and a rotary encoder (ESCON). A micro force sensor (FEMTO TOOLS FTS-100) is attached to the VCM. The force information obtained by the force sensor is transformed by a 16-bit analog digital convertor (LTC 1867). Specifications of the micro force sensor are described in Table 5.6. The sensor's probe consists of a silicone probe and a tungsten wire. The probe's deformation amount during its contact with the seminiferous tubule is transformed into the force value. Fig. 5-15 shows the scheme of the force measurement of the seminiferous tubule. Fig. 5-16 shows the outline of the shape of the force sensor's probe. The testis is mounted on an XYZ stage, and the pushing motion is monitored by a microscope (Nicon SMZ800) attached to a boom stand (WRAYMER B10). In addition, the pushing motion is recorded by a CMOS camera (WRAYMER NF500). In this paper, the electromagnetic linear actuator moving in the X direction is defined as $L1$, the electromagnetic linear actuator moving in the Y direction is defined as $L2$, the rotary actuator moving in the Z direction is defined as R, and the VCM moving in the X direction is defined as V.

Table 5.7: Specifications of The XYZ Mechanical Stage.

Parameters	**Descriptions**	**Values**	**Units**
	Control Parameters		
st	Sampling Time	0.1	msec
$K_{\mathrm{p}}^{\mathrm{L1}}, K_{\mathrm{p}}^{\mathrm{L2}}$	Positions Gains	2500.0	s^{-2}
$K_{\mathrm{p}}^{\mathrm{R1}}$	Positions Gains Actuators	2500.0	s^{-2}
$K_{\mathrm{v}}^{\mathrm{L1}}, K_{\mathrm{v}}^{\mathrm{L2}}$	Velocity Gains for X and Y Direction's Actuators	100.0	s^{-2}
$K_{\mathrm{v}}^{\mathrm{R1}}$	Velocity Gains for Z Direction's Actuators	100.0	s^{-2}
$g_{\mathrm{dob}}^{\mathrm{L1}}, g_{\mathrm{dob}}^{\mathrm{L2}}$	Cut-off Frequency of DOB	100.0	$\mathrm{rad/sec}$
$g_{\mathrm{dob}}^{\mathrm{R1}}$	Cut-off Frequency of DOB	100.0	$\mathrm{rad/sec}$
$g_{\mathrm{pd}}^{\mathrm{L1}}, g_{\mathrm{pd}}^{\mathrm{L2}}$	Cut-off Frequency of Pseudo Differentiation	200.0	$\mathrm{rad/sec}$
$g_{\mathrm{pd}}^{\mathrm{R1}}$	Cut-off Frequency of Pseudo Differentiation	100.0	$\mathrm{rad/sec}$
	Mechanical Parameters of S120D		
$M_{\mathrm{n}}^{\mathrm{L1}}, M_{\mathrm{n}}^{\mathrm{L2}}$	Actuator's Nominal Mass	0.4	kg
$K_{\mathrm{tn}}^{\mathrm{L1}}, K_{t\mathrm{n}}^{\mathrm{L2}}$	Nominal Torque Coefficient	3.5	$\mathrm{N/A}$
	Mechanical Parameters of DCX22		
Gr^{R1}	Gear Ratio	21.0	–
$J_{\mathrm{n}}^{\mathrm{R1}}$	Actuator's Nominal Inertia	0.75	kgm^2
	Mechanical Parameters of AVM12-6.8		
$M_{\mathrm{n}}^{\mathrm{V}}$	Actuator's Nominal Mass	0.03	kg
$K_{\mathrm{tn}}^{\mathrm{V}}$	Torque Coefficient	0.57	$\mathrm{N/A}$
	Mechanical Parameters of Z Stage		
l_{z}	Pitch	0.5	$\mathrm{mm}/2\pi$
L_{max}^{+}	Maximum Length	6.5	mm
L_{max}^{-}	Minimum Length	-6.5	mm

Control Design

Fig. 5-17 (a) shows a block diagram of a position control scheme on an XYZ stage, where $\boldsymbol{Q}$ is the matrix of the work space coordinate, $\boldsymbol{q}$ is the matrix of the joint space coordinate, $\boldsymbol{K}_{\mathbf{p}}$ is the matrix of

the position gain, $\boldsymbol{K}_{\mathrm{v}}$ is the matrix of the velocity gain, $\boldsymbol{M}_{\mathbf{n}}$ is the matrix of the nominal mass. $\boldsymbol{f}_{\mathbf{ext}}$ is the external force generated by actuators. Components of each matrix are expressed as

$$\begin{aligned}
\boldsymbol{s} &= \mathrm{diag}[s, s, s], \\
\boldsymbol{Q} &= [X, Y, Z]^{\mathrm{T}}, \\
\boldsymbol{q} &= [q_{\mathrm{L1}}, q_{\mathrm{L2}}, \theta_{\mathrm{R1}}]^{\mathrm{T}}, \\
\boldsymbol{K}_{\mathbf{p}} &= \mathrm{diag}[K_{\mathrm{p}}^{\mathrm{L1}}, K_{\mathrm{p}}^{\mathrm{L2}}, K_{\mathrm{p}}^{\mathrm{R1}}], \\
\boldsymbol{K}_{\mathbf{v}} &= \mathrm{diag}[K_{\mathrm{v}}^{\mathrm{L1}}, K_{\mathrm{v}}^{L2}, K_{\mathrm{v}}^{\mathrm{R1}}], \\
\boldsymbol{f}_{\mathbf{ext}} &= \mathrm{diag}[f_{\mathrm{L1}}^{\mathrm{ext}}, f_{\mathrm{L2}}^{\mathrm{ext}}, f_{\mathrm{R}}^{\mathrm{ext}}].
\end{aligned} \tag{5.24}$$

Fig. 5-17(b) shows a block diagram of the force measurement system, where q_{V} is the position of the VCM, $\dot{q}_{\mathrm{V}}$ is the velocity of the VCM, f^{sen} is the reaction force obtained by the micro force sensor, and M_{nV} is the mass of the VCM. Also, Table 5.7 shows control parameters for the XYZ stage.

Hamster Model with Experimental Cryptorchidism

Eleven to fourteen week-old male Syrian hamsters with bilateral experimental cryptorchidism are used as the NOA model. Hamsters are anesthetized by using Isoflurane (Wako Pure Chemical Industries). The left-side testis is lifted up to the abdominal cavity, and both testes are extracted after two weeks. The left-side testis is defined as the cryptorchidism group (Crypt) and the right-side testis is defined as the control group (Control).

Stiffness Measurement Method

The testes are placed in a plastic petri dish and are preserved at 4 degrees. The membrane of the testis is opened and the stiffness of the seminiferous tubule is measured at five random points. The operator can adjust the contact position between the force sensor's probe and the seminiferous tubule by using the XYZ stage. Position commands of two different scales are adopted for the XYZ stage. The small-scale position commands are set as follows:

$$\begin{aligned}
X^{\mathrm{cmd1}} &= 0.001\mathrm{mm}, \\
Y^{\mathrm{cmd1}} &= 0.001\mathrm{mm}, \\
Z^{\mathrm{cmd1}} &= 0.001\mathrm{mm}.
\end{aligned} \tag{5.25}$$

Table 5.8: Results of the ANOVA for the Stiffness Variation between Each Experimental Day

day	n	mean±SD	p-value	α
1st	3	0.845±0.0357		
2nd	4	0.123±0.0484		
3rd	4	0.112±0.0543		
Total	11	0.108±0.0489	0.076	>0.05

Table 5.9: Results of the ANOVA for the Stiffness Variation at Each Measurement Point

Point	n	mean±SD	range
A	10	0.121±0.0534	0.0731-0.238
B	9	0.0884±0.0407	0.0188-0.145
C	9	0.117±0.0376	0.0714-0.199
D	10	0.114±0.0559	0.0638-0.227
E	10	0.0992±0.0543	0.0142-0.198
Total	48	0.108±0.0489	0.0142-0.238

Moreover, the large-scale position commands are set as follows:

$$\begin{aligned} X^{\mathrm{cmd2}} &= 0.0001\mathrm{mm}, \\ Y^{\mathrm{cmd2}} &= 0.0001\mathrm{mm}, \\ Z^{\mathrm{cmd2}} &= 0.0001\mathrm{mm}. \end{aligned} \tag{5.26}$$

Constant velocity motion is adopted for the measurement of motion. The maximum deformation is set to $0.1\mathrm{mm}$ and the velocity is set to $10\mu\mathrm{m/sec}$.

Static Analysis Method

The static analysis is done by using SPSS 24 (IBM) and R version 3.1.3. An ANOVA is used for a multiple group comparison. Further, the two groups are compared by a t-test.

5.3.3 Experimental Results

Measurement Results

Fig. 5-18 shows the measurement plots of q_{sem} vs f_{sem}. From these results, the reaction force does not increase linearity when the deformation amount was increasing. Therefore, the stiffness became smaller and these results were same to the stiffness model described in Section 5.2.

Stiffness Variation between Each Experimental Day

The average seminiferous tubule of the control group on each experimental day is compared by the ANOVA. The results of the average seminiferous tubule and the results of the t-test on each experimental

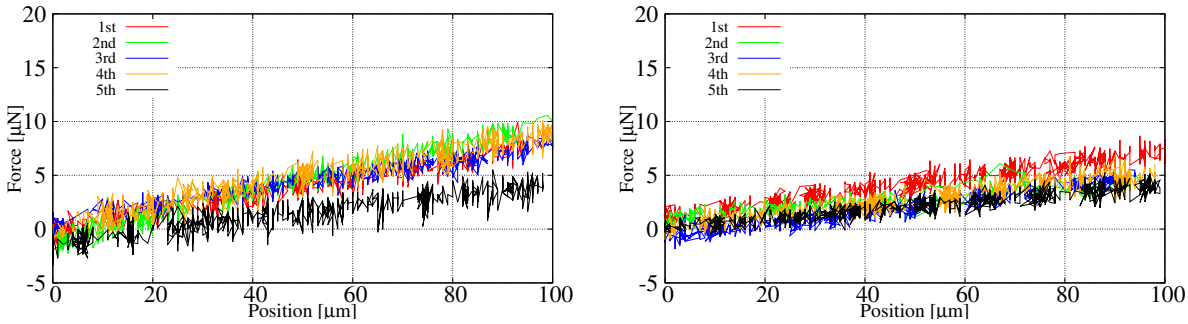

(a) Normal Group (b) Crypt Group

Fig. 5-18: Position vs Force Plots of the Seminiferous Tubule's Stiffness

day are shown in Table 5.8, where, α shows the significant probability. The results suggest that the average seminiferous tubule on each experimental day does not depend on the experimental day.

Stiffness Variation at Each Measurement Point

The average seminiferous tubule of the control group at each measurement point is compared by the ANOVA. The results are shown in Table 5.9. In addition, the stiffness data are analyzed by the paired t-test. From the results of the paired t-test, we find no significant differences among the measurement points. Thus, we are not required to take into account the variation of seminiferous tubule's stiffness at each measurement point.

Comparison of the Average Stiffness and Other Parameters

Experimental results of the average seminiferous tubule, $\tilde{K}_{\mathrm{sem}}$ and the size of the testis between the control group and the crypt group are shown in Table 5.10. Each parameter between the control group and the crypt group is compared by using the t-test. the box plot of the average seminiferous tubule stiffness with the beeswarm between the normal seminiferous tubule and the crypt seminiferous tubule is shown in Fig. 5-19. Where, green plots are the beeswarm results, red diamond is the average of the $\tilde{K}_{\mathrm{sem}}$ and red arrow is the standard derivation. From Fig. 5-19, the stiffness of the both testis is significant difference.

Table 5.10: Results of the t-test for $\tilde{K}$ and Other Parameters

	Control($n = 9$)		Crypt($n = 9$)		p-Value	α
	mean±SD	range	mean±SD	range		
Testis's Mass	1.96 ± 0.14	1.71-2.17	0.57±0.04	0.51-0.63	0.00	< 0.01
Major Axis	20.9±0.78	19.0-22.0	14.6±1.33	12.0-17.0	0.00	< 0.01
Minor Axis	14.9±0.93	13.0-16.0	9.78±0.83	8.0-11.0	0.00	< 0.01
Stiffness	0.11±0.05	0.014-0.24	0.07±0.03	0.013-0.16	0.000	< 0.01

Comparison of The Minor Stiffness K_j

Fig. 5-20 shows the results of the box plot with beeswarm of the minor stiffness K_j between the normal group and the crypt group. In this figure, the blue line indicates the approximation of K_j. The results of the regression line of normal testis is $K_j = 0.0015j + 0.12$. Also, the regression line of crypt testis is $K_j = 0.00068j + 0.15$. From the results, we find that the slope of the minor stiffness, K_j of the crypt group is larger than that of the normal group. However, the difference of the minor stiffness is smaller than the minor stiffness of the testis described in Fig. 5-10.

5.3.4 Discussions

In Section 5.3, the stiffness of the seminiferous tubule is measured and the spermatogenesis evaluation is done using the crypt group testis and the control group testis. The seminiferous tubules are measured by using an XYZ stage and a VCM with a micro force sensor. The stiffness of the seminiferous tubule is evaluated by two indexes ($\tilde{K}_{\rm sem}$ and K_j). The static characteristic of the seminiferous tubule is evaluated by $\tilde{K}_{\rm sem}$. In addition, the dynamic characteristic of the seminiferous tubule is evaluated by K_j. Both indexes are derived from the mechanical theory and are significantly different between the control group and the crypt group, as shown in the experimental results. To our knowledge, no study has attempted to compare the seminiferous tubule between the crypt group and the control group.

As evident in the results of the position vs. force plots, the non-linearity effect seems to increase with the increase of deformation. The cause of this phenomenon is the parallel connection between the

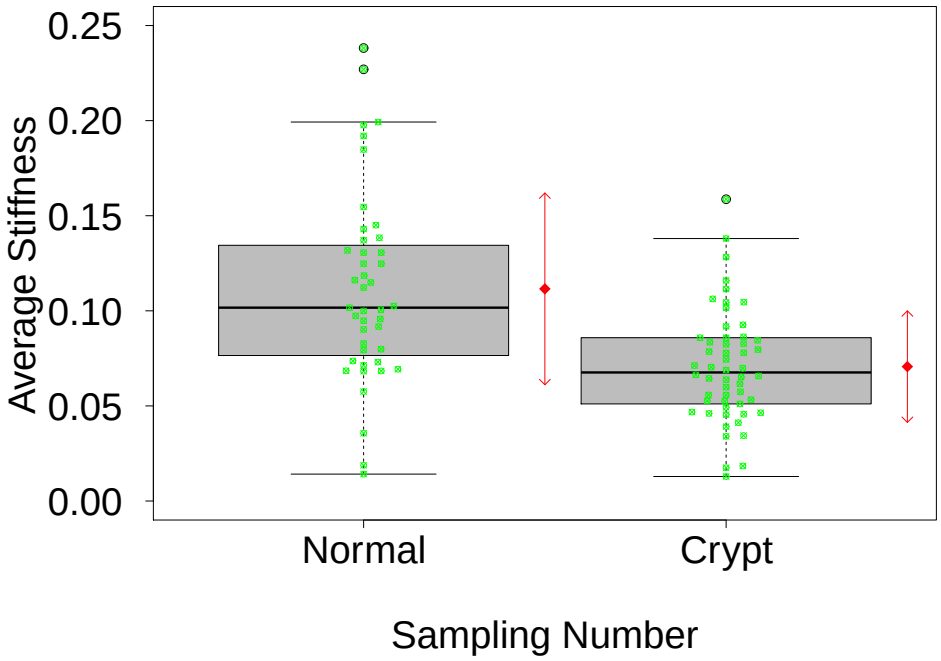

Fig. 5-19: Plots of the $\tilde{K}_{\mathrm{sem}}$ for Each Group

seminiferous tubules as described in 5.3.1. In this research, stiffness is measured by using the reaction force within a deformation amount of 100 μm deformation amount. In addition, as evident in the results of the morphology analysis shown in Fig. 5-12, the minimum diameter of the seminiferous tubule is 165.7 μm. Therefore, setting the deformation amount to within 165.7 μm is required for measuring the hardness of only one seminiferous tubule. For this reason, the deformation amount set is an appropriate value.

The seminiferous tubule is not extracted from the testis for the following two reasons: (i) the condition of the seminiferous tubule would change during hardness measurements. In particular, the amount of moisture in the seminiferous tubule would decrease dramatically; (ii) the sperm and other components in the seminiferous tubule would be lost after extraction from the testis. In this research, in order to capture the measurement point accurately, the XYZ mechatronic stage is developed and the contact points are observed by the microscope. The shape of the micro force sensor's tip is of a circular plane and the diameter is 2μm. Consequently, the contact area is small enough compared with the diameter of the seminiferous tubule. From these results, we gather that the hardness measurement method of using the developed measurement system is an appropriate solution for assessing the hardness of the seminiferous

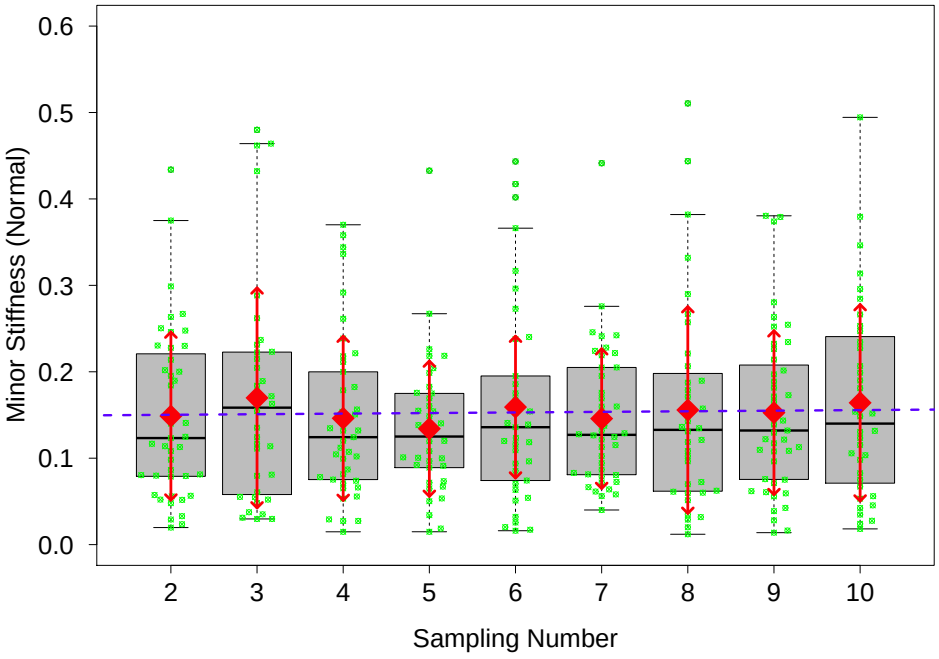

(a) Normal Group

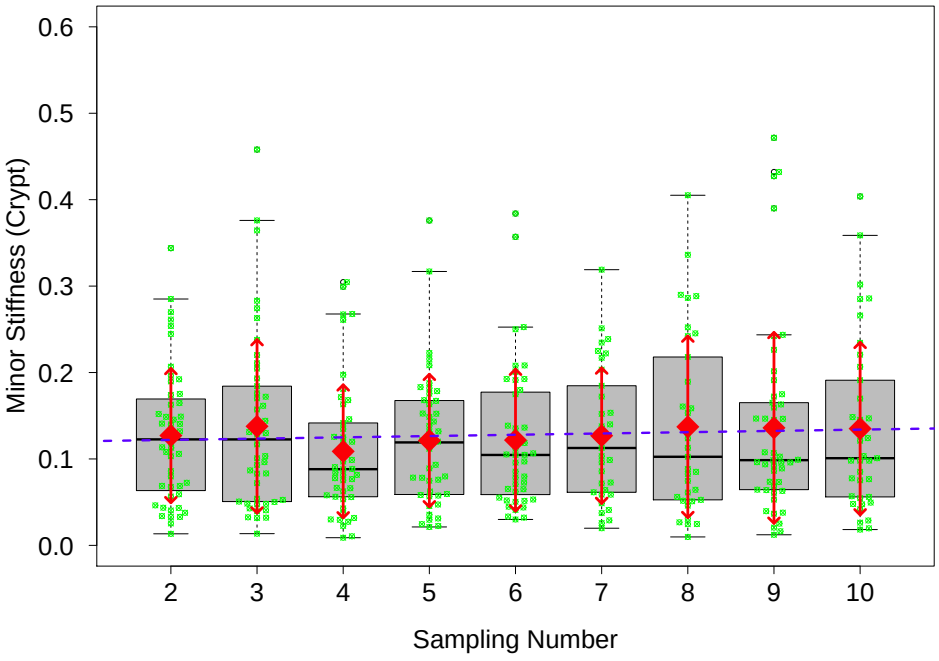

(b) Crypt Group

Fig. 5-20: Results of the Box plot and the Beeswarm between the Normal and the Crypt Seminiferous Tubule's Minor Stiffness

tubule.

5.4 Summary

This section describes the quantitative evaluation method for evaluating NOA. Stiffness is used as a quantitative index. The experiment is done by using Syrian hamsters, the testes and seminiferous tubules of which are evaluated. From the static analysis results, we find a significant difference between the crypt group and the control group. Therefore, our research has discovered a relationship between stiffness and NOA. To the best of our knowledge, this research is the first trial in the world to discover this result. This research contributes insight into the mechanisms of NOA.

Chapter 6

Conclusions

In this thesis, two studies are explained.

One is a development of a haptic medical application using EHTS control strategy. This applications aimed to apply the NOTES surgical operation. Two medical instruments are developed and the size of both instruments are within 2.6mm. In addition, the EHTS, which can transmit the position and the force information at the remote place by using fund energy, is applied to both instruments. This is the originality of this research. In my knowledge, there are no research to apply the hydraulic energy transmission based medical applications. From the experimental results, the transmission performance does not deteriorate under any wire's shape. This characteristics is a biggest advantage of the EHTS control strategy. In addition, the experimental results indicated to the EHTS does not depend on the temperature variation and time-related deterioration. Furthermore, the 4-ch. bilateral control is applied to both systems and the haptic sensation perforce was confirmed through the experiments.

From these results, the EHTS based medical instruments have a possibility to integrate with the remote medical tele-operation system. However, proposed system have some issues. First, the EHTS has a risk for liquid leaking. This phenomenon makes the position and the force transmission performance deteriorate. As a solution for liquid leaking, the rotary pomp to compensate the charge pressure should be implemented to the EHTS. Further, the mechanical sealing technologies such as an O-ring is also helpful to prevent the oil leaking. Second, the time response depends on the transmission liquid. In this research, the olive oil was chosen for the position and the force transmission and the arrival time to the steady state is late due to the viscosity of the olive oil. Also, bandwidth of the reaction force from the environment was narrow. Therefore, this system cannot transmit an impulsive force. The bandwidth

of the force transmission might be improved by using low-viscosity liquid such as a saline solution. However, there is a trade-off between the liquid leaking and the oil viscosity. Above problems would be considered as future works. Third, this research considers only only one DoF motion. In order to achieve a complex tasks, the multiple DoF systems using EHTS are required. This issue is must be considered as a future work.

In second study, development of a quantitative index for NOA judgement was discussed. This research was a first approach to evaluate the spermatogenesis quantitatively. This research makes a large impact for the urology fields. Syrian hamsters testicles and their seminiferous tubules are used for spermatogenesis evaluation. As a quantitative index, the stiffness, which is an index to express the hardness of the environment, is measured. In addition, the morphological analysis is conducted. From statistical analysis, the stiffness of the cryptorchidism model is significant low compared with the normal model and this results indicate that the stiffness is an effective index to identify the NOA patients.

Above evaluation results would be a good motivation to develop a remote surgical robot for NOA treatment by using the haptic technology. However, the mechanical structure of the measurement system described in this research is fragile due to the micro force sensor's structure. In case of NOA's operation such as MD-TESE, the measurement system should be more robust. From this reason, the development of the force sensor-less system for micro surgical operation is required.In addition, this research is only evaluated hamster's testis. In order to install the actual medical operation, it is necessary to evaluate the stiffness of human's testis. Both issues should be considered as future works.

From above results, the haptic technology is one of the helpful methods to solve the modern medical problems. In addition, the haptic technology is expected to apply any other medical applications outside of describing in this thesis.

References

[1] S. Lee-Kong and D. L. Feingold, "The History of Minimally Invasive Surgery", *Seminars in Colon and Rectal Surgery*, Vol. 24, No. 1, pp. 3–6, 2013.

[2] J. Marescaux and F. Rubino, "The ZEUS Robotic System: Experimental and Clinical Applications", *Surgical Clinics of North America*, Vol. 83, No. 6, pp. 1305–1315, 2003.

[3] M. P. Clark, E. S. Qayed, D. A. Kooby, S. K. Maithel, and F. F. Willingham, "Natural Orifice Translumenal Endoscopic Surgery in Humans: A Review", *Minimally Invasive Surgery*, Vol. 2012, No. 2012, pp. 1–8, 2012.

[4] T. Kawahara and M. Kaneko, "Non-Contact Stiffness Imager for Medical Application", *Proceeding of the IEEE International Conference on Information Acquisition*, pp. 350–355, 2005.

[5] G.T. Cao, P.F. Shi, and B Hu, "Liver Fibrosis Identification based on Ultrasound Images Captured under Varied Imaging Protocols.", *Journal of Zhejiang University Science B*, Vol. 6, No. 11, pp. 1107–1114, 2005.

[6] O. Oshiro, M. Suga, and M. Ohta, "Shear Modulus and Viscosity Measurement Using MR Elastography", *Medical Imaging Technology*, Vol. 19, No. 5, pp. 389–399, 2001.

[7] S. Audiere, Y. Mofid, and M. Chabit, "Fibroscan Practice Improvement with a Real-time Assistance Ultrasound Tool: A Preliminary Study", *Proceeding of the IEEE Ultrasounds Symposium*, pp. 1455–1458, 2009.

[8] M. Plodinec, M. Loparic, C. A. Monnier, E. C. Obemann, R. Zanetti-Dallenbach, P. Oertle, J. T. Hyotyla, U. Aebi, M. Bentires-Alj, Roderick Y. H. Lim, and C. A. Schoenenberger, "The Nanomechanical Signature of Breast Cancer", *Natrue Nanotechnology*, Vol. 7, pp. 757–765, 2012.

[9] P. Moreira, N. Zeimiti, C. Liu, and P. Poignet, "Viscoelastic Model Based Force Control for Soft Tissue Interaction and Its Application in Physiological Motion Compensation", *Computer Methods and Programs in Biomedicine*, Vol. 116, No. 2, pp. 52–67, 2014.

[10] S. Hyodo, Y. Soeda, and K. Ohnishi, "Verification of Flexible Actuator From Position and Force Transfer Characteristic and Its Application to Bilateral Teleoperation System", *IEEE Transactions on Industrial Electronics*, Vol. 56, No. 1, pp. 36–42, 2009.

[11] G. Palli and C. Melchiorri, "Optimal Control of Tendon-Sheath Transmission Systems", *International Federation of Automatic Control (IFAC) Proceedings Volumes*, Vol. 39, No. 15, pp. 73–78, 2006.

[12] S. J. Phee, A. P. Kencana, V. A. Huynh, Z. L. Sun, S. C. Low, K. Yang, D. Lomanto, and K. Y. Ho, "Design of A Master and Slave Transluminal Endoscopic Robot for Natural Orifice Transluminal Endoscopic Surgery", *Proceedings of the Institution of Mechanical Engineers, Part C: Journal of Mechanical Engineering Science*, Vol. 224, No. 7, pp. 1495–1503, 2010.

[13] T. N. Do and S. J. Phee, "Haptic Feedback in Natural Orifice Transluminal Endoscopic Surgery (Notes)", *arXiv.Org*, pp. 1–12, 2016.

[14] R. Kumar, "Medical Management of Non-obstructive Azoospermia", *Clinics*, Vol. 68, No. S1, pp. 75–79, 2013.

[15] A. A. Dabaja and P. N. Schlegel, "Microdissection Testicular Sperm Extraction: An Update", *Asian Journal of Andrology*, Vol. 15, No. 1, pp. 35–39, 2013.

[16] P. N. Schlegel, "Testicular Sperm Extraction: Microdissection Improves Sperm Yield with Minimal Tissue Excision", *Human Reproduction*, Vol. 14, No. 1, pp. 131–135, 1999.

[17] K. Ohnishi, M. Shibata, and T. Murakami, "Motion Control for Advanvced Mechatronics", *IEEE/ASME Transactions on Mechatronics*, Vol. 1, No. 1, pp. 56–67, 1996.

[18] K. Ohnishi, "Robust Motion Control by Disturbance Observer", *Journal of the Robotics Society of Japan*, Vol. 11, No. 4, pp. 486–493, 1993.

[19] T. Murakami, F. Yu, and K. Ohnishi, "Torque Sensorless Control in Multidegree-of-freedom Manipulator", *IEEE Transactions on Industrial Electronics*, Vol. 40, No. 2, pp. 259–265, 1993.

[20] S. Sakaino, T. Sato, and K. Ohnishi, "Multi-DOF Micro-macro Bilateral Controller Using Oblique Coordinate Control", *IEEE Transactions on Industrial Informatics*, Vol. 7, No. 3, pp. 446–454, 2011.

[21] E. Sariyildiz and K. Ohnishi, "A Guide to Design Disturbance Observer Based Motion Control", *Power Electronics Conference(IPEC-Hiroshima 2014 - ECCE-ASIA)*, pp. 2483–2488, May.2014.

[22] E. Sariyildiz and K. Ohnishi, "Stability and Robsutness of Disturbance Observer Based Motion Control Systems", *IEEE Transactions on Industrial Electronics*, Vol. 62, No. 1, pp. 414–422, 2015.

[23] T. Murakami, R. Nakamura, F. Yu, and K. Ohnishi, "Force Sensorless Compliant Control Based on Reaction Force Estimation Observer in Multi-Degrees-of-Freedom Robot", *Journal of the Robotics Society of Japan*, Vol. 11, No. 5, pp. 765–768, 1993.

[24] W. Iida and K. Ohnishi, "Reproducibility and Operationality in Bilateral Teleoperation", *Proceeding of the 8th IEEE International Workshop on Advanced Motion Control (AMC 2004)*, pp. 217–222, 2004.

[25] W. S. Liu and Y. Li, "The Research for Control Strategies and Methods of Teleoperation System", *World Automation Congress (WAC), 2012*, pp. 1–4, 2012.

[26] C. Basdogan, S. De, J. Kim, M. Muniyandi, H. Kim, and M. A. Srinivasan, "Haptics in Minimally Invasive Surgical Simulation and Training", *IEEE Computer Graphics and Applications*, Vol. 24, No. 2, pp. 56–64, 2004.

[27] A. M. Okamura, "Haptic Feedback in Robot-assisted Minimally Invasive Surgery", *Current Opinion in Urology*, Vol. 19, No. 1, pp. 102–107, 2009.

[28] H. Saafi, M. A. Laribi, S Zeghloul, and I. M. Yousef, "Teleoperation Control System For Non-Nomothetic Master/Slave Kinematics for Minimally Invasive Surgery", *Proceeding of the 2013 IEEE 39th Annual Conference of the IEEE Industrial Electronics Society (IECON 2013)*, pp. 3800–3805, 2013.

[29] H. Saafi, M. A. Laribi, S. Zeghloul, and I. M. Yousef, "Movement Safety Control Method of A Haptic Device for Minimally Invasive Surgery", *Proceeding of the 2014 IEEE 23rd International Symposium on Industrial Electronics (ISIE 2014)*, pp. 1233–1238, 2014.

[30] I. Nisky, F. A. Mussa-Ivaldi, and A. Karniel, "Analytical Study of Perceptual and Motor Transparency in Bilateral Teleoperation", *IEEE Transactions on Human-Machine Systems*, Vol. 43, No. 6, pp. 570–582, 2013.

[31] L. Chen, X. Wang, and W. L. Xu, "Inverse Transmission Model and Compensation Control of A Single-tendon-sheath Actuator", *IEEE Transactions on Industrial Electronics*, Vol. 61, No. 3, pp. 1424–1434, 2014.

[32] F. Bechet, K. Ogawa, E. Sariyildiz, and K. Ohnishi, "Electrohydraulic Transmission System for Minimally Invasive Robotics", *IEEE Transactions on Industrial Electronics*, Vol. 62, No. 12, pp. 7643–7654, 2015.

[33] N. S. Al-Waili, K. S. Saloom, T. N. Al-Waili, and A. N. Al-Waili, "The Safety and Efficacy of a Mixture of Honey, Olive Oil, and Beeswax for the Management of Hemorrhoids and Anal Fissure: A Pilot Study", *The Scientific World Journal*, Vol. 6, No. 2, pp. 1998–2005, 2015.

[34] A. . Erenel, G. Vural, Ş. Y. Efe, S. Özkan, S. Özgen, and R. Erenolu, "Comparison of Olive Oil and Dry-clean Keeping Methods in Umbilical Cord Care as Microbiological", *Maternal and Child Health Journal*, Vol. 14, No. 6, pp. 999–1004, 2010.

[35] C. Stoukides, "The galactopharmacopedia: Topical Meications and Breastfeeding", *Journal of Human Lactation*, Vol. 3, No. 9, pp. 185–187, 1993.

[36] M. J. Beelen, G. J. Naus, M. R. J. van de Molengraft, and M. Steinbuch, "Force Feedback Control Design for Nonideal Teleoperators", *Control Engineering Practice*, Vol. 21, No. 12, pp. 1694–1705, 2013.

[37] C. R. Wagner, N. Stylopoulos, and R. D. Howe, "The Role of Force Feedback in Surgery: Analysis of Blunt Dissection", *Proceedings of the 10th Symposium on Haptic Interfaces for Virtual Environment and Teleoperator Systems*, pp. 68–74, 2002.

[38] T. Ko, H. Kaminaga, and Y. Nakamura, "Underactuated Four-fingered Hand with Five Electro Hydrostatic Actuators in Cluster", *2017 IEEE International Conference on Robotics and Automation*, pp. 620–625, 2017.

[39] K. Ogawa, S. Uozumi, K. Yu, N. Wada, T. Uraoka, N. Yahagi, Y. Kitagawa, and K. Ohnishi, "Development of Miniature Haptic Forceps for Flexible Endoscope", *Journal of Japan Society of Computer Aided Surgery*, Vol. 17, No. 2, pp. 185–187, 2014.

[40] M. N. Mascarenhas, S. R. Flaxman, T. Boerma, S. Vanderpoel, and G. A. Stevens, "National, Regional, and Global Trends in Infertility Prevalence Since 1990: A Systematic Analysis of 277 Health Surveys", *PLoS Medicine*, Vol. 9, No. 12, pp. 1–12, 2012.

[41] P. Thonneau, S. Marchand, A. Tallec, M. L. Ferial, B. Ducot, J. Lansac, P. Lopes, J. M. Tabaste, and A. Spira, "Incidence and Main Causes of Infertility in A Resident Population (1,850,000) of Three French Regions (1988-1989)", *Human reproduction*, Vol. 6, No. 6, pp. 811–816, 1991.

[42] B. Maryland and B. Alabama, "Report on Optimal Evaluation of the Infertile Male", *Fertility and Sterility*, Vol. 82, No. 1, pp. 123–130, 2004.

[43] B. Alabama, "Diagnostic Evaluation of The Infertile Female: A Committee Opinion", *Fertility and Sterility*, Vol. 103, No. 6, pp. e44–e50, 2015.

[44] N. Akhter and S. Jebunnaher, "Evaluation of Female Infertility", *Journal of Medicine*, Vol. 13, No. 2, pp. 200–209, 2012.

[45] P. N. Schlegel, "Cause of Azoospermia and Their Management", *Fertility and Development*, Vol. 16, No. 5, pp. 561–572, 2004.

[46] B. Maryland and B. Alabama, "Report on Evaluation of the Azoospermic Male", *Fertility and Sterility*, Vol. 86, No. 4, pp. 210–215, 2006.

[47] B. Alabama, "Evaluation of The Azoospermic Male", *Fertility and Sterility*, Vol. 90, No. 5, pp. S74–S77, 2008.

[48] G. M. Willott, "Frequency of Azoospermia", *Forensic Science International*, Vol. 20, No. 1, pp. 9–10, 1982.

[49] J. P. Jarow, M. A. Espeland, and L. I. Lipshultz, "Evaluation of the Azoospermic Patient", *The Journal of Urology*, Vol. 142, No. 1, pp. 62–65, 1989.

[50] K. Baker and E. Sabanegh, "Obstructive Azoospermia: Reconstructive Techniques and Results", *Clinics*, Vol. 68, No. S1, pp. 61–73, 2013.

[51] N. Aziz, A. Agarwal, K. P. Nallella, and A. J. Jr. Thomas, "Relationship Between Epidemiological Features and Aetiology of Male Infertility as Diagnosed by A Comprehensive Infertility Service Provider", *Reproductive Biomedicine Online*, Vol. 12, No. 2, pp. 209–214, 2006.

[52] A. M. Jequier, "Obstructive Azoospermia: A Study of 102 Patients", *Clinical Reproduction and Fertility*, Vol. 3, No. 1, pp. 21–36, 1985.

[53] H. Hibi, T. Ohori, C. Ito, Y. Yamada, N. Honda, Y. Hashiba, and Y. Asada, "Microdissection TESE (MD-TESE) Does Not Improve Sperm Retrieval Rate but Contributes to Favourable Pregnancy Rate in Non-obstructive Azoospermic (NOA) Patients", *European Urology Supplements*, Vol. 7, No. 3, p. 126, 2008.

[54] A. M. Bernie, R. Ramasamy, and P. N. Schlegel, "Predictive Factors of Successful Microdissection Testicular Sperm Extraction", *Basic and Clinical Andrology*, Vol. 23, No. 5, pp. 1–7, 2013.

[55] Y. Sato, S. Nozawa, and T. Iwamoto, "Study of Spermatogenesis and Thickening of Lamina Propria in the Human Seminiferous Tubules", *Fertility and Sterility*, Vol. 90, No. 4, pp. 1310–1312, 2008.

[56] S. G. Johnsen, "Testicular Biopsy Score Count – A Method for Registration of Spermatogenesis in Human Testes: Normal Values and Results in 335 Hypogpnadal Males", *Hormones*, Vol. 1, No. 1, pp. 2–25, 1970.

List of Achievements

Journals (As a first author)

[1] Kenji Ogawa, Daisuke Tomizuka, Miki Yoshiike, Shiari Nozawa, Ryuto Nakazawa, Yoko Sato, Yasuhide Morikawa, Teruaki Iwamoto, and Kouhei Ohnishi, "A New Quantitative Method for Evaluating Spermatogenesis Based on Measurements of the Testis Hardness : A Studying Using a Hamster Model with Experimental Cryptorchidism," *Journal of The Japan Society of Computer Aided Surgery,* (Publication accepted.)

[2] Kenji Ogawa, Seiji Uozumi, Koyo Yu, Norihito Wada, Toshio Uraoka, Naohisa Yahagi, Yuko Kitagawa, and Kouhei Ohnishi, "Development of Miniature Haptic Forceps for Flexible Endoscope," *Journal of Japan Society of Computer Aided Surgery,* vol.17, No. 2, pp.91 – pp.100, 2015.

Journals (As a co-author)

[1] Takuya Matsunaga, Daisuke Tomizuka, Takahiro Nozaki, Saito Yuki, Kenji Ogawa, Kouhei Ohnishi, Norihito Wada, and Yuko Kitagawa, "Development of Miniature Haptic Forceps for Flexible Endoscope," *Journal of Japan Society of Computer Aided Surgery,* Vol. 19, No. 3, pp. 123 – 130, Feb. 2017.

[2] Francis Bechet, Kenji Ogawa, Emre Sariyildiz, and Kouhei Ohnishi, "Electro-Hydraulic Transmission System for Minimally Invasive Robotics," *IEEE Transactions on Industrial Electronics,* Vol. 62, No. 2, pp. 750 – 760, Apr. 2015.

International Conference (As a first author)

[1] Kenji Ogawa, Kouhei Ohnishi, and Yousef Ibrahim "Robust Force Control with a Novel Gain Tuning Methodology Based on the Stable Margin Theory," In *Proceedings of the 26th IEEE International Symposium on Industrial Electronics,* Edinburgh, UK, Jun. 19th – 21st, 2017.

[2] Kenji Ogawa, Kouhei Ohnishi, and Yousef Ibrahim, "New State Observer Gain Tuning Methodology Based on the Stable Margin Theory," In *Proceedings of the 18th Annual International Conference on Industrial Technology,* Toronto, Canada, Mar. 22nd – 25th, 2017.

[3] Kenji Ogawa and Kouhei Ohnishi, "Development of A Haptic Palpation Device With A Scaling Bilateral Control for The NOTES Surgery", In *Proceedings of the 2015 IEEE International Conference on Mechatronics, ICM 2017,* Gippsland, Australia, Feb. 13th – 15th, 2015.

[4] Kenji Ogawa and Kouhei Ohnishi, "Evaluation of Stiffness Calculation for Organ Palpation Device with Electro-Hydraulic Transmission System Based Remote Actuator," In *Proceedings of the 13th IEEE 2015 International Conference on Industrial Informatics,* Cambridge, UK, Jul. 22nd – 24th, 2015.

[5] Kenji Ogawa, Ryohei Kozuki, Bechet Francis, and Kouhei Ohnishi, "Development of Electro-Hydraulic Transmission System Based Haptic Remote Actuator for Organ Palpation Device,." In *Proceeding of the 1st IEEJ International Workshop on Sensing, Actuation, and Motion Control, SAMCON 2015,* Nagoya, Japan, Mar. 9th – 10th, 2015.

[6] Kenji Ogawa, Ryohei Kozuki, and Kouhei Ohnishi, "A Method for Improving Scaling Bilateral Control by Integration of Physical and Control Scaling Ratio", In *Proceedings of the 2015 IEEE International Conference on Mechatronics, ICM 2015,* Nagoya, Japan, Mar. 6th – 8th, 2015.

[7] Kenji Ogawa and Kouhei Ohnishi, "Propopsal of Friction and Force Transmission Compensator for Cancer Hardness Measurement System Using Flexible Actuator," In *Proceeding of the 23rd International Symposium on Industrial Electronics, ISIE 2014,* Istanbul, Turkey, Jun. 1st– 4th, 2014.

[8] Kenji Ogawa, Ryohei Kozuki, and Kouhei Ohnishi, "Analysis of Force Transmission Ability by Variation of Thrust Wire Posture," In *Proceedings of the 13th International Workshop on Advanced Motion Control,* Yokohama, Japan, Mar. 14th – 16th, 2014.

International Conference (As a co-author)

[1] Toshiaki Okano, Kenji Ogawa, and Kouhei Ohnishi, "Motion Loading System Taking Into Account The Variable Control Stiffness and Human Reactions," In *Proceeding of the IEEE 24th International Conference on Mechatronics and Machine Vision in Practice,* Aukland, New Zealand, Nov. 21st – 23rd, 2017.

[2] Yoshiyuki Kambara, Kenji Ogawa, and Kouhei Ohnishi, "Modal Space Disturbance Decoupling Method for Bilateral Control," In *Proceeding of the 2nd IEEJ International Workshop on Sensing, Actuation, and Motion Control,* Tokyo, Japan, Mar. 7th – 8th, 2016.

[3] Ryohei Kozuki, Kenji Ogawa, and Kouhei Ohnishi, "A Power Based Compensation Method for Bilateral Control System under Time Delay," In *Proceeding of the 1st IEEJ International Workshop on Sensing, Actuation, and Motion Control,* Nagoya, Japan, Mar. 9th – 10th, 2015.

[4] Ozhan Ozen, Emre Sariyildiz, Haoyong Yu, Kenji Ogawa, Kouhei Ohnishi, and Asif Sabanovic, "Practical PID Controller Tuning for Motion Control," In *Proceedings of the 2015 IEEE International Conference on Mechatronics,* Nagoya, Japan, Mar. 6th – 8th, 2015.

[5] Ryohei Kozuki, Kenji Ogawa, and Kouhei Ohnishi, "Elimination of Reactive Communication Operational Force in Bilateral Control System under Time Delay," In *Proceeding of the 2015 IEEE International Conference on Mechatronics,* Nagoya, Japan, Mar. 6th – 8th, 2015.

[6] Takaaki Ikeda, Kenji Ogawa, and Kouhei Ohnishi, "Quantitative Evaluation of Stroke Paralysis Considering Individual Differences in Symptoms," In *Proceeding of the 2015 IEEE International Conference on Mechatronics,* Nagoya, Japan, Mar. 6th – 8th, 2015.

[7] Nobuto Yoshimura, Kenji Ogawa, and Kouhei Ohnishi, "Verification of Compliance Control for Soft Robot," In *Proceeding of the 13th International Workshop on Advanced Motion Control,* Yokohama, Japan, Mar. 14th – 16th, 2014.

Domestic Conference (As a first author)

[1] Kenji Ogawa, Yoshiyuki Kambara, Hiromu Sekiguchi, and Kouhei Ohnishi, "A Modal Space Decoupling Method for Bilateral Control Considering With Environmental Impedance," In *Proceeding of the 2016 IEE-Japan Industry Applications Society Conference,* Gunma, Japan, Aug. 30th – Sep. 1st, 2016.

[2] Kenji Ogawa, Hiroki Nagashima, Yuri Yamamoto, Koyo Yu, Yoshitaka Abe, Yasunari Ikeda, Kouhei Shigeta, Kazunobu Shinoda, Yohei Yamada, Masashi Tsuruta, Masaru Nakamura, Koji Okabayashi, Daisuke Aoki, Yuko Kitagawa and Kouhei Ohnishi, "Study Concerning the Effects of Laparoscopy Angle on the Suture Operation Part 1: Suture Time," In *Proceeding of the 28th Annual Meeting of the Japan Society for Endoscopic Surgery,* Osaka, Japan, Dec. 10th–12th, 2015.

[3] Kenji Ogawa, Seinan Kyo and Kouhei Ohnishi, "The Validation of *in vitro* Experiments of Friction and Force Transmission Compensator for cancer Hardness Measurement System Using Flexible

Actuator," In *Papers of the IEE Japan Technical Meeting on Industrial Instrumentation and Control,* Tokyo, Japan, Mar. 10th–11th, 2014.

[4] Kenji Ogawa, Kouhei Ohnishi and Norihito Wada, "Development of Non-invasive Hardness Measurement System trough Endoscope," *Journal of Japan Society of Computer Aided Surgery*, Vol.15, no.2, pp.186–187, Tokyo, Japan, 2013.

Domestic Conference (As a co-author)

[1] 岩本晃明, 小川健司, 冨塚大輔, 吉池美紀, 野澤資亜利, 中澤龍斗, 佐藤陽子, 森川康英, 大西公平, "ロボット支援を用いた非閉塞性無精子症に対する MD-TESE の精子回収率改善を目指した挑戦的萌芽研究：第 1 報 ハムスター精巣の硬さと造精機能との関連," **第 *105* 回日本泌尿器科学会総会**, 鹿児島, 日本, 4 月 21 日–24 日, 2017.

[2] 萩野詩季, 栗脇良太, 小川健司, 富塚大輔, 吉池美紀, 野澤資亜利, 中澤龍斗, 谷口雅康, 高木光博, 森川康英, 大西公平, 佐藤陽子, 岩本晃明, "ロボット支援を用いた非閉塞性無精子症に対する MD-TESE の精子回収率改善を目指した挑戦的萌芽研究：第 2 報 ハムスター精巣の硬さに影響する精巣内構造の変化に関する形態学的解析," **日本アンドロロジー学会第 *36* 回学術大会**, 岡山, 日本, 12 月 10 日–12 日, 2017.

[3] Daisuke Tomizuka, Kenji Ogawa, Miki Yoshiike, Shiari Nozawa, Ryuto Nakazawa, Yoko Sato, Kouhei Ohnishi, Yasuhide Morikawa, and Teruaki Iwamoto, "Developmet of the System to Measure the Hardness of the Testis for Evaluating the Ability of Spermatogenesis A Preliminary Study Using Hamster Testis ," *Journal of Japan Society of Computer Aided Surgery*, Vol.18, no.4, pp.271–272, Tokyo, Japan, Nov. 26th – 27th, 2016.

[4] Masaru Nakamura, Koji Okabayashi, Masashi Tsuruta, Kouhei Shigeta, Kenji Ogawa, Hiroki Nagashima, Yuri Yamamoto, Koyo Yu,Yoshitaka Abe, Yasunari Ikeda, Daisuke Aoki, Yuko Kitagawa and Kouhei Ohnishi, "Study Concerning the Effects of Laparoscopy Angle on the Suture Operation Part 2: Suture Distance," In *Proceeding of the 28th Annual Meeting of the Japan Society for Endoscopic Surgery*, Osaka, Japan, Dec. 10–12th, 2015.

[5] Takaaki Ikeda, Kenji Ogawa, Kazuki Tanida and Kouhei Ohnishi, "Development of Bilateral Upper Limb Rehabilitation System with Turntable System," In *Papers of the I.E.E. Japan Technical Meeting on Industrial Instrumentation and Control*, Tokyo, Japan, Mar. 10–11th, 2014.

[6] Yoshiki Ohno, Kenji Ogawa and Kouhei Ohnishi, "Performance Improvement Method for Communication Disturbance Observer under Varying Time Delay," In *Papers of the I.E.E. Japan Technical Meeting on Industrial Instrumentation and Control*, Tokyo, Japan, Mar. 10–11th, 2014.